

Functionality Determinants and Pore-level Quantitative Structure–Activity Relationship (QSAR) Approach for Water Permeation Rate in Aquaporins

Juan José Galano-Frutos ^{1,a,*}, Luca Bergamasco ^{2,a,*}, Paolo Vigo ², Matteo Morciano ², Matteo Fasano ², Davide Pirolli ¹, Eliodoro Chiavazzo ² and Maria Cristina de Rosa ¹

¹ Istituto di Scienze e Tecnologie Chimiche “Giulio Natta” (SCITEC) - National Research Council (CNR), Via Largo Francesco Vito 1, 00168 Rome, Italy

² Department of Energy, Politecnico di Torino, C.so Duca degli Abruzzi 24, 10129 Turin, Italy

^a These authors contributed equally to this work.

* **Correspondence:** J.J. G.-F. juan-jose.galano-frutos@scitec.cnr.it; L.B. luca.bergamasco@polito.it

Abstract: Aquaporins play a key role for the regulation of water transport and solute selectivity in biological cells and tissues. Due to their unique properties, during the last years aquaporins (AQPs) have attracted increasing interest for their use in the development of biomimetic membranes for water filtration. Motivated by this fascinating application, and the need for reliable methodologies to rationalize the design of AQPs or other biomimetic molecules with targeted filtration properties, we conduct in this work an all-round analysis of their structural features to provide crucial insights into the key determinants of functionality of these relevant biomolecules. Particularly, we analyze —on a selected set of experimentally-resolved AQP structures— the composition and peculiarities of their NPA and Selectivity Filter (SF) motifs, the overall structural and sequence similarities between them, their pore shape and the residue-level pore-lining composition. Then, AQPs’ pore structural and physico-chemical descriptors are put into correlation with available data on experimental permeation rate, within the context of a pore-level QSAR modeling. The approach, presented here as a methodological proof of concept, enables the identification of key —potentially novel— features related to water permeability, which could contribute to a deeper residue-level understanding of AQP filtering properties. Potential beneficiary areas include the rational design of optimized AQP-based biomimetic membranes and research into the molecular mechanisms underlying AQP-related diseases.

Keywords: Aquaporins; Pore Permeation; Pore Selectivity; Structural Motifs; Pore Descriptors; QSAR

1. Introduction

Water is vital for any biological system, as it constitutes about 70% of the mass of most living organisms. The maintenance of ionic homeostasis and water levels within the cell and within different organisms’ tissues and compartments is a function that has been linked to a protein family called aquaporins (AQPs). Initially referred to as CHannel-forming Integral Protein (CHIP) [1,2] or Major Intrinsic Proteins (MIPs), AQPs are 28-35 kDa integral membrane protein channels, which enable the transport of water across cells with a high efficiency and a unique selectivity (a nicely and succinctly told history about the discovery of aquaporins can be found in [3]). Found as homotetramers, each subunit forms an integral membrane pore, characterized by six transmembrane spanning domains, with cytosolic amino and carboxy termini. Only pure water and small uncharged solutes, e.g. glycerol, urea, metalloids, carbon dioxide, nitrogen, hydrogen peroxide and ammonia, are allowed to pass through the pore. This selectivity is due to an electrostatic barrier located at the center of the channel, which prevents the passage of protons and other charged molecules [4]. Phenomena like the survival of some plants in extreme environments, characterized by saline-alkaline soils, high or low temperatures, heavy metal toxicity and drought are owed to adaptations developed by these organisms thanks to the presence of AQPs [5–8]. AQPs have also been associated with cell volume regulation, transepithelial fluid transport, cell migration and

proliferation, neuroexcitation, among other physiological events [9–11]. In this regards, they have been directly linked to various non-infectious and infectious diseases in humans [3,9,10,12,13], highlighting the importance of their study across a variety of research and development fields.

AQPs are found in a huge variety of taxa, from mammalian to bacteria [3], which suggests a common ancestor whose structure has conserved for over 2 to 3 billion years of evolution [14]. There are more than 350 known aquaporins, with 13 subfamilies found in mammalian, namely Aqp0-12. Mammalian AQPs are usually divided into three sub-classes, one containing proteins that allow only water molecules flow, namely Aqp0, 1, 2, 4, 5, 6 and 8, which are referred to as orthodox aquaporins, another one that allows the transport of water and other small solutes, like glycerol or urea, that includes Aqp3, 7, 9 and 10, referred to as aquaglyceroporins (AQGPs), and a more recently discovered class that has comparatively lower sequence homology (about 20%) with the orthodox aquaporins, that includes Aqp11 and Aqp12, referred to as unorthodox or superaquaporins [13,15]. A high AQPs diversity is also present in plants, where there are five homologous AQPs subfamilies, namely plasma membrane intrinsic proteins (PIP), tonoplast intrinsic protein (TIP), small basic intrinsic protein (SIP), nodulin-26 like intrinsic protein (NIP) and X intrinsic proteins (XIP) [6]. Amphibians [16], bacteria [17] and fungi [18] have also been reported to carry AQPs. Henceforth, the term AQPs will generically refer to all classes of these molecules, except when a specific distinction is required. In such cases, strictly water-permeant aquaporins will be referred to as AQPs, whereas those that allow the passage of glycerol and other solutes will be referred to as AQGPs.

Thanks to their inherent functional characteristics, AQPs are used for developing next-generation ultra-permeable membranes [19,20]. Aquaporin-based biomimetic membranes (ABMs) [21] have demonstrated remarkable promise both in water desalination [22,23] (see reviews [24–28]) and wastewater treatment [29–31]. Their application for these and other related purposes has proven to be a valuable solution [32–34] as an alternative to conventional reverse osmosis (RO) [35,36] or thermal desalination techniques [37,38]. Achieving cost reduction and devising an efficient upscaling strategy, all while safeguarding and fully harnessing the distinctive functionality of aquaporin proteins, represent the 'grand challenge' in advancing the design of ABMs [24]. In line with this, Cohen-Tanugi and colleagues [34] demonstrated the potential for energy and cost savings of increased membrane permeability. Moreover, reviews by Hélix-Nielsen [26] and Beratto-Ramos et al. [31] outlined the primary difficulties that still persist in the fabrication of ABMs, which are mainly based both on the presence of membrane defects that lead to impaired transport performance and protein (and/or membrane) instability. They also emphasized the necessity of adopting novel optimization and design strategies to enhance this technology further. In close alignment with this imperative, the past 15 years have witnessed a significant surge in the development of bio-inspired artificial water channels (AWCs), which has been driven by the ambition to fabricate synthetic counterparts of AQPs (see reviews [39,40], and recent applications in [41,42]), marking a notable frontier in scientific exploration.

In response to the growing demand of membrane-based technology for water filtration purposes, as well as the important physiological functions and pathophysiological roles in diseases [9,11], significant efforts —spanning both experimental and computational domains— have been dedicated to unraveling the working principles governing the permeation and selective capabilities of AQPs (see reviews [14,15,43–47]). Such efforts are geared towards harnessing their potential for advanced optimization and design strategies. For instance, it has been shown that AQPs' water permeability and high solute rejection occur through a narrow hydrophilic constriction, typically around ~3 Angstroms, which facilitates the formation of a water single-file wire [48]. This process is characterized by hydrogen bonding among water molecules [43,49], alongside bonding and polarizing interactions with the pore lining [48]. Also, amino acids positions determinative of AQP vs. AQGPs selectivity, and those involved in auto-regulatory events linked to post-translational modifications have been unveiled through a variety of experimental methods, including site-directed mutagenesis, chimeric domain swaps, membrane permeability assays, electron crystallography, X-ray crystallography, and molecular dynamics simulations [15,50,51]. However, a precise and thorough comprehension, particularly at the atomic or residue level, of the permeation properties, selectivity and mechanisms exhibited by natural AQPs is still missing [52].

In this regard, the primary motivation for this article is twofold. First, to describe and analyze the best available structural and functional information on AQPs. Second, to conduct a comprehensive analysis of all this information to uncover key features that primarily confer the filtering and selectivity capabilities to these fascinating biomolecules.

2. Characteristic Features of AQPs: Similarities and Differences

2.1. Basic Structure

Aquaporins are homotetramers formed by four monomer channels, each constituted by six transmembrane and two half-spanning helices interconnected through five loops [50,52,53] (Figure 1). The inner terminals of the two half helices host the amino acid sequences constituting the NPA motifs, which face each other in the middle of the pore (see Figure 1 panel B). This motif typically involves asparagine, proline and alanine (Asn, Pro and Ala) residues, which are highly conserved in aquaporins [4,35,48,52–68] (see **Section 2.2**). In this region, proton exclusion is accomplished with a reorientation of the water molecules, which favors their passage [4,43,50,69].

Each monomer presents a second-stage filtering feature in its channel that is located closer to the extracellular border [43,52] and works as a constriction region. This feature is generally referred to as selectivity filter (SF) or ar/R (aromatic/arginine) region, since it always comprises at least one aromatic residue and one Arg (Figure 1, panel B; see **Section 2.3**). On the outside of the pore, helices are hydrophobic, while on the inside they are mainly hydrophilic [70]. Each monomer is functionally independent with its own pore (Figure 1, panel C), and when assembled together, the four monomers form a pore in the middle. No water permeation has been observed in natural AQPs through this central pore, so that the flux takes place only through the four lateral pores of the monomer units [71]. While the orthodox AQPs' pore has been shown to have approximately 1-3 Å minimum diameter [69], AQGs exhibit a constriction pore passage which is approximately 1 Å wider, which allows them to accomplish glycerol diffusion [70]. In the following sections, we will present a detailed analysis of the two main features described above (see Table 1), along with an examination of the pore diameter and geometric characteristics of the selected set of AQPs (Table 2). In addition, we include a Supplementary Section where we conducted structure- and sequence-based comparative analyses, to highlight the similarities and differences exhibited by these fundamental filtering molecules (Figure S1 and Figure S2).

2.2. NPA Motif

The AQP family features two highly conserved asparagine-proline-alanine (NPA) motifs that are absent in other protein channels, like gramicidin A [4]. These two motifs, located in the narrow central segment of the channel are essential for water permeation and selectivity. Proton exclusion, which is essential to maintain the electrochemical gradient across cellular and subcellular membranes, is accomplished thanks to a reorientation of the water molecules inside the pore passage [4,43,50]. This reorientation is realized thanks to the two asparagine residues facing each other in the NPA motif [69,72], which create H-bonds with the water molecule in transit, substituting some of the water-water H-bonds [43]. The hydrogen bonds with the two Asn residues, instead, facilitate water diffusion through the pore [62,69]. This reorientation allows their continuous flux so that, when one molecule moves through the channel, the next one is readily available to follow the same path [57,69]. A slightly different mechanism has been suggested in some aquaporins. For instance, in hAqp4, the two asparagines (Asn97 and Asn213) separately form H-bonds with two different water molecules, while in most other AQPs only one water molecule is involved at a time [64]. This arrangement has also been observed in the crystal structures of hAqp5 and soPIP2;1 [64]. In aquaporins-0, the Asn184 donate a hydrogen bond to a tyrosine, Tyr23, which in turn donates it to the water molecule [72,73]. In this regard, the low water permeation observed in these AQPs (see Table S1) could be associated with the presence of this Tyr23, which is not present in other aquaporins.

In addition to facilitating water reorientation and thus proton exclusion, the NPA region can also function as a selectivity filter. When the two NPA motifs approach each other, a constriction forms, although the narrowest point most often occurs at the ar/R region (see **Section 5**).

Little sequence variation is found in the NPA motif through the whole family of aquaporins (Table 1). This occurs, for instance, in human aquaglyceroporin-7 (hAqp7), which allows glycerol permeation through cell membranes [74]. Human Aqp7 exhibits uncommon substitutions in its NPA motifs while both asparagine residues are conserved. This

results in the formation of distinctive triads: NAA (Asn94, Ala95, and Ala96) and NPS (Asn226, Pro227, and Ser228, see Table 1) [74]. Another case pertains to the aquaglyceroporin found in the malarial parasite *Plasmodium falciparum* (pAqgp), a protein of great significance in the life cycle of the parasite [75]. In pAqgp, both NPA regions undergo substitutions, although the two asparagines remain also conserved: NLA (Asn-Leu-Ala) and NPS (Asn-Pro-Ser) triads (Table 1). These modifications have been suggested to be crucial in maintaining the proper alignment of the asparagine residues at the selectivity filter [75].

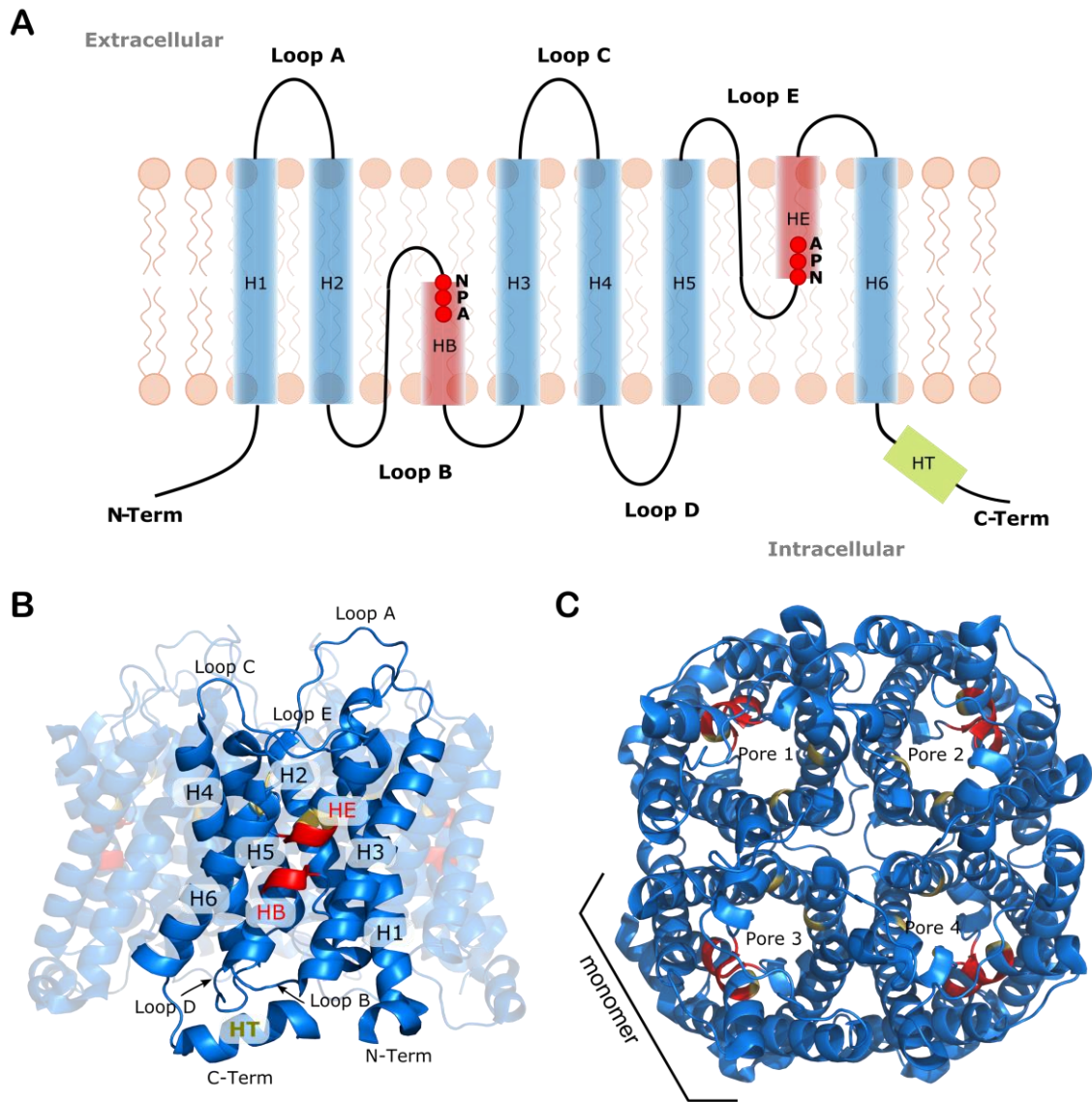


Figure 1. Structural features of mammalian AQPs. (A) Schematic representation of the mammalian AQP channel topology. Each monomer comprises six transmembrane helices (H1–H6) connected by five loops (A–E) and an additional C-terminal short amphipathic helix (HT). Loops B and E fold back into the membrane, forming two half-membrane spanning helices (HB and HE) that harbor the two asparagine–proline–alanine (NPA) motifs (red colored circles). The N- and C-termini are located in the cytoplasm, and the amphipathic helix (HT) is a common protein–protein interaction site. (B) Crystal structure (side view) of the human aquaporin-1 (hAqp1, PDB ID 7UZE [76]), highlighting the structural features for one monomer, as represented in panel A. The NPA motifs are highlighted in red, and the selectivity filter (SF) motif is highlighted in yellow. (C) Tetrameric structure of hAqp1 viewed from the cytoplasmic side, with the pores indicated on each monomer.

2.3. Selectivity Filter Motif

Aquaporins exhibit an hourglass structure, where the narrowest part of their pore is formed by some conserved amino acids —usually in the number of four— that facilitate the passage of water [69,77] in single file [48]. The composition

of this region, known as selectivity filter (SF) or aromatic/arginine (ar/R) motif [11,52], affects the dimension and polarity of the pore, ultimately influencing its solute selectivity and permeation rate [57,58,67,78]. SF contains at least one arginine and one aromatic residue, although the specific composition may vary among different AQPs (Table 1).

Table 1. Sequences of the NPA and the selectivity filter (SF) motifs of selected AQPs. The symbols highlight the difference or identity in the sequence of the NPA motif (middle column), and in the SF motif (last column).

AQP short name ^a	PDB ID	Sequences of the NPA motifs ^b			Sequence of the SF motif ^c					
bAqp0	1YMG	NPA 68-70	&	NPA 184-186	⊖	Phe48	His172	Arg187	Ala181	Δ
oAqp0	2B6O	NPA 68-70	&	NPA 184-186	⊖	Phe48	His172	Arg187	Ala181	Δ
bAqp1	1J4N	NPA 78-80	&	NPA 194-196	⊖	Phe58	His182	Arg197	Cys191	⊖
hAqp1	7UZE	NPA 76-78	&	NPA 192-194	⊖	Phe56	His180	Arg195	Cys189	⊖
aAqp1	7W7S	NPA 70-72	&	NPA 184-186	⊖	Phe50	His172	Arg187	Cys181	⊖
kAqp1	3ZOJ	NPA 112-114	&	NPA 224-226	⊖	Phe92	His212	Arg227	Ala221	Δ
hAqp2	4NEF	NPA 68-70	&	NPA 184-186	⊖	Phe48	His172	Arg187	Cys181	⊖
hAqp4	3GD8	NPA 97-99	&	NPA 213-215	⊖	Phe77	His201	Arg216	Ala210	Δ
rAqp4	2D57	NPA 97-99	&	NPA 213-215	⊖	Phe77	His201	Arg216	Ala210	Δ
hAqp5	3D9S	NPA 69-71	&	NPA 185-187	⊖	Phe49	His173	Arg188	Cys182	⊖
hAqp7	6QZI	NAA 94-96	&	NPS 226-228	⊖	Phe74	Gly214	Arg229	Tyr223	⊖
hAqp10	6F7H	NPA 82-84	&	NPA 214-216	⊖	Gly62	Gly202	Arg217	Ile211	⊖
soPIP2;1	1Z98	NPA 101-103	&	NPA 222-224	⊖	Phe81	His210	Arg225	Thr219	⊖
mAqpM	2F2B	NPA 82-84	&	NPA 199-201	⊖	Phe62	Ile187	Arg202	Ser196	⊗
aAqpM	3NE2	NPA 83-85	&	NPA 200-202	⊖	Phe63	Ile188	Arg203	Ser197	⊗
osNIP2;1	7CJS	NPA 108-110	&	NPA 219-221	⊖	Gly88	Ser207	Arg222	Gly216	⊕
atTIP2;1	5I32	NPA 83-85	&	NPA 197-199	⊖	His63	Ile185	Arg200	Gly194	⊗
atPIP2;4	6QIM	NPA 107-109	&	NPA 228-230	⊖	Phe87	His216	Arg231	Thr225	⊖
eAqpZ	1RC2	NPA 63-65	&	NPA 186-188	⊖	Phe43	His174	Arg189	Thr183	⊖
aAqpZ2	3LLQ	NPA 63-65	&	NPA 184-186	⊖	Phe43	His172	Arg187	Thr181	⊖
pAqgp	3C02	NLA 70-72	&	NPS 193-195	Δ	Trp50	Gly181	Arg196	Phe190	⊕
eGlpF	1FX8	NPA 68-70	&	NPA 203-205	⊖	Trp48	Gly191	Arg206	Phe200	⊕

^a Full name and AQPs' source organism are given in Table 2 (**Section 8 Materials and Methods**). ^b Information retrieved from the UniProtKB database [79]. ^c Information retrieved in some cases from the reviewed literature and in the others from structural alignment.

In orthodox aquaporins, there is also a highly conserved His residue (Table 1), which normally faces the positively charged Arg residue. This Arg provides two hydrogen bond donor sites to which the His may bind, constricting thus the pore passage [80]. The fact that this His appears replaced in AQPps by a small Gly, preventing the formation of the key H-bond interactions mentioned, suggests an important role for the former in the solute selectivity of these proteins [69]. Krenc and colleagues [80], working with the rat aquaporin-1, demonstrated the importance of this His through a mutational study in the position.

Greater sequence variability is evident in the SF motif compared to the NPA sequences among the AQPs listed in Table 1. In bAqp1 (Figure 2, panel A), for instance, the SF is formed by a hydrophobic corner (Phe58) and a hydrophilic face (His182, Arg197 and Cys191) on the opposite side [56] (Figure 2, panel B). The same residues are found in hAqp1

forming an almost identical SF: Phe56, His180, Arg195 and Cys189 [67]. This SF sequence is also carried by the aquaporin-1 of other organisms (e.g., *Anabas testudineus*: aAqp1), as well as by human aquaporins 2 and 5 (hAqp2, hAqp5). This set of AQPs is indicated with the symbol \ominus in Table 1.

Bovine and ovine aquaporins 0 (bAqp0, oAqp0), as well as the human and rat aquaporins 4 (hAqp4, rAqp4, with symbol Δ in Table 1), present the same residues quartet in their SF motif, namely Phe, His, Arg and Ala. Three of these residues (Phe, His and Arg) match those found in the SF of the previous set of aquaporins (\ominus), while the Cys is substituted by an Ala residue. In aquaporins 0, this change enables the formation of a secondary constriction region, resulting in reduced water permeation [81,82]. In aquaporins 4, the His is thought to play a determinant role in preventing glycerol passage [64,83].

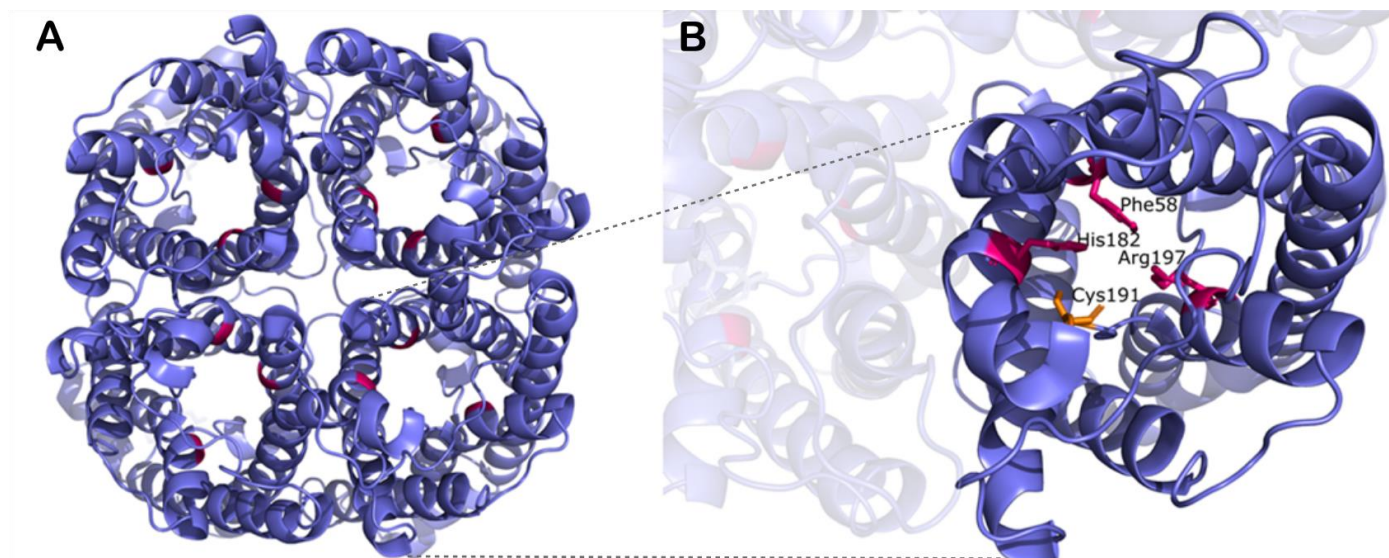


Figure 2. Location of the selectivity filter in the bovine aquaporin-1 (bAqp1, PDB ID 1J4N [56]) viewed from the cytoplasmic side (A). Arrangement of the SF residues in one of the monomers (B). The three conserved residues (Phe58, His182, Arg197) are highlighted in magenta, and the less conserved one (Cys191) is shown in orange (the side chains in sticks).

Another subgroup of AQPs sharing the same residues in their SF motif, namely Phe, His, Arg and Thr (with symbol \square in Table 1), includes the spinach plasma membrane aquaporin (soPIP2;1) [84], the *E. coli* and *Agrobacterium fabrum* aquaporins Z (eAqpZ [57], aAqpZ2 [85]), and the *Arabidopsis thaliana* aquaporin atPIP2;4 [86]. In this group, the distinctive element is the Thr residue in the fourth amino acid position. In the bacterial (*E. coli*) eAqpZ, for instance, the Arg residue (Arg189) has been suggested to be crucial, as it shows two diverse conformations that result in significant differences in water permeability [65]. In one of these conformations, Arg189 forms a hydrogen bond with Thr183, which is believed to prevent the passage of water [65]. Thus, eAqpZ can exhibit structures that are either permeable or impermeable to water.

Other sequences in the SF region show a Gly residue in the second position, with a variety of other amino acids in the first and fourth positions. This is the case, for instance, of the human aquaporins 7 (hAqp7) [74] and 10 (hAqp10) [87], as well as the AQGP from the malarial parasite *Plasmodium falciparum* (pAqgp) [75] and the *E. coli* glycerol-conducting channel (eGlpF) [56].

Ile or Ser residues can also accompany Arg in the central positions of the SF region [48–50]. Archaeal (*Methanothermobacter marburgensis*) aquaporin (mAqpM) is particularly interesting because it may exhibit multi-functional transport features. In this aquaporin, the His residue, highly conserved among water-selective AQPs, is replaced by an isoleucine residue at position 187 (Phe62, Ile187, Arg202 and Ser196). This substitution, which creates in mAqpM a wider and more hydrophobic SF than that observed in aquaporins 1, is believed to be an adaptation for the conductance of larger and less polar permeants than water, e.g., H₂S and CO₂, in addition to the water transport [59]. At the same time, the presence of Ile187 —which together with Phe62 forms the hydrophobic part of the mAqpM's constriction

region— creates a pore narrower than that of the *E. coli* glycerol-conducting channel, eGlpF, suggesting that mAqpM may be not suited to conduct glycerol [59].

A particular conformation of the SF has been identified in the ammonia-permeable *Arabidopsis thaliana* TIP2;1 (His63, Ile185, Arg200 and Gly194), which is also permeable to water [88]. Here, the conserved His in position 2 is replaced by a more hydrophobic Ile185 increasing pore diameter. The most interesting feature, however, is the behavior of Arg200, whose sidechain is pushed to the side of the pore by His131, which acts as a fifth element of the SF motif. Besides, Arg200 is H-bound to His63, conserved across all tonoplast intrinsic proteins (TIPs), which replaces the aromatic residue (Phe or Trp) mostly present in the other AQPs. The presence of both His63 and Arg200, along with the referred SF's fifth residue, His131, are a characteristic element of aquaammoniaporins [88].

In summary, three residues —Phe, His, and Arg— are conserved across the majority of the aquaporins analyzed in this study. Notably, Arg is conserved across all AQPs. While His is highly conserved among all orthodox AQPs [56,60,61,64,65,85,88], this hydrophilic residue is replaced by a Gly in AQQPs [48,74,75,87], leading to increased hydrophobicity and pore size. In the next section, we present and analyze the permeation rates reported for the set of aquaporins listed in Tables 1 and 2.

3. Permeation Rate

As previously anticipated, two key functional elements of AQPs are their selectivity and permeation properties. In the previous sections we qualitatively described the main structural motifs that shape these properties, and highlighted the similarities and differences across the representative set of AQPs here investigated. AQPs' pore shape, whose conical design —both in the cytoplasmic and the extracellular entrances (see **Section 5**)— ensures the creation of highly permeable water channels that can transport $\sim 10^9$ water molecules per second (per monomer) in a single-file manner [89–92]. Both experimental [1,51,89,90,92–94] and *in silico* [4,49,91,95,96] approaches have been devised to measure or simulate the water permeation rate of AQPs. Back in the early 90's, *in vitro* functional assays were developed to measure the osmotic water permeability of membrane water channels. Classical —though still used— swelling assays based either on the microinjection and expression of a transcribed protein sequence (typically the mRNA of the protein channel of interest) in *Xenopus laevis* oocytes (oocytes swelling assay: OSA) [1] or the reconstitution of the protein in liposomes (proteoliposome swelling assay: PSA) [89], have been indispensable tools for the estimation of the water permeation rates of many AQPs. On the computational side, most approaches have relied on molecular dynamics simulations (MDS), including simulations under equilibrium conditions [49,78,95,97–103], pressure-induced [95], and steered molecular dynamics [96]. However, Zhu et al. [95] indicated that equilibrium MDS is not a reliable method for computing osmotic water permeation rates. They proposed instead using a more realistic approach based on creating a hydrostatic pressure difference across the membrane [95]. The theoretical aspects for calculating permeation rates in aquaporins are also summarised in that article [95].

One aspect that should be mentioned is that, despite improvements in the accuracy —in particular of the physical techniques used[51]— of methods for measuring the water permeation rate of AQPs [104], the vast majority of measurements of their unitary permeability (single-channel osmotic permeation coefficient, p_f) has been achieved by indirect methods. These values are indirectly estimated from the membrane osmotic permeation coefficient (P_f) and channel density measurements, and large errors are often obtained depending on the accuracy of estimated number of channels in the sample. As stated by Gonzalez and collaborators, innovative methodological efforts are still needed to enable direct experimental measurements of the events occurring in water molecules inside AQP channels [44].

Said that, access to reliable quantitative data of AQP permeation rates is required to unravel the key structure-function relationships to a molecular level, as we intend here. We have, therefore, compiled here the osmotic water permeation rates (per single-channel, p_f) that appear reported for the AQPs collected in this work, encompassing both experimental and computational methodologies (see Table S1 and Figure 3). Experimental data was not found for some AQPs listed in Table 1, for which only *in silico* data is reported. Unfortunately, for some AQPs, we could not find any data, or the reported permeation rates were not provided as single-channel water permeabilities (i.e., p_f) but rather as global osmotic permeability coefficient (P_f) or other metrics. In cases like these —for instance, with hAqp7 [105–107] and hAqp10 [87]— we were unable to convert P_f into p_f due to the lack of required data for such a transformation. Most of the reported osmotic permeation rates for AQPs have relied on a couple of experimental approaches, namely OSA

and PSA, which have been combined with a variety of physical or imaging techniques [51]. In the last decade, although still insufficient, some efforts have been made to obtain more direct permeation measurements [107] and to apply improved experimental strategies [108].

The human red blood cell aquaporin-1, hAqp1, the first water pore identified by Peter Agre’s group [1,109], has been by far the experimentally most studied AQP (see Table S1). Three research groups, including the Hall’s lab [110,111], the Van Hoek and Verkman’s lab [112–114] and the Agre’s lab [89,90,92], have reported the osmotic permeation rate (p_f) of hAqp1 with fairly low dispersion (Ave \pm MSE: $5.1 \pm 1.2 \times 10^{-14} \text{ cm}^3 \cdot \text{s}^{-1}$ per protein subunit, Figure 3 and Table S1). For the sake of simplicity, the factor 10^{-14} and the units will be omitted from hereon. De Groot and Grubmuller [43], on the other hand, calculated the in silico permeability of hAqp1 (7.5 ± 0.5) through MDS, in good agreement with the experimental average abovementioned. The water permeation of bAqp1, which has a nearly identical structure (0.96 TM-score, Figure S1, panel A, and Figure S2), a high sequence identity (89 %, Figure S1, panel C), and the same NPA and SF motifs (Table 1) as hAqp1, has been both measured (2.3) [113] and calculated (average of 8.8 ± 1.7 [95,97], Figure 3 and Table S1). Despite the differences between the permeations from these two approaches, which is a bit larger for bAqp1 (6.5) than for hAqp1 (2.4), no significant disagreement is observed between the experimentally (2.8) or computationally (1.3) measured water permeations of these two aquaporin-1 channels, as expected for highly similar AQPs.

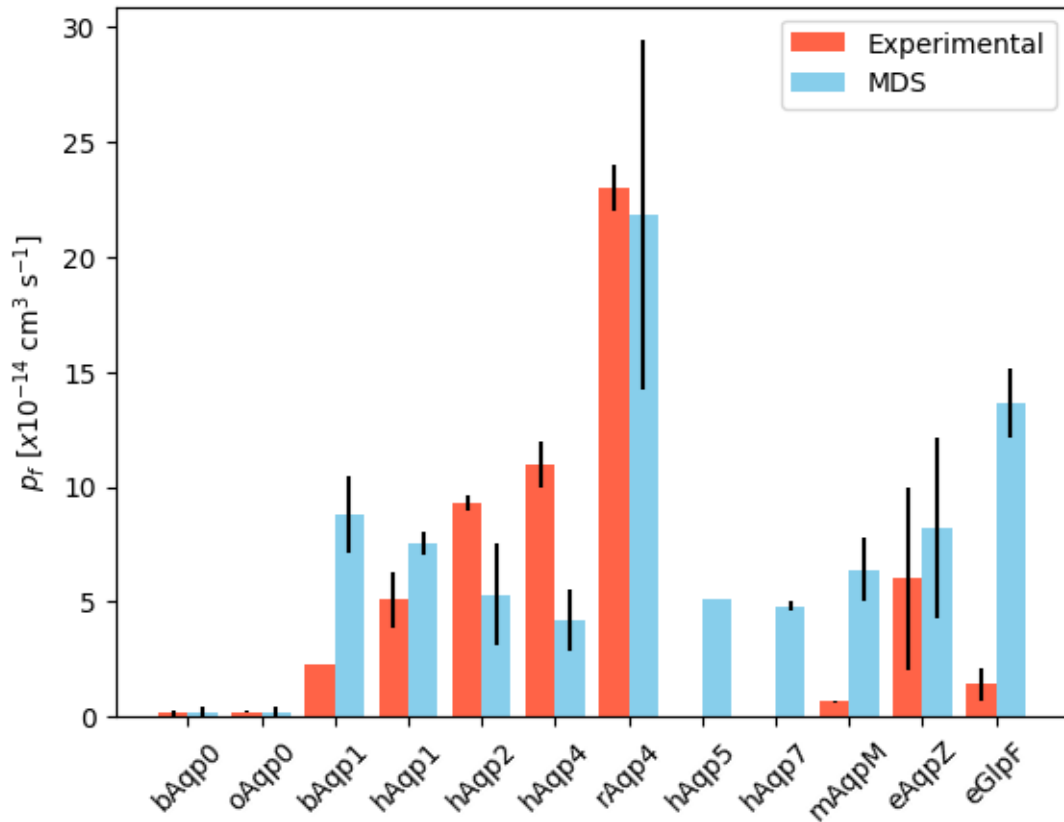


Figure 3. Osmotic water permeations (p_f), in $10^{-14} \text{ cm}^3 \text{ s}^{-1}$, reported for the AQPs in Tables 1 and 2, either from experimental measurements or molecular dynamics simulations (MDS). The experimental methods used, as well as the main conditions and setup established for the measurements are summarized in Table S1. In cases where more than one data has been reported —regardless the method used—, the bars represent the averages thereof and the black vertical lines the mean standard errors. Otherwise, the black lines represent the experimental error in the individual measurement or calculation as reported.

In the case of the Major Intrinsic Proteins of Lens, the so-called MIPs or aquaporins-0, bAqp0 is arguably the most investigated AQP of its type (water permeation average of 0.15 ± 0.1 from experimental measurements [110–112], and 0.2 ± 0.2 from MDS [97], Table S1). We found similar reports for the sheep (SI of 98 % and TM-score of 0.96 versus bAqp0, Figure S1, panels C and A) and rat aquaporins-0, namely 0.2 ± 0.1 [115] and 0.3 ± 0.1 [116], respectively (Table

S1). Rat Aqp0 lacks a 3D structure in the PDB database and therefore it is not listed in Tables 1 and 2. Permeation data for other AQPs, including some not listed in Tables 1 and 2 due to their lack of 3D structure, can be found in Table S1. It is worth noting that, for proteins where both the OSA and the PSA experimental methods have been applied, namely bAqp0, hAqp1 and rAqp4 (see Table S1), the reported water permeations measured through the former method are often significantly lower compared to the latter. Nevertheless, an exhaustive comparison of these methods here is beyond the scope of this work.

Moreover, as the equilibrium MDS approach, mostly used in earlier modeling of AQPs, has been shown to have some limitations [95], and since water osmotic permeations calculated from MDS sometimes exceed experimental measurements by a considerable margin (see bAqp1, mAqpM and eGlpF in Table S1), we will exclude MDS permeation rates from the subsequent modeling approach presented below in **Section 6**. However, we would like to emphasize the importance of MDS-based methods and their application to the modeling of AQP-related phenomena. Unlike experimental methods, MDS-based approaches allow for direct quantitative measurement of AQP permeation and have provided invaluable atom- and residue-level insights into their filtration mechanisms, selectivity, and proton exclusion capabilities [43,49,74,95,97]. In addition, they hold the potential to deepen our understanding of the behavior of protein channels in lipid membranes and to enable detailed thermodynamic and stability analyses [117,118], which could help address the instability issues of AQPs outlined in the literature [31].

4. Pore Composition Analysis

Although specificities of the NPA and the SF motifs of AQPs have been, in general, described, a comprehensive amino acid composition analysis of the AQPs' pore lining at the widest available 3D structural level seems to be missing. Here, using the pore lining amino acid composition provided by the PoreWalker server [119] (**Supplementary Files**), we have extracted the per amino acid and per amino acid type statistics (i.e., non-polar, polar uncharged, polar positively charged, and polar negatively charged residues in the pore lining) across all the AQPs studied, and compared them with the amino acidic composition for the whole protein (Figure 4 and Table S2).

Composition averages per amino acid type for all investigated proteins (Figure 4) indicate that the percentages of non-polar (i.e. Gly, Ala, Val, Ile, Leu, Met, Pro, Phe, Trp) and negatively charged (Asp, Glu) amino acids are reduced by 3.4% (p-value=0.0019) and 1.4% (p-value=0.0008), respectively) in the pore lining compared to the whole protein. Conversely, polar uncharged (Ser, Thr, Cys, Tyr, Asn, Gln) and positively charged (Arg, Lys, His) residues are prevalent by 2.2% (p-value=0.0068) and 2.6% (p-value=0.0003), respectively) in the pore lining. The majority of the AQPs here analyzed follows this general pattern individually (see Table S2). Only hAqp7, one out of the four AQGs in the group, presents a totally opposed profile, namely higher percentages of non-polar and negatively charged amino acids while lower percentages of polar uncharged and positively charged residues in the pore lining. hAqp10 —another AQG—, and osNIP2;1 —a silicon influx transporter in the *Oryza sativa japonica* plant—, do not either fully meet the general composition picture presented by the rest of AQPs (Table S2 and Figure 4).

Focusing solely on the residues of the pore lining, orthodox AQPs from the animal kingdom generally exhibit a higher content of polar residues (charged and uncharged, >38-40%, Table S2) compared to AQPs from other kingdoms, and to hAqp7 (34.4%) and hAqp10 (30.3%), the only two mammalian AQGs in the set. The amino acid contents of these two AQGs more closely match those of non-animal AQPs (Table S2). The higher total content of polar residues in orthodox AQPs from animals relates to the higher content of polar uncharged residues (23.3-33.3% vs. 17.0-29.2% in the remaining AQPs) and positively charged residues (10.0-18.0% vs. 4.8-12.9%). The content of negatively charged residues is similar in both subgroups (2.1-6.7% vs. 2.0-7.5%). All in all, the current composition analysis on the reduced sample of AQPs here studied reveals clear differences in amino acid type composition within the pore lining of animal AQPs compared to AQGs. Such differences are not as evident in the rest of AQPs or AQGs from the other kingdoms. Additionally, the analysis shows that only the AQGs (hAqp7, hAqp10, pAqp and eGlpF) have a pore lining composition where the content of non-polar amino acids is similar to or higher than that in the whole protein (Table S2), which could be related with their different selectivity and permeability (Table S1) compared to orthodox AQPs.

Local amino acidic composition has also been showed to shape the diameter and constriction sites of AQPs' pores. For example, the ar/R region in eGlpF is amphipathic, with the amino acids Trp48 and Phe200 being highly hydrophobic [48]. These two amino acids are usually replaced in orthodox aquaporins: Trp by Phe or His, and Phe by Ala, Thr or

Cys [48]. In hAqp1 (and bAqp1), they are replaced by Phe56 (Phe58) and Cys189 (Cys191), respectively, and on top of that Gly191 is replaced by His180 (His182) (Table 1), which decrease the pore hydrophobicity in aquaporins-1 [55,56,65]. The absence of this hydrophobic corner causes the only passage of water in orthodox aquaporins. Additionally, the presence of the bulkier Phe141 in the NPA region of sheep and bovine aquaporins-0 (oAqp0 and bAqp0) instead of leucine in aquaporins-1 (Leu149 in hAqp1 and Leu151 in bAqp1 [73,81]), results in significantly smaller diameters (Table S3) and consequently lower permeation rates for aquaporins-0 compared to aquaporins-1 (Table S1). In the next section, we also address aspects of AQPs' local composition related to auto-regulatory pore gating events [44], which drive conformational changes that consequently affect their permeability.

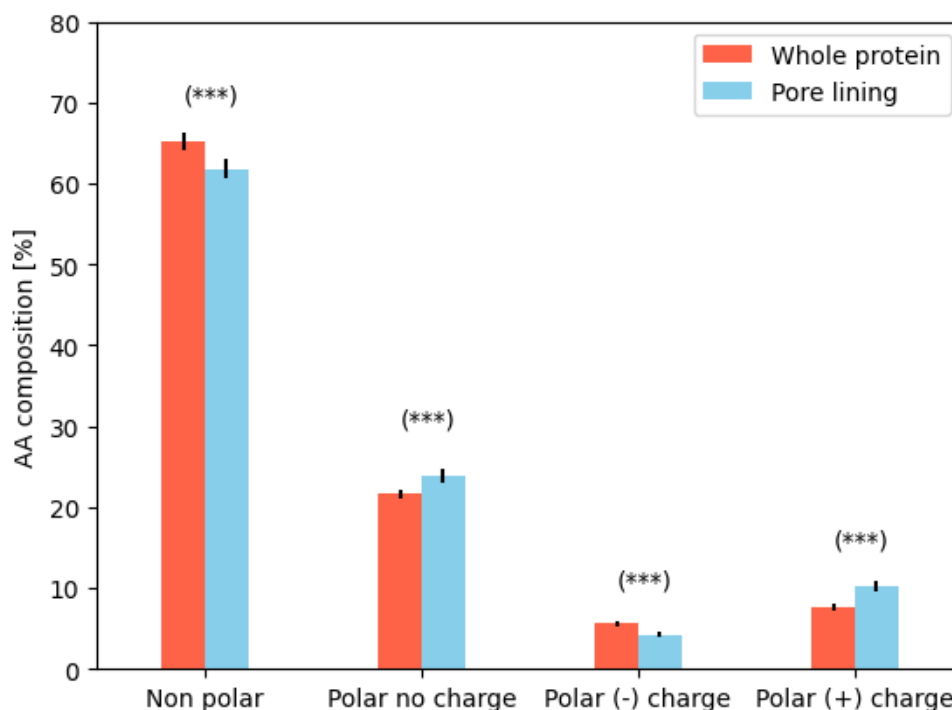


Figure 4. Comparative depiction of the per-amino-acid type composition (in %) both in the whole protein and the pore lining over all the AQPs investigated. The statistical significance (p -value < 0.01) of a t -test for mean differences is shown on each pair of compared bars. Data on the whole protein composition were obtained from the canonical aquaporin sequences retrieved from UniProt database [98]. Statistics on the pore lining composition were calculated based on the information given by the PoreWalker software [119]. FASTA files with the protein sequences used are provided as **Supplementary Files** along with all the output files provided by the PoreWalker tool [119], which contain the pore shape, size and residue-level lining composition. Individual amino acid composition is given in Table S2.

5. Pore Shape Analysis

Pore diameter is perhaps the most comprehensive physical parameter to describe the size and shape of an aquaporin's pore. The PoreWalker tool [119] facilitates the calculation of pore diameter profiles and other properties, such as pore regularity. Additionally, it provides detailed representations of longitudinal cuts of the pores, along with the list of amino acids that make up the pore lining. As an example, Figure 5 depicts the pore diameter profile (panel A, top) of *E. coli* AqpZ—a commonly used aquaporin in ABMs for filtration, desalination, and water purification [27,120]—, wherein the positions of the crucial NPA and SF motifs along the pore's x -axis are highlighted to illustrate their relative localization with respect to the minimum diameter. The 2D projection of the pore shape based on the calculated diameter profile (panel B) and selected longitudinal cuts (panels C and D) provides additional useful information for comparative assessment of the AQPs' pore shape. Figure S3 includes similar panels for the remaining 21 AQPs analyzed in this work. Table S3 contains detailed information including the minimum diameter exhibited by the AQPs' pore, as well as the positions of this minimum, the NPA motifs and the SF along the pore.

Calculated pore diameters by PoreWalker tool [119] range from 1.4-26.5 Å along the entire longitudinal axis among all the AQPs here investigated. Diameter profiles indicate that both the cytoplasmic and extracellular pore entrances have—in general—a conical shape that extends to the single-file region (constriction site) located at the center of the membrane (Table S3 and Figure S3). This hourglass shape, however, varies from aquaporin to aquaporin, being highly regular in bovine and ovine aquaporins-0 (bAqp0 81% and oAqp0 75% regularity along the pore, Table S3), aquaporins-1 (66-85%), human aquaporin-2 (70%), and human aquaporin-4 (65%), whereas it is less regular in the rest of AQPs, namely: aquaporins from plants (39-58%), bacteria (37-64%), and aquaglyceroporins (41-61%, Table S3). Occasionally, the loss of regularity in the pore come together with the loss of the conical shape in one of the two halves, leading to a funnel-shaped pore. This clearly occurs with the two plant AQPs from the highly conserved subfamily known as PIPs, soPIP2;1 and atPIP2;4, as well as the aquaglyceroporin hAqp10 (Table S3 and Figure S3). PIP aquaporins have been extensively studied and shown to exhibit well-conserved auto-regulatory molecular-level mechanisms known as ‘pore gating’ (closure mediated by conformational change of the cytoplasmic loop D, dependent of pH, post-translational modification or calcium-binding) allowing them to adjust membrane water permeation under diverse conditions [9,84,121–124]. Indeed, the selected crystal structure of soPIP2;1 (PDB ID 1Z98 [84]) has been shown to be a closed (pore-gated) conformation [84], which is also the case of atPIP2;4 (verified by structure comparative analysis with soPIP2;1, see Figure S4). Likewise, a pH-dependent pore gating mechanism has been identified in the human aquaglyceroporin hAqp10 [87], wherein His80 has been suggested to be the key residue (pH-sensor). The crystal structure of hAqp10 here analyzed (PDB ID 6F7H [87]) exhibits the closed (pore-gated) conformation (Figure S4). Taking all this into account and examining the diameter profiles calculated by the PoreWalker server for these AQPs, it seems that the apparent pore deformation from a classical hourglass (into a funnel-like shape), as predicted for soPIP2;1, atPIP2;4 and hAqp10 aquaporins, is mainly due to the pore closure at the cytosolic interface (Figure S4). This regulatory mechanism seems to be less conserved in animal orthodox AQPs. Nonetheless, evidence suggesting the presence of other regulatory mechanisms, such as mechanosensitivity [125] and voltage-gating [101,126,127] have also been described. A recent literature review on the pore gating phenomena in AQPs is available in ref. [44].

A residue-level mechanism such as the abovementioned pore gating, modulated by the presence of conserved residues at key positions that undergo chemical modifications, highlights the importance of unraveling the specific structural determinants of AQPs’ permeation and selectivity. A thorough understanding of these elements may be crucial for designing and optimizing more effective AQP-based filtration membranes.

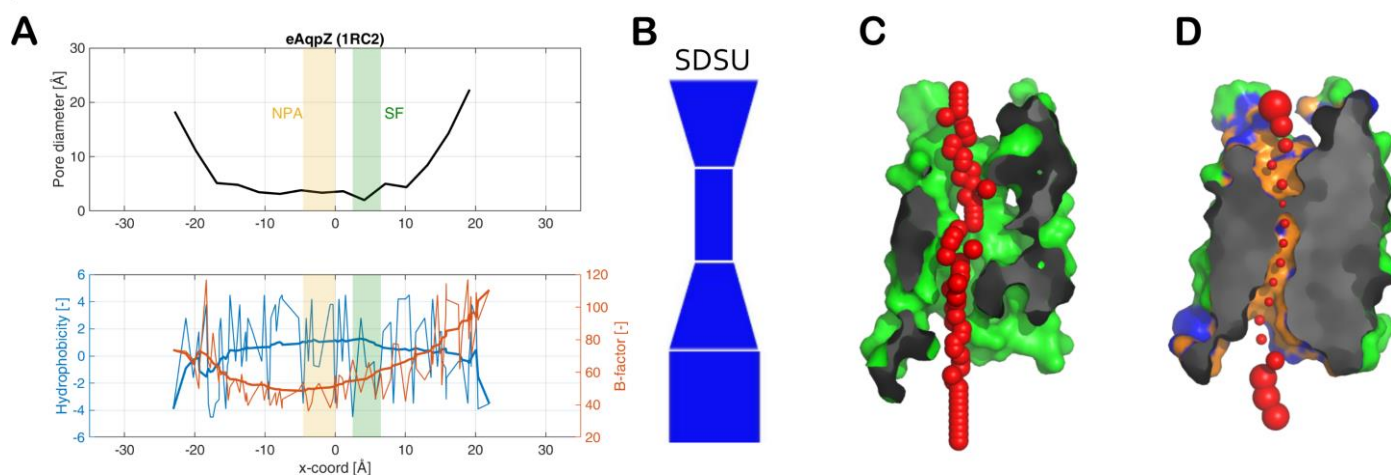


Figure 5. Pore properties profiles and geometrical shape for *Escherichia coli* aquaporin Z (eAqpZ, PDB ID 1RC2). (A) Top panel: diameter profile along the pore principal axis (x -coordinate) at 3Å step as calculated by the PoreWalker tool [119]; Bottom panel: per-residue hydrophobicity index (blue) and B-factor (orange) of amino acids in the pore lining along the pore x -coordinate, as calculated by Discovery Studio (BIOVIA, Dassault Systèmes) [128] and as obtained from the crystal PDB file, respectively. The thicker lines are smoothed curves (noise removed). Vertical bands show the x -coordinates ranges where the NPA (orange) and SF (green) motifs are located. (B) Funnel-like form representing a 2D projection of the predicted pore shape as calculated by variations of diameter values along the pore: the bottom of the pore axis (i.e. the lowest x -coordinate) correspond to the bottom of the stack.

In the letter code on the top of the form, 'D' indicates a conical frustum generated by decreasing pore diameter values, i.e. the diameter of the lower base of the frustum is bigger than the diameter of its upper circle, 'U' indicates the opposite conical frustum, i.e. lower base diameter smaller than upper base diameter, and 'S' indicates a cylinder (the code ordering from bottom to top). (C) and (D) Longitudinal cross-sectional images of the pore issued by PoreWalker, where the pore regularity is shown through red spheres located at the centre of the pore every 1 Å step (C), whereas the pore dimension is represented by red spheres —at the center of the pore at 3 Å step— whose sizes are proportional to the pore diameter calculated at that point (D). In the latter, orange and blue areas show pore-lining atoms and corresponding residues, respectively. **Notes:** Amino acids in the pore lining are reported in the PoreWalker's output files (**Supplementary Files**). The *x*-coordinates in the properties profiles (A) were shifted from the original ones issued by PoreWalker, to place the beta carbon (βC) of the asparagine (N) in the second NPA motif at the center of the *x*-coordinate system (*x*=0). This ensures that all the AQPs are aligned to have the same reference *x*-coordinate.

Water-selective AQPs typically exhibit a minimum pore diameter slightly smaller than that of a water molecule (~2.8 Å), while AQGs have larger diameters [65] (Table S3). In most AQPs, the constriction site (the minimum diameter) of the pore is located at or very close to the SF motif (see Table S3, Figure 5 and Figure S3). In contrast, *Anabas testudineus* aquaporin-1 (aAqp1) and *Arabidopsis thaliana* TIP2;1 aquaporin (atTIP2;1) exhibit the minimum diameter near the NPA motifs. For hAqp10 and atPIP2;4 aquaporins the minimum diameter is located near the cytoplasmic border of the pore (Table S3), consistent with the occurrence of a pore closed (pore gating) —as described above (Figure S4). Among the water-selective AQPs, the aquaporins-0 (bAqp0 and oAqp0) and the human aquaporin-5 (hAqp5) exhibit the smallest diameters, ranging from 1.4 to 1.7 Å. This correlates well, particularly for aquaporins-0, with their water permeations, which are the lowest among all AQPs (Table S1). However, as it has been previously shown [97], and confirmed here by cross-referencing the data in Tables S1 and S3, the minimum pore diameter for the AQPs analyzed does not follow the same hierarchical order as water permeation. Namely, the relative minimum pore diameter order is: oAqp0 < bAqp0 ~ hAqp5 < kAqp1 ~ aAqpM ~ eAqpZ ~ aAqpZ2 < atPIP2;4 ~ soPIP2;1 ~ hAqp2 < rAqp4 < bAqp1 < mAqpM ~ atTIP2;1 < hAqp4 ~ aAqp1 < eGlpF < pAqgp < hAqp1 ~ hAqp7 << osNIP2;1 << hAqp10 (Table S3). While, the relative water permeation order for those AQPs experimentally measured (averages or individual values, as reported in Table S1) is as follows: bAqp0 ~ oAqp0 < mAqpM < eGlpF < bAqp1 < hAqp1 < eAqpZ < hAqp2 < hAqp4 << rAqp4.

6. Pore-level QSAR Study as a Methodological Proof of Concept

Quantitative Structure-Activity Relationship (QSAR) (or Quantitative Structure-Property Relationship, QSPR) modeling, is one of the most extended *in silico* tools employed in medicinal chemistry [129]. In QSAR, features such as solubility, acidity, and polarity are computed as molecular descriptors and then applied to determine which of them can be used to predict measurable tasks, like toxicity, drug-likeness, or enzyme binding. The use of QSAR for modeling the activities (or properties) of peptides and proteins is an emergent field of research not yet as well established as it is for small molecules (e.g., potential drugs [130–132]). This is largely due to the significant complexity involved in applying QSAR to proteins. First, it requires the generation of molecular descriptors —independent variables that must be correlated with the target activity or property— that adequately capture the intricate shape and surface properties of proteins at both local and global levels. Second, translating QSAR modeling results into the design of new, enhanced proteins is challenging since attempting to improve certain protein properties by changing one or a few amino acids can sometimes compromise their local or global stability and thus their functioning, potentially rendering the entire effort futile. Furthermore, any newly designed protein must be tested, which requires at least it to be expressed and isolated, processes that can be both costly and cumbersome. For valuable insights into the current state, development, and optimization of molecular descriptors to be used in QSAR studies on peptides and proteins, readers may refer to the following works: ref. [133] (a review paper) and ref. [134] (a research article).

As demonstrated above, efforts to decipher the determinants of AQPs' filtering and selectivity properties have been made [14,15,43–47]. Most of them, however, have predominantly focused on individual features of these proteins, as for instance, the amino acid compositions of the NPA and SF motifs, the pore gating, or the pore shape and size, to name a few. Moreover, the challenges that experimentalists continue to face in obtaining direct and reproducible data [44]

(introduced in **Section 3**) have perhaps limited the acquisition of permeation data for many AQPs (as demonstrated by the limited number of entries in the Table S1), which hinders extensive analyses.

Modeling the permeation of aquaporins entails additional challenges. First, the complex nature of this transport phenomenon is determined by a combination of local and global features, both inside and outside the pore, and associated with events such as auto-regulatory mechanisms (see pore gating, introduced in **Section 5**), which depends on post-translational modifications at the periphery of the pore [9,84,121–124], or the voltage-induced pore gating [44,135]. Second, identifying pore descriptors or features that accurately capture their specific properties seems, a priori, a non-trivial task.

While aware of all these current challenges, we believe that the potential of methods —such as QSAR— to identify new patterns in high-dimensional complex processes, like membrane permeation [136–138], makes their application highly appealing for AQP-based systems. QSAR could provide deeper insights at both the molecular and residue levels, offering a better understanding of the AQPs’ functioning, and creating opportunities for the rational improvement of their properties and for targeted interventions in disease-related contexts. This has motivated us to propose here a QSAR methodology based on pore characteristics in relation to water permeability. Therefore, although the available experimental permeation rate (p_f) data is currently limited (see Table S1 and Figure 3), we conduct a proof-of-concept ‘pore-level QSAR²’ study with the set of ten (10) AQPs —from our list of 22 selected—, for which experimental measurements are reported.

6.1. Pore Descriptors, Training Set, QSAR Modeling and Performance

Intuitive and comprehensive descriptors for permeable pores such as their diameter (Figure 5, panel A, top, and Figure S3, left top panels) and regularity (Table S3), as well as the amino acids lining the pore (**Supplementary Files**) were obtained using the PoreWalker tool [119]. Furthermore, based on the pore lining composition, two very informative and typically important properties were obtained per amino acid: the hydrophobicity index (the Kyte-Doolittle scale [139]), calculated by Discovery Studio [128], and the B-factor, extracted from the PDB files. These per-residue properties have also been plotted along the x-coordinate of the pore (Figure 5, panel A, bottom, and Figure S3, left bottom panels).

The Kyte-Doolittle hydrophobicity scale ranges from -4.5 , the most hydrophilic value for Arg, to 4.5 , the most hydrophobic value for Ile, with Gly being the most amphipathic residue (-0.4). Hydrophobicity profiles obtained for the AQPs here investigated (Figure 5, panel A, bottom, and Figure S3, left bottom panels) show significantly more hydrophobic residues (positive indexes) lining the pore than hydrophilic ones (negative indexes). These differences are less pronounced near and at the intra- and extracellular interfaces, where the pore diameter and water contact surface increase, and there is a higher concentration of hydrophilic residues. The hydrophobicity profiles, thus, predominantly show a downward bell-shaped smoothed curve, with the peak located around the central part of the pore, where the NPA and SF motifs are situated. It is important to note that, although hydrophobic residues predominate, in particular in the central region of the pore, the presence of hydrophilic residues interspersed among them could be essential for water passage [48,97]. Moreover, the B-factor profiles displayed the opposite shape, that is, an upward bell smoothed curve (Figure 5, panel A, bottom, and Figure S3, left bottom panels). The B-factor measures the atomic displacement or flexibility in molecular structures, indicating how much atoms deviate from their average positions due to thermal motion or structural disorder. According to these graphs, residues in the pore with the lowest flexibility are located in the region encompassing the pore constriction sites, namely the SF and NPA motifs. This is likely due to the proximity of the pore walls, which facilitates the formation of interaction networks (**Section 2.3**) that are crucial for the transport and selectivity exhibited by these proteins.

All in all, eight pore descriptors (PDs) (see **Section 8.4**) were selected to conduct the pore-level QSAR modeling on the following aquaporins with reported experimental permeation rate (henceforth PR) and structure: bAqp0, oAqp0, bAqp1, hAqp1, hAqp2, hAqp4, rAqp4, mAqpM, eAqpZ and eGlpF. Given the small number of PR data points available (10), we decided to use this entire dataset as training set. Experimental PR averages were used in the cases where more than one measurement has been collected. PR values for this AQPs dataset range between $0.15 (\pm 0.1)$ for bovine Aqp0 and $23 (\pm 1.0)$ for rat Aqp4, with a mean of $5.91 (\pm 2.25) (\times 10^{-14} \text{ cm}^3 \cdot \text{s}^{-1})$, Table S1). After aligning and equalizing (by trimming the ends, see Figure S5) the x-coordinates of all AQPs’ pores (x-coordinate range between -20 and 17.5 \AA ,

see the **Materials and Methods** section and the corresponding Supplementary section), the PDs were calculated. Some of them (Regularity, Ave_Bfac, Ave_Bfac_BB and Ave_Bfac_SC) were internally normalized to ensure consistency on the same scale (0–10) across all, and the entire PD dataset was then standardized prior to modeling.

Ordinary Least Squares (OLS) regression was combined with the LASSO (Least Absolute Shrinkage and Selection Operator) regularization method [140] for the modeling. The LASSO method enables feature (PD) selection and the application of stronger penalties to PDs exhibiting significant multicollinearity, thereby preventing their inclusion in the models. This procedure led to simplified models and reduced the risk of overfitting and model instability. The final LASSO coefficients are provided in Figure S6. To obtain the best-performing models that included two or more PDs, we first examined the autocorrelation matrix and the variance inflation factors (VIF) of the PDs. Models where the PDs showed intercorrelation greater than 0.4 (in absolute value) and VIF exceeding 5 were discarded. Another relevant metric, the condition number (CN), was also calculated to assess the sensitivity of the regression coefficients to perturbations in the data. In this case, models with $CN > 10$ were considered unstable and of no interest. Considering all these aspects, models obtained that included three or more PDs exhibited significant multicollinearity and instability, and were therefore discarded, even though some showed good fitting (not shown).

Here, we present the best single-PD and two-PD models, which exhibit good fittings (R^2) and reasonable internal predictabilities, LOO- Q^2 (see all the statistical parameters in Table S4):

$$PR = 5.75(\pm 1.26) * Ave_Bfac_SC + 5.91(\pm 1.26); R^2 = 0.72, LOO-Q^2 = 0.40 \quad \text{(Model 1),}$$

$$PR = 5.43(\pm 1.10) * Ave_Bfac_SC + 2.14(\pm 1.10) * Ave_diam + 5.91(\pm 1.08); R^2 = 0.82, LOO-Q^2 = 0.55 \quad \text{(Model 2).}$$

Model 1 (p-value = 0.002) reveals that the descriptor Ave_Bfac_SC alone accounts for an impressive 72 % of the PR variability. Model 2 (p-value = 0.002), which includes the pore average diameter (Ave_diam), still reaches a substantial R^2 of 0.82. However, it should be pointed out that Ave_diam appears in this model with a lower coefficient (Table S4) and results in only a minimal increase in R^2 compared to Model 1. PR residuals derived from Models 1 and 2 followed a normal distribution (not shown) and did not exceed the absolute value of 5.7 and $4.5 \times 10^{-14} \text{ cm}^3 \cdot \text{s}^{-1}$ (Table S5), respectively (averages of 2.98 and $2.36 \times 10^{-14} \text{ cm}^3 \cdot \text{s}^{-1}$), despite the simplicity of these predictive models. The application of the *y*-scrambling technique (with 100 permutations) did not produce a single scrambled model with R^2 and LOO- Q^2 values better than those of the original model suggesting that random fitting could be ruled out (Figure S7). *Y*-scrambling approach is implemented in the Python script used for model training and evaluation (see **Supplementary File**).

As previously described, parameters such as the pore diameter, hydrophobicity/hydrophilicity, and B-factors show significant variability along the pore's *x*-coordinate (Figure 5 and Figure S3). This suggests that the correlation found in models containing these PDs may vary when considering smaller sections of the pore. If observed, this would confirm the longitudinal impact of such descriptors on PR variability. In this regard, we obtained 5 additional reduced pore segments by trimming their ends at the *x*-coordinates indicated in Table S4, and proceeded in the same manner to find the best models for each one. Two important aspects stand out from the resulting models: first, all models invariably and significantly included the predictor Ave_Bfac_SC, both in the best single- and two-PD models (exhibiting positive coefficients); and second, a variation in the correlation of the models across the different pore trimmings is exhibited, as anticipated.

The first of these findings highlights the importance of pore flexibility in relation to water permeation of AQPs. Flexibility has been shown to be crucial for pore gating events [44,84,121–124] (see **Section 5**), which allows for direct regulation of pore permeation. However, none of the AQPs included here in the modeled training set has been shown to exhibit pore gating. Therefore, the high correlation observed between PR and pore flexibility, captured through the descriptor Ave_Bfac_SC, should not be explained by conformational changes associated to this molecular event (Figure S4). Instead, it may be related to the entire set of amino acids lining the pores, particularly their side chain flexibilities, which are indeed reflected in Ave_Bfac_SC. In the models, the positive coefficients associated to Ave_Bfac_SC reveal that pores with greater average side chain flexibility will allow for higher water flux. From a physico-chemical perspective, this may suggest that faster dynamics of the pore-lining residues prevents stronger and therefore more persistent

interactions between these residues and the single-file water molecules (via hydrogen bond formation, for instance). Otherwise, it may increase friction and hinder water passage [141]. This role of protein flexibility in coupling water and protein dynamics has been observed in molecular dynamics simulations of prototypical peptides and proteins [142].

The second aspect extracted from these models (Table S4): the variation in correlation (R^2) and predictive power (LOO- Q^2) of the models across the different pore trimmings —particularly for single-PD models, i.e., those that include only the Ave_Bfac_SC descriptor—, clearly reflect the sensitivity of PR to the pore longitudinal changes in flexibility (see B-factor profiles in Figure 5 and Figure S3). In this context, the weakest correlation (R^2) and the smaller coefficient associated to Ave_Bfac_SC, observed, for instance, in the models for the pore segment from -5 to 5 Å —where flexibility (Ave_Bfac_SC) decreases due to the rigidification caused by the proximity of the pore walls—, suggests that if the overall flexibility of the pore were similar to that of this segment, this property would be less relevant in the process, and the PR of AQPs would also decrease. In other words, this confirms the importance of flexibility for AQPs permeation and demonstrates the value of the applied segmentative pore-level QSAR modeling for uncovering this kind of hidden relevant information for the process under analysis, which could be difficult to reveal by other approaches.

Furthermore, the inclusion of Ave_diam in the best two-PD models obtained for each of the pore trimmings (Table S4) suggests that this descriptor —although it explains less of the PR variability compared to Ave_Bfac_SC— is still important. Likewise, the absence of the descriptor Min_diam in all of these models confirms the virtually non-existent linear correlation with the AQPs' water permeation rate, as shown in **Section 5**. What the above suggests is that the determinants of the water permeation process in aquaporins are both integral and complex, and cannot be attributed solely to one or two structural elements, such as the NPA regions and the SF, which determinate the constriction region. Studying these elements individually when investigating the filtration process in AQPs is important, but to precisely understand all of the determinants and how they interact with each other, a comprehensive analysis is required. Such complexity invites the evaluation of nonlinear approaches. A preliminary evaluation using non-linear regression (not shown) resulted in some models exhibiting reasonable performance, but with stronger collinearity between the selected descriptors, which led to their disregard. More advanced approaches using neural networks or deep learning [136–138] may provide additional opportunities, however, more training data would typically be required.

6.2. Challenges and Main Limitations of the Proposed Methodology

QSAR models presented here offer valuable insights, although they are accompanied by certain limitations due to the reduced size of the training (10 AQPs). The observed LOO- Q^2 values, while reasonable, highlight areas for improvement. The absence of a test set has prevented us to perform external validation, and no applicability domain was calculated. Nevertheless, this does not reduce the utility of the models in providing a deeper residue-level understanding of the relationships between structural features and pore permeation properties.

Similarly, although the relevance of the side chain flexibility of the pore-lining residues has been demonstrated, the fact that this property is calculated here based on experimental B-factors (from the crystals in the PDBs, Tables 1 and 2) could pose some challenges. It should be pointed out that we used the AQP structures (wild-type) resolved with the highest resolution among all available. However, there are slight differences in the resolutions of these structures, as well as in the experimental conditions, equipment, and other elements related to their structural resolution (see Table S6). Considering this, in order to equalize the B-factors across all the PDB structures and to avoid scaling issues, we individually normalized the values of all the AQPs between 0 and 1. Before that, we aligned the structures and trimmed the protruding (over the alignment) N- and C-terminal ends of those AQPs with longer chains, as these regions typically exhibit the greatest relative flexibilities. Otherwise, the normalization would not have been reliable enough.

Moreover, it is evident that the large scatter associated to some individual AQP's permeation rate data obtained experimentally adds uncertainty to the QSAR modeling performed. All this emphasizes the need for enhanced experimental efforts in the determination of reliable permeation measurements of AQPs to advance this type of methodologies. In addition, as the application of this approach here serves only as a proof of concept, we explored a limited number of pore descriptors for demonstrative purposes. However, there is still large room to develop and propose new descriptive features of pore water filtration and selectivity, which should be incorporated as new and more accurate experimental data —or in silico data from molecular dynamics simulations— become available. In this regard, the computational

community could also contribute significantly to improving MDS-based modeling methodologies for AQPs, especially now that we have access to remarkable tools like AlphaFold [143,144] and unprecedented computational power.

7. Conclusions

In this work, we addressed a systematic analysis of the main features of AQPs—a family of biomolecules with significant applications in various fields of research and technology—at the highest resolution and broadest known structural scale. The analysis included pairwise sequence and structure comparisons, residue-level information on protein structure and properties, and composition at both the pore and whole protein scales. This information was cross-referenced and analyzed against a compilation of reported functional data on permeation rates measured experimentally and/or in silico. Additionally, a pore-level QSAR approach, presented as a methodological proof of concept, has proven useful in identifying key characteristics influencing water permeation through the pores, such as pore-lining flexibility, represented through the B-factors of the pore-lining amino acid side chains. The best QSAR models achieved, while showing good correlation and reasonable predictive performance, currently lack the predictive power necessary for real-case applications. This limitation is primarily due to the scarcity of experimental permeation rate data for AQPs, which hinders the use of broader training sets. However, this issue does not diminish the utility of the models for gaining a deeper residue-level understanding of AQPs' filtering properties. We believe that the methodology, therefore, holds great promise and could help advance—once additional permeation data become available—the rational design of highly efficient AQPs or other biomimetic molecules with desired filtration properties, as well as provide insights into the molecular mechanisms underlying AQP-related diseases.

8. Materials and Methods

8.1. PDB Structures of Collected AQPs

A search for proteins of the MIP family was performed on two different databases, namely PROSITE [145,146] and InterPro [147,148]. Proteins with available 3D structures identified in the initial search were subsequently retrieved from the RCSB PDB archive [149].

The PROSITE database [145,146], returned 285 entries (with accession code PS00221 related to MIP family, by March 2024). Out of the true positive sequences (264), 53 structure entries were available on the PDB archive according to this database. The InterPro database [147,148], which contained all the structure entries reported in PROSITE, returned (with accession code IPR000425 related to MIP family, by March 2024) 73 different PDB structures. This number of structures represented 22 individual aquaporins. In cases where multiple structures were available for a protein, the one with the highest structural resolution among those with canonical sequences (no mutations) was selected as its representative structure. An overview of these 22 AQPs and their respective PDB IDs is reported in Table 2.

8.2. Pore Shape Prediction with PoreWalker Server

Pore shape and size analysis of the AQPs was done via the PoreWalker online tool [119], using the selected PDB structures referred in Table 2. The initial chain of each tetrameric AQP structure was uploaded to the server for calculation, and the resulting data was subsequently processed. The server's output includes the calculation of the pore diameter profile, 3D shape regularity, 2D projection of the pore shape, cross-sectional images of the pore, as well the composition of amino acids lining the pore. The output files issued by PoreWalker for the AQPs studied are provided as **Supplementary Files**.

8.3. Training Set, Pore Descriptors and Pore-level QSAR Modeling

The set of 10 AQPs with available experimental measurements of water permeability rate (PR) was used as the training set to conduct the pore-level QSAR study, namely: bAqp0, oAqp0, bAqp1, hAqp1, hAqp2, hAqp4, rAqp4, mAqpM, eAqpZ and eGlpF (see Table S1 and Figure 3). A set of eight (8) pore descriptors (PDs) is used to conduct the modeling. Based on the pore features obtained by PoreWalker [119] (diameter, regularity and amino acid composition) and by Discovery Studio (Kyte-Doolittle hydrophobicity) [128], along with flexibility from atomic B-factors (from the PDBs),

we established the following simple descriptors that could be a priori related with the AQPs' permeability: 1) average diameter (Ave_diam, in Å), 2) minimum diameter (Min_diam, in Å), 3) regularity, 4) average hydrophobicity (Ave_hydropho), 5) average hydrophilicity (Ave_hydrophi), 6) average B-factor (Ave_Bfac), 7) average side chain B-factor (Ave_Bfac_SC), and 8) average backbone B-factor (Ave_Bfac_BB).

To ensure uniform conditions and reduce uncertainty across all AQPs, the x -coordinate of the pores was equalized by setting the minimum and maximum values to -20 and 17.5 Å, respectively, trimming the pore ends (intra- and extracellularly) accordingly (see Figure S5). Additional pore trimmings were also evaluated, where the x -coordinate length of the pores was further shortened by the ends (Table S4). PDs for all these trimmed pores were calculated and treated statistically. The iterative regularization technique LASSO (Least Absolute Shrinkage and Selection Operator) [140] was used, along with the Ordinary Least Squares (OLS) multiple linear regression method (MLR), to select the best combination of PDs for QSAR modeling, aiming to prevent multicollinearity and overfitting as much as possible. The statistical and predictive parameters of the obtained best-performing models are provided in Table S4. Auto-correlation analysis, and y -scrambling to rule out random fitting, are conducted. All the PD datasets generated and used throughout the described methodology are provided as **Supplementary Files**. For further details, please refer to the **Supplementary Materials and Methods** section.

Table 2. Overview of AQPs and selected 3D structures.

Molecule (short name)	PDB ID	Source organism	Ref. ^a
Aquaporin 0 (bAqp0)	1YMG	<i>Bos taurus</i>	[72]
Aquaporin 0 (oAqp0)	2B6O	<i>Ovis aries</i>	[73]
Aquaporin 1 (bAqp1)	1J4N	<i>Bos Taurus</i>	[56]
Aquaporin 1 (hAqp1)	7UZE	<i>Homo sapiens</i>	[76]
Aquaporin 1 (aAqp1)	7W7S	<i>Anabas testudineus</i>	[150]
Aquaporin 1 (kAqp1)	3ZOJ	<i>Komagataella pastoris</i>	[151]
Aquaporin 2 (hAqp2)	4NEF	<i>Homo sapiens</i>	[67]
Aquaporin 4 (hAqp4)	3GD8	<i>Homo sapiens</i>	[64]
Aquaporin 4 (rAqp4)	2D57	<i>Rattus norvegicus</i>	[83]
Aquaporin 5 (hAqp5)	3D9S	<i>Homo sapiens</i>	[63]
Aquaporin 7 (hAqp7)	6QZI	<i>Homo sapiens</i>	[74]
Aquaporin 10 (hAqp10)	6F7H	<i>Homo sapiens</i>	[87]
Aquaporin (soPIP2;1)	1Z98	<i>Spinacia oleracea</i>	[84]
Aquaporin M (mAqpM)	2F2B	<i>Methanothermobacter marburgensis</i>	[60]
Probable aquaporin M (aAqpM)	3NE2	<i>Archaeoglobus fulgidus</i>	[152]
Aquaporin NIP2;1 (osNIP2;1)	7CJS	<i>Oryza sativa japonica</i>	[153]
Aquaporin TIP2;1 (atTIP2;1)	5I32	<i>Arabidopsis thaliana</i>	[88]
Probable aquaporin PIP2;4 (atPIP2;4)	6QIM	<i>Arabidopsis thaliana</i>	[86]
Aquaporin Z (eAqpZ)	1RC2	<i>Escherichia coli</i>	[57]
Aquaporin Z 2 (aAqpZ2)	3LLQ	<i>Agrobacterium fabrum</i>	[85]
Aquaglyceroporin (pAqgp)	3C02	<i>Plasmodium falciparum</i>	[75]
Glycerol uptake facilitator protein (eGlpF)	1FX8	<i>Escherichia coli</i>	[48]

^a Reference articles for structures 3LLQ and 3NE2 are not yet available. In these cases the references provided are the links to the entries in the RCSB Protein Data Bank [149].

Supplementary Information: This article has an associated Supplementary Information document, and Supplementary Information Files are provided in this link: <https://shorturl.at/S1yTJ>.

Author Contributions: **Juan José Galano-Frutos:** Conceptualization, Methodology, Software, Validation, Formal analysis, Investigation, Data curation, Writing - Original draft preparation, Writing - Reviewing and Editing, Visualization, Project administration; **Luca Bergamasco:** Conceptualization, Methodology, Software, Validation, Formal analysis, Investigation, Data curation, Writing - Original draft preparation, Writing - Reviewing and Editing, Visualization, Project administration; **Paolo Vigo:** Investigation, Data curation, Writing - Original draft preparation; **Matteo Morciani:** Writing - Reviewing and Editing; **Matteo Fasano:** Writing - Reviewing and Editing; **Davide Pirolli:** Writing - Reviewing and Editing; **Eliodoro Chiavazzo:** Writing - Reviewing and Editing; **Maria Cristina de Rosa:** Writing - Reviewing and Editing, Supervision.

Conflicts of Interest: The authors declare no conflicts of interest. The funders had no role in the design of the study; in the collection, analyses, or interpretation of data; in the writing of the manuscript; or in the decision to publish the results.

References

1. Preston, G.M.; Carroll, T.P.; Guggino, W.B.; Agre, P. Appearance of Water Channels in *Xenopus* Oocytes Expressing Red Cell CHIP28 Protein. *Science* **1992**, *256*, 385–387, doi:10.1126/science.256.5055.385.
2. Agre, P.; Sasaki, S.; Chrispeels, M.J. Aquaporins: A Family of Water Channel Proteins. *American Journal of Physiology-Renal Physiology* **1993**, doi:10.1152/ajprenal.1993.265.3.F461.
3. Agre, P.; Borgnia, M.J.; Yasui, M.; Neely, J.D.; Carbrey, J.; Kozono, D.; Beitz, E.; Hoffert, J.; Leitch, V.; King, L.S. Discovery of the Aquaporins and Their Impact on Basic and Clinical Physiology. *Curr Top Membr* **2001**, *51*, 1–38, doi:10.1016/S1063-5823(01)51003-0.
4. Tajkhorshid, E.; Nollert, P.; Jensen, M.Ø.; Miercke, L.J.; O’Connell, J.; Stroud, R.M.; Schulten, K. Control of the Selectivity of the Aquaporin Water Channel Family by Global Orientational Tuning. *Science (New York, N.Y.)* **2002**, *296*, 525–530, doi:10.1126/science.1067778.
5. Goto, S.G.; Lee, R.E.; Denlinger, D.L. Aquaporins in the Antarctic Midge, an Extremophile That Relies on Dehydration for Cold Survival. *The Biological Bulletin* **2015**, *229*, 47–57, doi:10.1086/BBLv229n1p47.
6. Gautam, A.; Pandey, A.K. Aquaporins Responses under Challenging Environmental Conditions and Abiotic Stress Tolerance in Plants. *Bot. Rev.* **2021**, *87*, 467–495, doi:10.1007/s12229-021-09249-z.
7. Kapilan, R.; Vaziri, M.; Zwiazek, J.J. Regulation of Aquaporins in Plants under Stress. *Biological Research* **2018**, *51*, 4, doi:10.1186/s40659-018-0152-0.
8. Philip, B.N.; Kiss, A.J.; Lee, R.E. The Protective Role of Aquaporins in the Freeze-Tolerant Insect *Eurosta Solidaginis* : Functional Characterization and Tissue Abundance of EsAQP1. *Journal of Experimental Biology* **2011**, *214*, 848–857, doi:10.1242/jeb.051276.
9. *Aquaporins*; Yang, B., Ed.; Advances in Experimental Medicine and Biology; Second Edition.; Springer Nature: Singapore, 2023; Vol. 1398; ISBN 978-981-19741-4-4.
10. Verkman, A.S. Aquaporins in Clinical Medicine. *Annu Rev Med* **2012**, *63*, 303–316, doi:10.1146/annurev-med-043010-193843.
11. Verkman, A.S. Aquaporins. *Current Biology* **2013**, *23*, R52–R55, doi:10.1016/j.cub.2012.11.025.

12. Azad, A.K.; Raihan, T.; Ahmed, J.; Hakim, A.; Emon, T.H.; Chowdhury, P.A. Human Aquaporins: Functional Diversity and Potential Roles in Infectious and Non-Infectious Diseases. *Front Genet* **2021**, *12*, 654865, doi:10.3389/fgene.2021.654865.
13. Dutta, A.; Das, M. Deciphering the Role of Aquaporins in Metabolic Diseases: A Mini Review. *The American Journal of the Medical Sciences* **2022**, *364*, 148–162, doi:10.1016/j.amjms.2021.10.029.
14. Kruse, E.; Uehlein, N.; Kaldenhoff, R. The Aquaporins. *Genome Biology* **2006**, *7*, 206, doi:10.1186/gb-2006-7-2-206.
15. Krane, C.M.; Goldstein, D.L. Comparative Functional Analysis of Aquaporins/Glyceroporins in Mammals and Anurans. *Mammalian genome : official journal of the International Mammalian Genome Society* **2007**, *18*, 452–462, doi:10.1007/s00335-007-9041-5.
16. Suzuki, M.; Shibata, Y.; Ogushi, Y.; Okada, R. Molecular Machinery for Vasotocin-Dependent Transepithelial Water Movement in Amphibians: Aquaporins and Evolution. *The Biological Bulletin* **2015**, *229*, 109–119, doi:10.1086/BBLv229n1p109.
17. Tong, H.; Hu, Q.; Zhu, L.; Dong, X. Prokaryotic Aquaporins. *Cells* **2019**, *8*, 1316, doi:10.3390/cells8111316.
18. Pettersson, N.; Filipsson, C.; Becit, E.; Brive, L.; Hohmann, S. Aquaporins in Yeasts and Filamentous Fungi. *Biol Cell* **2005**, *97*, 487–500, doi:10.1042/BC20040144.
19. Kumar, M.; Grzelakowski, M.; Zilles, J.; Clark, M.; Meier, W. Highly Permeable Polymeric Membranes Based on the Incorporation of the Functional Water Channel Protein Aquaporin Z. *Proc Natl Acad Sci U S A* **2007**, *104*, 20719–20724, doi:10.1073/pnas.0708762104.
20. Yang, Z.; Wu, C.; Tang, C.Y. Making Waves: Why Do We Need Ultra-Permeable Nanofiltration Membranes for Water Treatment? *Water Res X* **2023**, *19*, 100172, doi:10.1016/j.wroa.2023.100172.
21. Nielsen, C.H. Biomimetic Membranes for Sensor and Separation Applications. *Anal Bioanal Chem* **2009**, *395*, 697–718, doi:10.1007/s00216-009-2960-0.
22. Li, Y.; Qi, S.; Tian, M.; Widjajanti, W.; Wang, R. Fabrication of Aquaporin-Based Biomimetic Membrane for Seawater Desalination. *Desalination* **2019**, *467*, 103–112, doi:10.1016/j.desal.2019.06.005.
23. Güvensoy-Morkoyun, A.; Velioglu, S.; Gökтуğ, M.A.; Tantekin-Ersolmaz, S.B. Desalination Potential of Aquaporin-Inspired Functionalization of Carbon Nanotubes: Bridging Between Simulation and Experiment. *ACS Applied Materials & Interfaces* **2022**, *14*, 28174–28185, doi:10.1021/acsami.2c03700.
24. Tang, C.; Wang, Z.; Petrinić, I.; Fane, A.G.; Hélix-Nielsen, C. Biomimetic Aquaporin Membranes Coming of Age. *Desalination* **2015**, *368*, 89–105, doi:10.1016/j.desal.2015.04.026.
25. Tang, C.Y.; Zhao, Y.; Wang, R.; Hélix-Nielsen, C.; Fane, A.G. Desalination by Biomimetic Aquaporin Membranes: Review of Status and Prospects. *Desalination* **2013**, *308*, 34–40, doi:10.1016/j.desal.2012.07.007.
26. Hélix-Nielsen, C. Biomimetic Membranes as a Technology Platform: Challenges and Opportunities. *Membranes* **2018**, *8*, doi:10.3390/membranes8030044.
27. Azarafza, A.; Islam, M.A.; Golpazirsorkheh, Y.; Efteghar, I.; Sadrzadeh, M.; Kamkar, M.; Shojaei, A.F.; Younas, M.; Aminabhavi, T.M.; Rezakazemi, M. Aquaporin-Based Biomimetic Membranes for Low Energy Water Desalination and Separation Applications. *Advanced Functional Materials* **2023**, *33*, 2213326, doi:10.1002/adfm.202213326.

28. Shannon, M.A.; Bohn, P.W.; Elimelech, M.; Georgiadis, J.G.; Mariñas, B.J.; Mayes, A.M. Science and Technology for Water Purification in the Coming Decades. *Nature* **2008**, *452*, 301–310, doi:10.1038/nature06599.
29. Space-Age Water Conservation | NASA Spinoff Available online: <https://spinoff.nasa.gov/page/space-age-water-conservation-nasa> (accessed on 27 April 2024).
30. Atkinson, S. Aquaporin's Membranes Play a Vital Role in Effectively Cleaning Both Produced and Oil and Gas Flow-Back Water. *Membrane Technology* **2020**, *2020*, 5–6, doi:10.1016/S0958-2118(20)30107-5.
31. Beratto-Ramos, A.; Dagnino-Leone, J.; Martínez-Oyanedel, J.; Aranda, M.; Bórquez, R. Fabrication and Filtration Performance of Aquaporin Biomimetic Membranes for Water Treatment. *Separation & Purification Reviews* **2022**, *51*, 340–357, doi:10.1080/15422119.2021.1948865.
32. Grzelakowski, M.; Cherenet, M.F.; Shen, Y.X.; Kumar, M. A Framework for Accurate Evaluation of the Promise of Aquaporin Based Biomimetic Membranes. *Journal of Membrane Science* **2015**, *479*, 223–231, doi:10.1016/j.memsci.2015.01.023.
33. Abdelrasoul, A.; Doan, H.; Lohi, A.; Cheng, C.-H. Aquaporin-Based Biomimetic and Bioinspired Membranes for New Frontiers in Sustainable Water Treatment Technology: Approaches and Challenges. *Polymer Science, Series A* **2018**, *60*, 429–450, doi:10.1134/S0965545X18040016.
34. Cohen-Tanugi, D.; McGovern, R.K.; Dave, S.H.; Lienhard, J.H.; Grossman, J.C. Quantifying the Potential of Ultra-Permeable Membranes for Water Desalination. *Energy Environ. Sci.* **2014**, *7*, 1134–1141, doi:10.1039/C3EE43221A.
35. Fasano, M.; Morciano, M.; Bergamasco, L.; Chiavazzo, E.; Zampato, M.; Carminati, S.; Asinari, P. Deep-Sea Reverse Osmosis Desalination for Energy Efficient Low Salinity Enhanced Oil Recovery. *Applied Energy* **2021**, *304*, 117661, doi:10.1016/j.apenergy.2021.117661.
36. Qasim, M.; Badrelzaman, M.; Darwish, N.N.; Darwish, N.A.; Hilal, N. Reverse Osmosis Desalination: A State-of-the-Art Review. *Desalination* **2019**, *459*, 59–104, doi:10.1016/j.desal.2019.02.008.
37. Morciano, M.; Fasano, M.; Bergamasco, L.; Albiero, A.; Curzio, M.L.; Asinari, P.; Chiavazzo, E. Sustainable Freshwater Production Using Passive Membrane Distillation and Waste Heat Recovery from Portable Generator Sets. *Applied Energy* **2020**, *258*, 114086, doi:10.1016/j.apenergy.2019.114086.
38. Antonetto, G.; Morciano, M.; Alberghini, M.; Malgaroli, G.; Ciocia, A.; Bergamasco, L.; Spertino, F.; Fasano, M. Synergistic Freshwater and Electricity Production Using Passive Membrane Distillation and Waste Heat Recovered from Camouflaged Photovoltaic Modules. *Journal of Cleaner Production* **2021**, *318*, 128464, doi:10.1016/j.jclepro.2021.128464.
39. Kocsis, I.; Sun, Z.; Legrand, Y.M.; Barboiu, M. Artificial Water Channels—Deconvolution of Natural Aquaporins through Synthetic Design. *npj Clean Water* **2018**, *1*, 1–11, doi:10.1038/s41545-018-0013-y.
40. Song, W.; Kumar, M. Artificial Water Channels: Toward and beyond Desalination. *Current Opinion in Chemical Engineering* **2019**, *25*, 9–17, doi:10.1016/j.coche.2019.06.007.
41. Andrei, I.M.; Chaix, A.; Benkhaled, B.T.; Dupuis, R.; Gomri, C.; Petit, E.; Polentarutti, M.; van der Lee, A.; Semsarilar, M.; Barboiu, M. Selective Water Pore Recognition and Transport through Self-Assembled Alkyl-Ureido-Trianglamine Artificial Water Channels. *J. Am. Chem. Soc.* **2023**, *145*, 21213–21221, doi:10.1021/jacs.3c02815.

42. Vincenzo, M.D.; Tiraferri, A.; Musteata, V.E.; Chisca, S.; Sougrat, R.; Huang, L.B.; Nunes, S.P.; Barboiu, M. Biomimetic Artificial Water Channel Membranes for Enhanced Desalination. *Nature nanotechnology* **2021**, *16*, 190–196, doi:10.1038/s41565-020-00796-x.
43. Groot, B.L. de; Grubmüller, H. The Dynamics and Energetics of Water Permeation and Proton Exclusion in Aquaporins. *Current opinion in structural biology* **2005**, *15*, 176–183, doi:10.1016/j.sbi.2005.02.003.
44. Ozu, M.; Alvear-Arias, J.J.; Fernandez, M.; Caviglia, A.; Peña-Pichicoi, A.; Carrillo, C.; Carmona, E.; Otero-Gonzalez, A.; Garate, J.A.; Amodeo, G.; et al. Aquaporin Gating: A New Twist to Unravel Permeation through Water Channels. *International Journal of Molecular Sciences* **2022**, *23*, 12317, doi:10.3390/ijms232012317.
45. Ozu, M.; Galizia, L.; Acuña, C.; Amodeo, G. Aquaporins: More Than Functional Monomers in a Tetrameric Arrangement. *Cells* **2018**, *7*, 209, doi:10.3390/cells7110209.
46. Fu, D.; Lu, M. The Structural Basis of Water Permeation and Proton Exclusion in Aquaporins (Review). *Molecular Membrane Biology* **2007**, doi:10.1080/09687680701446965.
47. Structure, Dynamics, and Function of Aquaporins Available online: <https://www.ks.uiuc.edu/Research/aquaporins/> (accessed on 28 April 2024).
48. Fu, D.; Lisbon, A.; Miercke, L.J.; Weitzman, C.; Nollert, P.; Krucinski, J.; Stroud, R.M. Structure of a Glycerol-Conducting Channel and the Basis for Its Selectivity. *Science* **2000**, *290*, 481–486, doi:10.1126/science.290.5491.481.
49. de Groot, B.L.; Grubmüller, H. Water Permeation across Biological Membranes: Mechanism and Dynamics of Aquaporin-1 and GlpF. *Science* **2001**, *294*, 2353–2357, doi:10.1126/science.1066115.
50. Gonen, T.; Walz, T. The Structure of Aquaporins. *Quarterly Reviews of Biophysics* **2006**, *39*, 361–396, doi:10.1017/S0033583506004458.
51. Solenov, E.I.; Baturina, G.S.; Katkova, L.E.; Zarogiannis, S.G. Methods to Measure Water Permeability. In *Aquaporins*; Yang, B., Ed.; Springer Netherlands: Dordrecht, 2017; pp. 263–276 ISBN 978-94-024-1057-0.
52. Xiong, M.; Li, C.; Wang, W.; Yang, B. Protein Structure and Modification of Aquaporins. In *Aquaporins*; Yang, B., Ed.; Springer Nature: Singapore, 2023; pp. 15–38 ISBN 978-981-19741-5-1.
53. Dingwell, D.A.; Brown, L.S.; Ladizhansky, V. Structure of the Functionally Important Extracellular Loop C of Human Aquaporin 1 Obtained by Solid-State NMR under Nearly Physiological Conditions. *The journal of physical chemistry. B* **2019**, *123*, 7700–7710, doi:10.1021/acs.jpcc.9b06430.
54. Sachdeva, R.; Priyadarshini, P.; Gupta, S. Aquaporins Display a Diversity in Their Substrates. *The Journal of Membrane Biology* **2023**, *256*, 1–23, doi:10.1007/s00232-022-00257-7.
55. Groot, B.L. de; Engel, A.; Grubmüller, H. A Refined Structure of Human Aquaporin-1. *FEBS letters* **2001**, *504*, 206–211, doi:10.1016/S0014-5793(01)02743-0.
56. Sui, H.; Han, B.G.; Lee, J.K.; Walian, P.; Jap, B.K. Structural Basis of Water-Specific Transport through the AQP1 Water Channel. *Nature* **2001**, *41*, 872–878, doi:10.1038/414872a.
57. Savage, D.F.; Egea, P.F.; Robles-Colmenares, Y.; O’Connell 3rd, J.D.; Stroud, R.M. Architecture and Selectivity in Aquaporins: 2.5 a X-Ray Structure of Aquaporin Z. *PLoS biology* **2003**, *1*, E72, doi:10.1371/journal.pbio.0000072.

58. Jiang, J.; Daniels, B.V.; Fu, D. Crystal Structure of AqpZ Tetramer Reveals Two Distinct Arg-189 Conformations Associated with Water Permeation through the Narrowest Constriction of the Water-Conducting Channel. *The Journal of biological chemistry* **2006**, *281*, 454–460, doi:10.1074/jbc.M508926200.
59. Palanivelu, D.V.; Kozono, D.E.; Engel, A.; Suda, K.; Lustig, A.; Agre, P.; Schirmer, T. Co-Axial Association of Recombinant Eye Lens Aquaporin-0 Observed in Loosely Packed 3D Crystals. *Journal of molecular biology* **2006**, *355*, 605–611, doi:10.1016/j.jmb.2005.10.032.
60. Lee, J.K.; Kozono, D.; Remis, J.; Kitagawa, Y.; Agre, P.; Stroud, R.M. Structural Basis for Conductance by the Archaeal Aquaporin AqpM at 1.68 Å. *Proceedings of the National Academy of Sciences* **2005**, *102*, 18932–18937, doi:10.1073/pnas.0509469102.
61. Savage, D.F.; Stroud, R.M. Structural Basis of Aquaporin Inhibition by Mercury. *Journal of molecular biology* **2007**, *368*, 607–617, doi:10.1016/j.jmb.2007.02.070.
62. Tani, K.; Hiroaki, T.M.Y.; Kamegawa, A.; Nishikawa, K.; Tanimura, Y.; Fujiyoshi, Y. Mechanism of Aquaporin-4's Fast and Highly Selective Water Conduction and Proton Exclusion. *Journal of molecular biology* **2009**, *389*, 694–706, doi:10.1016/j.jmb.2009.04.049.
63. Horsefield, R.; Nordén, K.; Fellert, M.; Backmark, A.; Törnroth-Horsefield, S.; Scheltinga, A.C.T. van; Kvassman, J.; Kjellbom, P.; Johanson, U.; Neutze, R. High-Resolution x-Ray Structure of Human Aquaporin 5. *Proceedings of the National Academy of Sciences of the United States of America* **2008**, *105*, 13327–13332, doi:10.1073/pnas.0801466105.
64. Ho, J.D.; Yeh, R.; Sandstrom, A.; Chorny, I.; Harries, W.E.; Robbins, R.A.; Miercke, L.J.; Stroud, R.M. Crystal Structure of Human Aquaporin 4 at 1.8 Å and Its Mechanism of Conductance. *Proceedings of the National Academy of Sciences of the United States of America* **2009**, *106*, 7437–7442, doi:10.1073/pnas.0902725106.
65. Savage, D.F.; O'Connell 3rd, J.D.; Miercke, L.J.; Finer-Moore, J.; Stroud, R.M. Structural Context Shapes the Aquaporin Selectivity Filter. *Proceedings of the National Academy of Sciences of the United States of America* **2010**, *107*, 17164–17169, doi:10.1073/pnas.1009864107.
66. Carrillo, D.R.; Ying, L.T.Y.; Darwis, D.; Soon, C.H.; Cornvik, T.; Torres, J.; Lescar, J. Crystallization and Preliminary Crystallographic Analysis of Human Aquaporin 1 at a Resolution of 3.28 Å. *Acta crystallographica. Section F, Structural biology communications* **2014**, *70*, 1657–1663, doi:10.1107/S2053230X14024558.
67. Frick, A.; Eriksson, U.K.; Mattia, F. de; Oberg, F.; Hedfalk, K.; Neutze, R.; Grip, W.J. de; Deen, P.M.; Törnroth-Horsefield, S. X-Ray Structure of Human Aquaporin 2 and Its Implications for Nephrogenic Diabetes Insipidus and Trafficking. *Proceedings of the National Academy of Sciences of the United States of America* **2014**, *111*, 6305–6310, doi:10.1073/pnas.1321406111.
68. Lieske, J.; Cerv, M.; Kreida, S.; Komadina, D.; Fischer, J.; Barthelmess, M.; Fischer, P.; Pakendorf, T.; Yefanov, O.; Mariani, V.; et al. On-Chip Crystallization for Serial Crystallography Experiments and on-Chip Ligand-Binding Studies. *IUCrJ* **2019**, *6*, 714–728, doi:10.1107/S2052252519007395.
69. Murata, K.; Mitsuoka, K.; Hirai, T.; Walz, T.; Agre, P.; Heymann, J.B.; Engel, A.; Fujiyoshi, Y. Structural Determinants of Water Permeation through Aquaporin-1. *Nature* **2000**, *407*, 599–605, doi:10.1038/35036519.
70. King, L.; Kozono, D.; Agre, P. From Structure to Disease: The Evolving Tale of Aquaporin Biology. *Nature Reviews Molecular Cell Biology* **2004**, *5*, 687–698, doi:10.1038/nrm1469.

71. Cui, Y.; Bastien, D.A. Water Transport in Human Aquaporin-4: Molecular Dynamics (MD) Simulations. *Biochemical and biophysical research communications* **2011**, *412*, 654–659, doi:10.1016/j.bbrc.2011.08.019.
72. Harries, W.E.; Akhavan, D.; Miercke, L.J.; Khademi, S.; Stroud, R.M. The Channel Architecture of Aquaporin 0 at a 2.2-Å Resolution. *Proceedings of the National Academy of Sciences of the United States of America* **2004**, *101*, 14045–14050, doi:10.1073/pnas.0405274101.
73. Gonen, T.; Cheng, Y.; Sliz, P.; Hiroaki, Y.; Fujiyoshi, Y.; Harrison, S.C.; Walz, T. Lipid-Protein Interactions in Double-Layered Two-Dimensional AQP0 Crystals. *Nature* **2005**, *438*, 633–638, doi:10.1038/nature04321.
74. de Mare, S.W.; Venskutonytė, R.; Eltschkner, S.; de Groot, B.L.; Lindkvist-Petersson, K. Structural Basis for Glycerol Efflux and Selectivity of Human Aquaporin 7. *Structure* **2020**, *28*, 215–222, doi:10.1016/j.str.2019.11.011.
75. Newby, Z.E.; O’Connell III, J.; Robles-Colmenares, Y.; Khademi, S.; Miercke, L.J.; Stroud, R.M. Crystal Structure of the Aquaglyceroporin PfAQP from the Malarial Parasite Plasmodium Falciparum. *Nature structural & molecular biology* **2008**, *15*, 619–625, doi:10.1038/nsmb.1431.
76. Vallese, F.; Kim, K.; Yen, L.Y.; Johnston, J.D.; Noble, A.J.; Cali, T.; Clarke, O.B. Architecture of the Human Erythrocyte Ankyrin-1 Complex. *Nature Structural & Molecular Biology* **2022**, *29*, 706–718, doi:10.1038/s41594-022-00792-w.
77. Ren, G.; Reddy, V.S.; Cheng, A.; Melnyk, P.; Mitra, A.K. Visualization of a Water-Selective Pore by Electron Crystallography in Vitreous Ice. *Proceedings of the National Academy of Sciences of the United States of America* **2001**, *98*, 1398–1403, doi:10.1073/pnas.98.4.1398.
78. Araya-Secchi, R.; Garate, J.A.; Holmes, D.S.; Perez-Acle, T. Molecular Dynamics Study of the Archaeal Aquaporin AqpM. *BMC Genomics* **2011**, *12 Suppl 4*, S8, doi:10.1186/1471-2164-12-S4-S8.
79. The UniProt Consortium UniProt: The Universal Protein Knowledgebase in 2023. *Nucleic Acids Research* **2023**, *51*, D523–D531, doi:10.1093/nar/gkac1052.
80. Krenc, D.; Song, J.; Almasalmeh, A.; Wu, B.; Beitz, E. The Arginine-Facing Amino Acid Residue of the Rat Aquaporin 1 Constriction Determines Solute Selectivity According to Its Size and Lipophilicity. *Molecular Membrane Biology* **2014**, *31*, 228–238, doi:10.3109/09687688.2014.960493.
81. Gonen, T.; Sliz, P.; Kistler, J.; Cheng, Y.; Walz, T. Aquaporin-0 Membrane Junctions Reveal the Structure of a Closed Water Pore. *Nature* **2004**, *429*, 193–197, doi:10.1038/nature02503.
82. Reichow, S.L.; Clemens, D.M.; Freitas, J.A.; Németh-Calahan, K.L.; Heiden, M.; Tobias, D.J.; Hall, J.E.; Gonen, T. Allosteric Mechanism of Water-Channel Gating by Ca²⁺-Calmodulin. *Nature structural & molecular biology* **2013**, *20*, 1085–1092, doi:10.1038/nsmb.2630.
83. Hiroaki, Y.; Tani, K.; Kamegawa, A.; Gyobu, N.; Nishikawa, K.; Suzuki, H.; Walz, T.; Sasaki, S.; Mitsuoka, K.; Kimura, K.; et al. Implications of the Aquaporin-4 Structure on Array Formation and Cell Adhesion. *Journal of molecular biology* **2006**, *355*, 628–639, doi:10.1016/j.jmb.2005.10.081.
84. Törnroth-Horsefield, S.; Wang, Y.; Hedfalk, K.; Johanson, U.; Karlsson, M.; Tajkhorshid, E.; Neutze, R.; Kjellbom, P. Structural Mechanism of Plant Aquaporin Gating. *Nature* **2006**, *439*, 688–694, doi:10.1038/nature04316.

85. Liu, Q.; Hillerich, B.; Love, J.; NYCOMPS. RCSB Protein Data Bank, 3LLQ: Aquaporin Structure from Plant Pathogen *Agrobacterium Tumefaciens* Available online: <https://www.rcsb.org/structure/3llq> (accessed on 6 October 2023).
86. Wang, H.; Schoebel, S.; Schmitz, F.; Dong, H.; Hedfalk, K. Characterization of Aquaporin-Driven Hydrogen Peroxide Transport. *Biochimica et biophysica acta. Biomembranes* **2020**, *1862*, 183065, doi:10.1016/j.bbamem.2019.183065.
87. Gotfryd, K.; Mósca, A.F.; Missel, J.W.; Truelsen, S.F.; Wang, K.; Spulber, M.; Krabbe, S.; Hélix-Nielsen, C.; Laforenza, U.; Soveral, G.; et al. Human Adipose Glycerol Flux Is Regulated by a pH Gate in AQP10. *Nature communications* **2018**, *9*, 1–11, doi:10.1038/s41467-018-07176-z.
88. Kirscht, A.; Kaptan, S.S.; Bienert, G.P.; Chaumont, F.; Nissen, P.; Goot, B.L. de; Kjellbom, P.; Gourdon, P.; Johanson, U. Crystal Structure of an Ammonia-Permeable Aquaporin. *PLoS biology* **2016**, *14*, e1002411, doi:10.1371/journal.pbio.1002411.
89. Zeidel, M.L.; Ambudkar, S.V.; Smith, B.L.; Agre, P. Reconstitution of Functional Water Channels in Liposomes Containing Purified Red Cell CHIP28 Protein. *Biochemistry* **1992**, *31*, 7436–7440, doi:10.1021/bi00148a002.
90. Zeidel, M.L.; Nielsen, S.; Smith, B.L.; Ambudkar, S.V.; Maunsbach, A.B.; Agre, P. Ultrastructure, Pharmacologic Inhibition, and Transport Selectivity of Aquaporin CHIP in Proteoliposomes. *Biochemistry* **1994**, *33*, 1606–1615, doi:10.1021/bi00172a042.
91. Jensen, M.Ø.; Mouritsen, O.G. Single-Channel Water Permeabilities of *Escherichia Coli* Aquaporins AqpZ and GlpF. *Biophysical journal* **2006**, *90*, 2270–2284, doi:10.1529/biophysj.105.073965.
92. Walz, T.; Smith, B.L.; Zeidel, M.L.; Engel, A.; Agre, P. Biologically Active Two-Dimensional Crystals of Aquaporin CHIP. *Journal of Biological Chemistry* **1994**, *269*, 1583–1586, doi:10.1016/S0021-9258(17)42062-X.
93. Coury, L.A.; Mathai, J.C.; Prasad, G.V.; Brodsky, J.L.; Agre, P.; Zeidel, M.L. Reconstitution of Water Channel Function of Aquaporins 1 and 2 by Expression in Yeast Secretory Vesicles. *Am J Physiol* **1998**, *274*, F34–42, doi:10.1152/ajprenal.1998.274.1.F34.
94. Pohl, P.; Saparov, S.M.; Borgnia, M.J.; Agre, P. Highly Selective Water Channel Activity Measured by Voltage Clamp: Analysis of Planar Lipid Bilayers Reconstituted with Purified AqpZ. *Proceedings of the National Academy of Sciences* **2001**, *98*, 9624–9629, doi:10.1073/pnas.161299398.
95. Zhu, F.; Tajkhorshid, E.; Schulten, K. Theory and Simulation of Water Permeation in Aquaporin-1. *Biophysical journal* **2004**, *86*, 50–57, doi:10.1016/S0006-3495(04)74082-5.
96. Jensen, M.Ø.; Park, S.; Tajkhorshid, E.; Schulten, K. Energetics of Glycerol Conduction through Aquaglyceroporin GlpF. *Proc Natl Acad Sci U S A* **2002**, *99*, 6731–6736, doi:10.1073/pnas.102649299.
97. Hashido, M.; Ikeguchi, M.; Kidera, A. Comparative Simulations of Aquaporin Family: AQP1, AQPZ, AQP0 and GlpF. *FEBS letters* **2005**, *579*, 5549–5552, doi:10.1016/j.febslet.2005.09.018.
98. Hashido, M.; Kidera, A.; Ikeguchi, M. Water Transport in Aquaporins: Osmotic Permeability Matrix Analysis of Molecular Dynamics Simulations. *Biophysical journal* **2007**, *93*, 373–385, doi:10.1529/biophysj.106.101170.
99. Binesh, A.R.; Kamali, R. Molecular Dynamics Insights into Human Aquaporin 2 Water Channel. *Biophysical chemistry* **2015**, *207*, 107–113, doi:10.1016/j.bpc.2015.10.002.

100. Alberga, D.; Nicolotti, O.; Lattanzi, G.; Nicchia, G.P.; Frigeri, A.; Pisani, F.; Benfenati, V.; Mangiatordi, G.F. A New Gating Site in Human Aquaporin-4: Insights from Molecular Dynamics Simulations. *Biochimica et Biophysica Acta (BBA)-Biomembranes* **2014**, *1838*, 3052–3060, doi:10.1016/j.bbamem.2014.08.015.
101. Garate, J.-A.; English, N.J.; MacElroy, J.M.D. Human Aquaporin 4 Gating Dynamics in Dc and Ac Electric Fields: A Molecular Dynamics Study. *The Journal of Chemical Physics* **2011**, *134*, 055110, doi:10.1063/1.3529428.
102. Jung, J.S.; Bhat, R.V.; Preston, G.M.; Guggino, W.B.; Baraban, J.M.; Agre, P. Molecular Characterization of an Aquaporin cDNA from Brain: Candidate Osmoreceptor and Regulator of Water Balance. *Proc Natl Acad Sci U S A* **1994**, *91*, 13052–13056, doi:10.1073/pnas.91.26.13052.
103. Alishahi, M.; Kamali, R. Forced Diffusion of Water Molecules through Aquaporin-5 Biomembrane; a Molecular Dynamics Study. *Biophysics and physicobiology* **2018**, *15*, 255–262, doi:10.2142/biophysico.15.0_255.
104. Boytsov, D.; Hanneschlaeger, C.; Horner, A.; Siligan, C.; Pohl, P. Micropipette Aspiration-Based Assessment of Single Channel Water Permeability. *Biotechnol J* **2020**, *15*, e1900450, doi:10.1002/biot.201900450.
105. Moss, F.J.; Mahinthichaichan, P.; Lodowski, D.T.; Kowatz, T.; Tajkhorshid, E.; Engel, A.; Boron, W.F.; Vahedi-Faridi, A. Aquaporin-7: A Dynamic Aquaglyceroporin With Greater Water and Glycerol Permeability Than Its Bacterial Homolog GlpF. *Front Physiol* **2020**, *11*, 728, doi:10.3389/fphys.2020.00728.
106. Katano, T.; Ito, Y.; Ohta, K.; Yasujima, T.; Inoue, K.; Yuasa, H. Functional Characteristics of Aquaporin 7 as a Facilitative Glycerol Carrier. *Drug Metabolism and Pharmacokinetics* **2014**, *29*, 244–248, doi:10.2133/dmpk.DMPK-13-RG-121.
107. Palmgren, M.; Hernebring, M.; Eriksson, S.; Elbing, K.; Geijer, C.; Lasič, S.; Dahl, P.; Hansen, J.S.; Topgaard, D.; Lindkvist-Petersson, K. Quantification of the Intracellular Life Time of Water Molecules to Measure Transport Rates of Human Aquaglyceroporins. *J Membr Biol* **2017**, *250*, 629–639, doi:10.1007/s00232-017-9988-4.
108. Yue, K.; Jiang, J.; Zhang, P.; Kai, L. Functional Analysis of Aquaporin Water Permeability Using an Escherichia Coli-Based Cell-Free Protein Synthesis System. *Front. Bioeng. Biotechnol.* **2020**, *8*, doi:10.3389/fbioe.2020.01000.
109. Smith, B.L.; Agre, P. Erythrocyte Mr 28,000 Transmembrane Protein Exists as a Multisubunit Oligomer Similar to Channel Proteins. *J Biol Chem* **1991**, *266*, 6407–6415, doi:10.1016/S0021-9258(18)38133-X.
110. Zampighi, G.A.; Kreman, M.; Boorer, K.J.; Loo, D.D.F.; Bezanilla, F.; Chandy, G.; Hall, J.E.; Wright, E.M. A Method for Determining the Unitary Functional Capacity of Cloned Channels and Transporters Expressed in *Xenopus Laevis* Oocytes. *J. Membr Biol.* **1995**, *148*, 65–78, doi:10.1007/BF00234157.
111. Chandy, G.; Zampighi, G.A.; Kreman, M.; Hall, J.E. Comparison of the Water Transporting Properties of MIP and AQP1. *The Journal of membrane biology* **1997**, *159*, 29–39, doi:10.1007/s002329900266.
112. Van Hoek, A.N.; Wiener, M.; Bicknese, S.; Miercke, L.; Biwersi, J.; Verkman, A. Secondary Structure Analysis of Purified Functional CHIP28 Water Channels by CD and FTIR Spectroscopy. *Biochemistry* **1993**, *32*, 11847–11856, doi:10.1021/bi00095a013.
113. Schulte, D.J.; van Hoek, A.N. Functional Analysis and Association State of Water Channel (AQP-1) Isoforms Purified from Six Mammals. *Comparative Biochemistry and Physiology Part B: Biochemistry and Molecular Biology* **1997**, *118*, 35–43, doi:10.1016/S0305-0491(97)00015-1.

114. Van Hoek, A.; Verkman, A. Functional Reconstitution of the Isolated Erythrocyte Water Channel CHIP28. *Journal of Biological Chemistry* **1992**, *267*, 18267–18269, doi:10.1016/S0021-9258(19)36953-4.
115. Saboe, P.O.; Rapisarda, C.; Kaptan, S.; Hsiao, Y.-S.; Summers, S.R.; De Zorzi, R.; Dukovski, D.; Yu, J.; de Groot, B.L.; Kumar, M.; et al. Role of Pore-Lining Residues in Defining the Rate of Water Conduction by Aquaporin-0. *Biophysical Journal* **2017**, *112*, 953–965, doi:10.1016/j.bpj.2017.01.026.
116. Yang, B.; Verkman, A. Water and Glycerol Permeabilities of Aquaporins 1–5 and MIP Determined Quantitatively by Expression of Epitope-Tagged Constructs in *Xenopus* Oocytes. *Journal of Biological Chemistry* **1997**, *272*, 16140–16146, doi:10.1074/jbc.272.26.16140.
117. Galano-Frutos, J.J.; Sancho, J. Energy, Water, and Protein Folding: A Molecular Dynamics-Based Quantitative Inventory of Molecular Interactions and Forces That Make Proteins Stable. *Protein Science* **2024**, *33*, e4905, doi:10.1002/pro.4905.
118. Galano-Frutos, J.J.; Nerín-Fonz, F.; Sancho, J. Calculation of Protein Folding Thermodynamics Using Molecular Dynamics Simulations. *J. Chem. Inf. Model.* **2023**, *63*, 7791–7806, doi:10.1021/acs.jcim.3c01107.
119. Pellegrini-Calace, M.; Maiwald, T.; Thornton, J.M. PoreWalker: A Novel Tool for the Identification and Characterization of Channels in Transmembrane Proteins from Their Three-Dimensional Structure. *PLoS Comput Biol* **2009**, *5*, e1000440, doi:10.1371/journal.pcbi.1000440.
120. Abaie, E.; Xu, L.; Shen, Y. Bioinspired and Biomimetic Membranes for Water Purification and Chemical Separation: A Review. *Front. Environ. Sci. Eng.* **2021**, *15*, 124, doi:10.1007/s11783-021-1412-8.
121. Frick, A.; Järvå, M.; Törnroth-Horsefield, S. Structural Basis for pH Gating of Plant Aquaporins. *FEBS Letters* **2013**, *587*, 989–993, doi:10.1016/j.febslet.2013.02.038.
122. Tournaire-Roux, C.; Sutka, M.; Javot, H.; Gout, E.; Gerbeau, P.; Luu, D.-T.; Bligny, R.; Maurel, C. Cytosolic pH Regulates Root Water Transport during Anoxic Stress through Gating of Aquaporins. *Nature* **2003**, *425*, 393–397, doi:10.1038/nature01853.
123. Yaneff, A.; Sigaut, L.; Marquez, M.; Alleva, K.; Pietrasanta, L.I.; Amodeo, G. Heteromerization of PIP Aquaporins Affects Their Intrinsic Permeability. *Proceedings of the National Academy of Sciences* **2014**, *111*, 231–236, doi:10.1073/pnas.1316537111.
124. Yaneff, A.; Sigaut, L.; Gómez, N.; Aliaga Fandiño, C.; Alleva, K.; Pietrasanta, L.I.; Amodeo, G. Loop B Serine of a Plasma Membrane Aquaporin Type PIP2 but Not PIP1 Plays a Key Role in pH Sensing. *Biochimica et Biophysica Acta (BBA) - Biomembranes* **2016**, *1858*, 2778–2787, doi:10.1016/j.bbamem.2016.08.002.
125. Goldman, R.P.; Jozefkowicz, C.; Canessa Fortuna, A.; Sutka, M.; Alleva, K.; Ozu, M. Tonoplast (BvTIP1;2) and Plasma Membrane (BvPIP2;1) Aquaporins Show Different Mechanosensitive Properties. *FEBS Letters* **2017**, *591*, 1555–1565, doi:10.1002/1873-3468.12671.
126. English, N.J.; Garate, J.-A. Near-Microsecond Human Aquaporin 4 Gating Dynamics in Static and Alternating External Electric Fields: Non-Equilibrium Molecular Dynamics. *The Journal of Chemical Physics* **2016**, *145*, 085102, doi:10.1063/1.4961072.
127. Hub, J.S.; Aponte-Santamaría, C.; Grubmüller, H.; De Groot, B.L. Voltage-Regulated Water Flux through Aquaporin Channels In Silico. *Biophysical Journal* **2010**, *99*, L97–L99, doi:10.1016/j.bpj.2010.11.003.
128. Discovery Studio, BIOVIA, Dassault Systèmes 2022.

129. Cherkasov, A.; Muratov, E.N.; Fourches, D.; Varnek, A.; Baskin, I.I.; Cronin, M.; Dearden, J.; Gramatica, P.; Martin, Y.C.; Todeschini, R.; et al. QSAR Modeling: Where Have You Been? Where Are You Going To? *J. Med. Chem.* **2014**, *57*, 4977–5010, doi:10.1021/jm4004285.
130. Tropsha, A.; Isayev, O.; Varnek, A.; Schneider, G.; Cherkasov, A. Integrating QSAR Modelling and Deep Learning in Drug Discovery: The Emergence of Deep QSAR. *Nat Rev Drug Discov* **2024**, *23*, 141–155, doi:10.1038/s41573-023-00832-0.
131. Muratov, E.N.; Bajorath, J.; Sheridan, R.P.; Tetko, I.V.; Filimonov, D.; Poroikov, V.; Oprea, T.I.; Baskin, I.I.; Varnek, A.; Roitberg, A.; et al. QSAR without Borders. *Chem. Soc. Rev.* **2020**, *49*, 3525–3564, doi:10.1039/D0CS00098A.
132. Javier Sancho, J.J.G. QSAR Models for Prediction of Binding and Inhibitory Properties of [(E)-2- R-Vinyl]Benzene Derivatives with Therapeutic Effects against Helicobacter Pylori. *Med chem* **2013**, *04*, doi:10.4172/2161-0444.1000157.
133. Emonts, J.; Buyel, J.F. An Overview of Descriptors to Capture Protein Properties – Tools and Perspectives in the Context of QSAR Modeling. *Comput Struct Biotechnol J* **2023**, *21*, 3234–3247, doi:10.1016/j.csbj.2023.05.022.
134. Barley, M.H.; Turner, N.J.; Goodacre, R. Improved Descriptors for the Quantitative Structure–Activity Relationship Modeling of Peptides and Proteins. *J. Chem. Inf. Model.* **2018**, *58*, 234–243, doi:10.1021/acs.jcim.7b00488.
135. Mom, R.; Muries, B.; Benoit, P.; Robert-Paganin, J.; Réty, S.; Venisse, J.-S.; Padua, A.; Label, P.; Auguin, D. Voltage-Gating of Aquaporins, a Putative Conserved Safety Mechanism during Ionic Stresses. *FEBS Letters* **2021**, *595*, 41–57, doi:10.1002/1873-3468.13944.
136. Ignacz, G.; Szekely, G. Deep Learning Meets Quantitative Structure–Activity Relationship (QSAR) for Leveraging Structure-Based Prediction of Solute Rejection in Organic Solvent Nanofiltration. *Journal of Membrane Science* **2022**, *646*, 120268, doi:10.1016/j.memsci.2022.120268.
137. Ignacz, G.; Bader, L.; Beke, A.K.; Ghunaim, Y.; Shastry, T.; Vovusha, H.; Carbone, M.R.; Ghanem, B.; Szekely, G. Machine Learning for the Advancement of Membrane Science and Technology: A Critical Review. *Journal of Membrane Science* **2025**, *713*, 123256, doi:10.1016/j.memsci.2024.123256.
138. Yangali-Quintanilla, V.; Verliefe, A.; Kim, T.-U.; Sadmani, A.; Kennedy, M.; Amy, G. Artificial Neural Network Models Based on QSAR for Predicting Rejection of Neutral Organic Compounds by Polyamide Nanofiltration and Reverse Osmosis Membranes. *Journal of Membrane Science* **2009**, *342*, 251–262, doi:10.1016/j.memsci.2009.06.048.
139. Kyte, J.; Doolittle, R.F. A Simple Method for Displaying the Hydrophobic Character of a Protein. *Journal of Molecular Biology* **1982**, *157*, 105–132, doi:10.1016/0022-2836(82)90515-0.
140. Tibshirani, R. Regression Shrinkage and Selection Via the Lasso. *Journal of the Royal Statistical Society: Series B (Methodological)* **1996**, *58*, 267–288, doi:10.1111/j.2517-6161.1996.tb02080.x.
141. Horner, A.; Zocher, F.; Preiner, J.; Ollinger, N.; Siligan, C.; Akimov, S.A.; Pohl, P. The Mobility of Single-File Water Molecules Is Governed by the Number of H-Bonds They May Form with Channel-Lining Residues. *Science Advances* **2015**, *1*, e1400083, doi:10.1126/sciadv.1400083.
142. Gavrilov, Y.; Leuchter, J.D.; Levy, Y. On the Coupling between the Dynamics of Protein and Water. *Phys. Chem. Chem. Phys.* **2017**, *19*, 8243–8257, doi:10.1039/C6CP07669F.

143. Kovalevskiy, O.; Mateos-Garcia, J.; Tunyasuvunakool, K. AlphaFold Two Years on: Validation and Impact. *Proceedings of the National Academy of Sciences* **2024**, *121*, e2315002121, doi:10.1073/pnas.2315002121.
144. Jumper, J.; Evans, R.; Pritzel, A.; Green, T.; Figurnov, M.; Ronneberger, O.; Tunyasuvunakool, K.; Bates, R.; Židek, A.; Potapenko, A.; et al. Highly Accurate Protein Structure Prediction with AlphaFold. *Nature* **2021**, *596*, 583–589, doi:10.1038/s41586-021-03819-2.
145. PROSITE: Database of Protein Domains, Families and Functional Sites Available online: <https://prosite.expasy.org/> (accessed on 16 October 2023).
146. Sigrist, C.J.A.; de Castro, E.; Cerutti, L.; Cuche, B.A.; Hulo, N.; Bridge, A.; Bougueleret, L.; Xenarios, I. New and Continuing Developments at PROSITE. *Nucleic Acids Research* **2013**, *41*, D344–D347, doi:10.1093/nar/gks1067.
147. Paysan-Lafosse, T.; Blum, M.; Chuguransky, S.; Grego, T.; Pinto, B.L.; Salazar, G.A.; Bileschi, M.L.; Bork, P.; Bridge, A.; Colwell, L.; et al. InterPro in 2022. *Nucleic Acids Research* **2023**, *51*, D418–D427, doi:10.1093/nar/gkac993.
148. InterPro: Classification of Protein Families Available online: <https://www.ebi.ac.uk/interpro/> (accessed on 26 April 2024).
149. Berman, H.M.; Mitsuoka, K.; Westbrook, J.; Gilliland, Z.F. and G; Bhat, T.N.; Weissig, H.; Shindyalov, I.N.; Bourne, P.E. The Protein Data Bank. *Nucleic Acids Research* **2000**, *28*, 235–242, doi:10.1093/nar/28.1.235.
150. Zeng, J.; Schmitz, F.; Isaksson, S.; Glas, J.; Arbab, O.; Andersson, M.; Sundell, K.; Eriksson, L.A.; Swaminathan, K.; Törnroth-Horsefield, S.; et al. High-Resolution Structure of a Fish Aquaporin Reveals a Novel Extracellular Fold. *Life Science Alliance* **2022**, *5*, doi:10.26508/lsa.202201491.
151. Kosinska Eriksson, U.; Fischer, G.; Friemann, R.; Enkavi, G.; Tajkhorshid, E.; Neutze, R. Subangstrom Resolution X-Ray Structure Details Aquaporin-Water Interactions. *science* **2013**, *340*, 1346–1349, doi:10.1126/science.1234306.
152. Lee, J.K.; Finer-Moore, J.S.; Stroud, R.M. RCSB Protein Data Bank, 3NE2: Archaeoglobus Fulgidus Aquaporin Available online: <https://www.rcsb.org/structure/3ne2> (accessed on 6 October 2023).
153. Saitoh, Y.; Mitani-Ueno, N.; Saito, K.; Matsuki, K.; Huang, S.; Yang, L.; Yamaji, N.; Ishikita, H.; Shen, J.-R.; Ma, J.F.; et al. Structural Basis for High Selectivity of a Rice Silicon Channel Lsi1. *Nature communications* **2021**, *12*, 6236, doi:10.1038/s41467-021-26535-x.

Supplementary Information

for

Functionality Determinants and Pore-level Quantitative Structure–Activity Relationship (QSAR) Approach for Water Permeation Rate in Aquaporins

Juan José Galano-Frutos ^{1,†,*}, Luca Bergamasco ^{2,†,*}, Paolo Vigo ², Matteo Morciano ², Matteo Fasano ², Davide Pirolli ¹, Eliodoro Chiavazzo ² and Maria Cristina de Rosa ¹

¹*Istituto di Scienze e Tecnologie Chimiche “Giulio Natta” (SCITEC) - National Research Council (CNR), Via Largo Francesco Vito 1, 00168 Rome, Italy*

²*Department of Energy, Politecnico di Torino, C.so Duca degli Abruzzi 24, 10129 Turin, Italy*

[†]*These authors contributed equally to this work*

^{*}*Corresponding author(s): J.J. G.-F. juan-jose.galano-frutos@scitec.cnr.it; L.B. luca.bergamasco@polito.it*

TABLE OF CONTENT

SUPPLEMENTARY MATERIALS AND METHODS.....	4
Pairwise Comparison (Structure and Sequence) of AQPs	4
Pore Descriptors (PDs) and Training Set.....	5
Best Practices and Pore-level QSAR Modeling Implemented.....	7
SUPPLEMENTARY TABLES.....	9
Table S1. Experimental or computed water permeability(s) reported for the collected AQPs, as well as for some AQPs without available 3D structure (therefore, not listed in Tables 1 and 2 of the main article).	9
Table S2. Composition (in %) per amino acid (AA) and per amino acid type for the AQPs' pore lining compared to whole protein.....	15
Table S3. Pore characteristics and additional data extracted from PoreWalker output.....	18
Table S4. Statistical and predictive parameters of the best-performing QSAR models, including those with one and two PDs. ^a	24
Table S5. Experimental versus predicted PR residuals obtained from Models 1 and 2 presented in the main manuscript. ^a	26
Table S6. Resolution, experimental conditions and other relevant information about the crystallization of the AQPs included in the QSAR training set. ^a	27
SUPPLEMENTARY FIGURES.....	28
Figure S1. Structural and sequence comparisons of AQPs.	28
Figure S2. Hierarchical clustering based on the pairwise TM-score of AQPs.....	29
Figure S3. Pore properties profiles and geometrical shape for all the AQPs listed in Tables 1 and 2 of the main manuscript, except for <i>E. coli</i> AqpZ included in the main article.	34
Figure S4. Structure comparison of AQPs on pore gating molecular events.....	35

Figure S5. Scheme showing the structural alignment of the ten AQPs used as the training set in the pore-level QSAR study conducted as a proof of concept.	36
Figure S6. Final LASSO coefficients after applying the LASSO method [10] for feature selection.....	37
Figure S7. Comparative analysis of y -scrambled models versus the unscrambled one.....	38
SUPPLEMENTARY REFERENCES	39

SUPPLEMENTARY MATERIALS AND METHODS

Pairwise Comparison (Structure and Sequence) of AQPs

Systematic structural similarity (Template Modeling, TM-score) and sequence identity (SI) pairwise analyses have been carried out for the AQPs listed in Tables 1 and 2 of the main manuscript. TM-score is a length-independent metric for assessing the topological similarity of two protein structures. It ranges between 0 and 1, where 1 indicates a perfect match between two structures, values below 0.17 correspond to randomly chosen unrelated proteins whereas structures with a score higher than 0.7 assume generally the same fold in SCOP/CATH [1,2]. Such length independency has prompted the recommendation of this metric over the more commonly used RMSD metric for global comparative structural analyses [1].

The pairwise structural comparison between different proteins was carried out using the Pairwise Structure Alignment tool, available at the RCSB PDB website [3]. The selected protein chains are superposed based on the position of the C-alpha atoms of the backbone and on the location of secondary structural elements. Here, we selected the initial chain of the tetrameric AQPs' structures for the calculations. The tool provides several alignment methods, both rigid and flexible. Here we adopt a rigid body alignment, which is suitable for overall structural comparison of proteins which have closely related 3D shapes. Particularly, we adopt the FATCAT algorithm [4,5], which allows for flexible structure comparison but can be modified to a rigid structure comparison considering only alignments with matching sequence order. The method allows to calculate the TM-score [2] and the percentages of sequence identity per protein pair, among other features.

Results of the pairwise analyses carried out are shown in Figure S1 (panels A and C). The pairwise TM-scores depicted on the 2D map (Figure S1, panel A: > 0.75 for all pairs) confirm the high degree of structural similarity among all the AQPs, regardless the live kingdom or the class or sub-class they belong to. TM-score average per aquaporin (computed across all structures, as shown in Figure S1, panel B) were calculated. The averages consistently surpass the value of 0.8, with the exception of *Komagataella pastoris* aquaporin-1 (0.77), that is the only fungal AQP and the most

structurally distinct protein within the analyzed AQPs set. This distinctness is also evident from the pairwise TM-score-based clustering carried out and shown in Figure S2.

Despite the high global structural similarity among all types of AQPs (Figure S1, panel B), the specific structural features exhibited by the AQPs allow them to be grouped by the kingdom of life (e.g., animals, plants, protista, fungi, monera) or by aquaporin type (AQPs or AQPps; see Table 1 of the main article), as shown in Figure S2. Indeed, AQPs pairs showing the highest pairwise TM-score (>0.95) are the *Archaeoglobus fulgidus* probable aquaporin M (aAqpM) and the *Methanothermobacter marburgensis* aquaporin M (mAqpM), with a TM-score of 0.99 (71 % SI, Figure S1, panel C), the *Agrobacterium fabrum* aquaporin Z2 (aAqpZ2) and the *Escherichia coli* aquaporin Z (eAqpZ), with a TM-score of 0.97 (74 % SI), the hAqp1 and the bAqp1, with a TM-score of 0.96 (89 % SI), the bAqp0 and oAqp0, with a TM-score of 0.96 (98 % SI). Consistent with this, the human aquaglyceroporins hAqp7 and hAqp10 are grouped with the other two aquaglyceroporins in the AQPs set, namely pAqgp (*Plasmodium falciparum*) and eGlpF (*E. coli*), despite belonging to different kingdoms of life. All against all, mammalian AQPs shows the highest pairwise TM-score averages (Figure S1, panel B), namely oAqp0 (0.856), hAqp4 (0.854), rAqp4 (0.853), and bAqp0 (0.853).

At the sequence level, the highest pairwise SI averages (calculated over all the AQPs) are exhibited by the orthodox AQPs from animals, namely hAqp1 (0.415), hAqp5 (0.411), oAqp0 (0.41), bAqp0 (0.41), hAqp4 (0.41), rAqp4 (0.41), bAqp1 (0.408), hAqp2 (0.405) and aAqp1 (0.405) (Figure S1, panel D).

Pore Descriptors (PDs) and Training Set

To accomplish the pore-level QSAR modeling, we first proceeded to equalize the length of the x-coordinate of the pores across all the 10 AQPs in our training set, namely: bAqp0, oAqp0, bAqp1, hAqp1, hAqp2, hAqp4, rAqp4, mAqpM, eAqpZ and eGlpF (proteins with measurements of osmotic water permeability reported). We previously aligned the pore x-coordinate to ensure all the AQPs to have the same reference position (the beta carbon of the asparagine in the second NPA motif, where $x=0$, see Table S3, Figure 5 of the main article and Figure S3).

The x -coordinate equalization was performed by setting the minimum and maximum x -coordinates for all AQPs to -20 and 17.5 Å, respectively, trimming the external portions of the pore at both ends (intra- and extracellular, see Figure S5). In addition to equalizing the pore x -coordinate, this trimming was motivated by the observation that pore diameter profiles for several AQPs (obtained by the PoreWalker tool [6]) showed artifactually elongated x -coordinates at either the intracellular or extracellular end, or both (see Figure 5 of the main manuscript and Figure S3). In these regions, the pore shape is less defined, making it difficult to precisely determine which residues line the channel. Trimming the pore ends, therefore, helps to reduce the uncertainty associated with identifying the pore-lining residues at these parts, and also allows for a more reasonable standardization of the pore B-factors. Further pore trimmings resulting in shorter x -coordinate ranges (see Table S4), and, therefore, new sets of PD values, were conducted to analyze the impact of the longitudinal variability of certain PDs on the modeled permeability rate.

Amino acid hydrophobicity, represented here through the descriptors 'Ave_hydropho' (average per-residue hydrophobicity along the pore) and 'Ave_hydrophi' (average per-residue hydrophilicity), is the Kyte-Doolittle hydrophobicity scale [7]. The descriptor 'Ave_hydropho' considers only strictly hydrophobic amino acids (i.e., those with positive Kyte-Doolittle hydrophobicity), whereas 'Ave_hydrophi' accounts for strictly hydrophilic amino acids (i.e., those with negative Kyte-Doolittle hydrophobicity), although the latter was converted into a positive value by multiplying by -1 . The 'regularity' of the pore, provided by PoreWalker [6] as a percentage (see Table S2 and the **Supplementary Files**), was scaled between 0 and 10 (by dividing by 10) to match the scale of the other PDs. The pore regularity is a measure of how much straight (or uniform) is a pore longitudinally [6]. Moreover, since the B-factors were obtained from X-ray structures with different resolutions (the PBD IDs are indicated in Table S1 and in Tables 1 and 2 of the main manuscript), making their scales not directly comparable, we normalized them also between 0 and 10 for each AQP. Taking into account the differences —sometimes significant— between the B-factors of amino acid side chains (usually more flexible) and those of their backbone, we included the B-factor averages of these elements as pore

descriptors ('Ave_Bfac_SC' and 'Ave_Bfac_BB', normalized in the same way as the global B-factor, 'Ave_Bfac') in the modeling, with the aim of assessing their specific importance. The entire PD dataset was standardized prior to modeling to further prevent scale-related issues. PD values (prior to standardization) of the AQPs in the training set (for each pore trimmings evaluated) are compiled in CSV files and provided as **Supplementary Files**. Given the small number of PR data points available among AQPs, the entire dataset was used as a training set.

Best Practices and Pore-level QSAR Modeling Implemented

Autocorrelation analysis enabled the identification of multicollinearity between descriptors through the evaluation of the auto-correlation matrix, variance inflation factors (VIF)¹, and the condition number (CN)² for each QSAR model (Table S4). Note that the CN value in single-variable regression models does not, of course, measure multicollinearity between variables (which would not make sense); instead, it provides an assessment of the adequacy of the data scale and/or the numerical stability of the model.

The alpha³ parameter (lambda in Ref. [10]), used to penalize highly correlated independent variables, was set in the range of 0.1 to 1 (moderate penalty) and the

¹ The Variance Inflation Factor (VIF) [8] measures the extent of multi-collinearity in a regression model. A VIF value of 1 indicates no correlation between the independent variable and others. Values between 1 and 5 suggest moderate multicollinearity, while values above 5 indicate significant multicollinearity that could affect the stability of coefficient estimates. A VIF greater than 10 is often considered problematic, as it implies substantial inflation of the variance of the estimated coefficients, leading to unreliable results.

² The condition number (CN) [9] is a crucial metric that assesses the sensitivity of the regression coefficients to perturbations in the data. Generally, a condition number less than 10 indicates a well-conditioned model, suggesting stable and reliable coefficient estimates with minimal numerical errors. Values between 10 and 30 are often associated with moderate multicollinearity, where the results may still be usable but should be approached with caution. Condition numbers between 30 and 100 indicate significant multi-collinearity, raising concerns about the stability of the coefficient estimates. A condition number greater than 100 signals a poorly conditioned model, which can lead to high sensitivity to input changes, resulting in considerable numerical instability and unreliable outputs.

³ The alpha parameter in the LASSO method controls the strength of the regularization applied to the regression model. A small alpha value (e.g., <0.1) results in minimal regularization, allowing for more complex models that may overfit the data. Conversely, a larger alpha value (e.g., >1.0) increases the penalty on the coefficients, particularly affecting variables with

maximum number of iterations to 1,000,000 when applying the LASSO iterative regularization [10] to the regression models (OLS-MLR) to select the best combination of PDs. Convergence was attained in all cases. Statistical parameters obtained to assess the performance of the QSAR models include: R-squared (internal coefficient of determination), regression p-value (from a Fisher F-test), statistical significance (from a Student t-test, $\alpha=0.05$) for each independent variable (PD) in the models and the independent term, as well as the predictive parameters: SPRESS: Standard Prediction Error Sum of Squares, and LOO-Q² (leave-one-out cross-validation coefficient)⁴, all of which are presented in Table S4. One hundred (100) *y*-scrambled models were evaluated, and random fitting was discarded when none of the new shuffled models exhibited both R² and LOO-Q²⁵ that equaled or exceeded those of the original model. An *ad-hoc* Python script was prepared to perform all regression, statistical and *y*-scrambling analyses, which is provided as a **Supplementary File** (<https://shorturl.at/S1yTJ>).

significant multicollinearity. This leads to simpler models with potentially better generalization, but at the cost of possibly excluding important predictors and risking underfitting the data.

⁴ In QSAR studies, LOO-Q² values above 0.5 are typically regarded as acceptable, indicating satisfactory predictive ability. Values between 0.5 and 0.9 suggest good to very good predictivity, while values above 0.9 imply excellent predictivity.

SUPPLEMENTARY TABLES

Table S1. Experimental or computed water permeability(s) reported for the collected AQPs, as well as for some AQPs without available 3D structure (therefore, not listed in Tables 1 and 2 of the main article).

Protein (PDB) ^a	Experimental Osmotic Permeability, p^b ($\times 10^{-14} \text{ cm}^3 \cdot \text{s}^{-1}$)	Reference	Comments ^c	Computed Osmotic Permeability, p^b ($\times 10^{-14} \text{ cm}^3 \cdot \text{s}^{-1}$)	Reference	Comments ^c
bAqp0 (1YMG)	<0.4	[11]	PSA: proteoliposomes prepared by reverse-phase evaporation, by adding phosphatidylcholine (PC, 400 mg), phosphatidylinositol (PI, 40 mg), and cholesterol (240 mg), (moles of PC:PI:cholesterol = 11:1:11); Buffer: EDTA-phosphate (pH 7.4); Yield of bAqp0 in proteoliposomes: 33%.	0.2±0.2	[12]	Measurements from equilibrium MDS of the protein in a lipid bilayer (5 ns x 2 replicas, NPT); Starting structure PDB: 1YMG; FFs: Charmm22+CMAP (protein), Charmm27 (lipids); WM: Tip3p.
	0.028	[13]	OSA: measurements performed in <i>Xenopus laevis</i> oocytes injected with cRNAs coding for the protein; Buffer: 96 mM NaCl, 2 mM KCl, 1 mM MgCl ₂ , 1.8 mM CaCl ₂ , 5 mM HEPES (pH 7.6).			
	0.015	[14]	OSA: measurements performed in <i>Xenopus laevis</i> oocytes injected with cRNAs coding for the protein; Buffer: 96 mM NaCl, 2 mM KCl, 1.8 mM CaCl ₂ , 1 mM MgCl ₂ and 5 mM HEPES (pH 7.4) plus supplements (2.5 mM sodium pyruvate, 10 µg/ml aminobenzylpenicillin, 10 µg/ml streptomycin); Measured at 10°C.			
Ave±SEM*: <0.15±0.13						
oAqp0 (2B6O)	0.2±0.05	[15]	PSA: proteoliposomes reconstituted by dialysis by mixing purified oAqp1 (0.5 mg/mL) with the lipids PC, PS (phosphoserine) with cholesterol (1:4:5)	0.2±0.2	[15]	Measurements from equilibrium MDS of the protein in a POPC lipid bilayer (500 ns, NPT, 305 K, 1 atm); Starting structure PDB: 2B6O; FFs: Charmm36 (protein & lipids); WM: --;

			solubilized in OG at a lipid-protein ratio of 2 mg/mg; Buffer: 20 mM HEPES, 100 mM NaCl (pH 7.5). Measurements performed under a pressure gradient created by osmotic agents. Measured at 15°C.			150 mM NaCl; Essential-dynamics (ED) simulations were also carried out to restrain the protein in the open and closed states.
rAqp0 (no PDB structure)	0.3±0.1	[16]	OSA: measurements performed in <i>Xenopus laevis</i> oocytes injected with cRNAs coding for the protein; Buffer: Barth's solution (pH 7.4); Measured at 10°C.			
bAqp1 (1J4N)	2.3	[17]	PSA: proteoliposomes prepared by reverse-phase evaporation mixing purified bAqp1 and the lipids PC, PI with cholesterol (11:1:11); Buffer: 1 mM EDTA, 100 mM Na-phosphate (pH 7.4) and 200 mM octyl glucoside (OG). Measurements performed under osmotic gradient created by different solute concentrations of the Buffer (from 10 to 60-100 mM Na-phosphate).	10.1±4.0	[12]	Same MDS setup as for bAqp0; Starting structure PDB: 1J4N.
				7.1±0.9	[18]	MDS of the protein in a lipid bilayer (5 ns x 4 replicas, NVT, 310 K); A water pressure gradient is settled by applying a constant force on all water molecules in the main direction of the channel; Starting structure PDB: 1J4N; FFs: Charmm22+CMAP (protein), Charmm27 (lipids); WM: Tip3p.
Ave±SEM: 8.8±1.7						
hAqp1 (7UZE)	6.0±1.0	[11]	Same as for bAqp0. Yield of bAqp0 in proteoliposomes: 50%.	7.5±0.5	[19]	Measurements from equilibrium MDS of the protein in a lipid bilayer (10 ns, 2fs time-step, NPT, 300 K); Starting structure PDB: 1H6I; FFs: Gromos (protein & lipids).
	1.2	[13]	Same as for bAqp0.			
	1.4	[14]	Same as for bAqp0.			
	3.4	[17]	Same as for bAqp1.			
	6.8	[20]	PSA: measurements performed under osmotic gradient produced by manitol solutions; Buffer: Tris/HCl (pH 7.4); Measured at 10°C.			

	11.7±1.8	[21]	PSA: measurements performed under osmotic gradient with sucrose solutions on proteoliposomes prepared by mixing purified hAqp1, <i>E. coli</i> phospholipid, OG, and Tris-HCl; Buffer: MOPS (pH 7.5); Yield of hAqp1 in proteoliposomes: 50%.		
	5.43	[22]	Same as done by Zeidel, et al. [21]		
	4.6	[23]	Same as done by Zeidel, et al. [21], except that the concentration of hAqp1 in the proteoliposomes was varied in a range of values to determine the unit water conductance more precisely.		
Ave±SEM: 5.1±1.2					
rAqp1 (no PDB structure)	6.0	[16]	Same as for rAqp0.		
rabAqp1 (no PDB structure)	2.6	[17]	Same as for bAqp1.		
pAqp1 (no PDB structure)	1.9	[17]	Same as for bAqp1.		
oAqp1 (no PDB structure)	2.0	[17]	Same as for bAqp1.		
hAqp2 (4NEF)	9.3±0.3	[24]	PSA: measurements performed under osmotic gradient with sucrose solutions on proteoliposomes prepared by mixing purified hAqp2 and <i>E. coli</i> lipids; Buffer: 20 mM Tris-HCl, 50 mM NaCl (pH 7.2).	5.3±2.2	[25] MDS of the protein in a lipid bilayer (20 ns x 1 replica, NVT, 310 K); Starting structure PDB: 4NEF; FFs: Charmm22+CMAP (protein), Charmm27 (lipids); WM: Tip3p.
rAqp2	3.3±0.2	[16]	Same as for rAqp0.		

(no PDB structure)						
hAqp4 (3GD8)	11.0±1.0	[26]	PSA: measurements performed under osmotic gradient with sucrose solutions on proteoliposomes prepared by mixing purified hAqp4 and a mixture of POPC, POPG and cholesterol (2:1:2); Buffer: 20 mM HEPES, 200 mM NaCl (pH 8.0); Measured at 18°C.	1.3±0.3 to 9.5±2.1	[27]	Same approach followed by Hashido et al. [12] (200 ns x 1 replica, NPT, 310 K); Starting structure PDB: 3GD8.
				2.9±0.5	[28]	Equilibrium MDS of the protein in a lipid bilayer (100 ns x 1 replica, NPT, 298 K); Starting structure PDB: 3GD8; FFs: Charmm22+CMAP (protein), Charmm27 (lipids); WM: Tip3p.
				Ave±SEM: 4.2±1.3		
rAqp4 (2D57)	24.0±0.6	[16]	Same as for rAqp0.	7.4±2.6	[29]	Same MD setup as for bAqp0 by Hashido et al. [12]; Starting structure PDB: 2D57; Introduction of a p_f -matrix method for analysis, where p_f is decomposed into contributions from each channel local region.
	9.0 to 35.0	[30]	PSA: measurements performed under osmotic gradient with sucrose solutions on proteoliposomes prepared by mixing purified rAqp4, octyl glucoside and four different mixtures of two phospholipids: 1) dierucoylphosphatidylcholine & dielaidoylphosphatidylglycerol, 2) dieicosenoylphosphatidylcholine & dielaidoylphosphatidylglycerol, 3) palmitoylloeylphosphatidylcholine & dielaidoylphosphatidylglycerol, 4) ditridecanoylphosphatidylcholine & dimyristoylphosphatidylglycerol; Buffer: 25 mM HEPES, 50 mM NaCl, pH 7.4; Measured at 20°C.	25.0±1.0 (1) 33.0±1.0 (2)	[30]	MDS of the protein in two lipid bilayer of different thickness: (1) dimyristoylphosphatidylcholine, (2) dierucoylphosphatidylcholine (20 replicas each, 40ns total, NVT, 300 K); r-RESPA multiple-time-step integrator applied with time steps of 2 and 4 fs for short-range non-bonded and long-range electrostatic interactions, respectively; Water pressure gradient settled by applying an ion gradient (50 mM NaCl on the cytoplasmic side and 150 mM on the extracellular side); Starting structure PDB: 2D57; FFs: Charmm36 (protein & lipids); WM: modified Tip3p; 200 mM NaCl.
				Ave±SEM: 23.0±1.0		Ave±SEM: 21.8±7.6

hAqp5 (3D9S)				5.1	[31]	Same approach followed by Hashido et al. [12] (500 ns x 1 replica, NPT, 300 K); Starting structure PDB: 3D9S.
rAqp5 (no PDB structure)	5.0±0.4	[16]	Same as for rAqp0.			
hAqp7 (6QZI)				4.8±0.2	[32]	MDS of the protein in a lipid bilayer (500-1000 ns x 5 replicas, NPT, 300 K); Starting structure PDB: 6QZI; FF: Charmm36m for protein and lipids; WM: Tip3p.
mAqpM (2F2B)	0.6	[33]	PSA: measurements performed under osmotic gradient with sucrose solutions on proteoliposomes prepared by mixing purified mAqpM, octyl glucoside and <i>E. coli</i> phospholipids; Buffer: MOPS (pH 7.5); Measured at 4°C.	6.4±1.4	[34]	MDS of the protein in a lipid bilayer (20ns x 1 replica, NPT, 300 K); Starting structure PDB: 6QZI; FF: Charmm36m for protein and lipids; WM: Tip3p.
	0.7	[35]	PSA: measurements performed by setting an osmotic gradient with sucrose solutions on proteoliposomes; Buffer: 1.2% octyl glucoside, 50 mM HEPES, 100mM NaCl (pH 7.4); Measured at 12°C.			
Ave±SEM: 0.7±0.1						
eAqpZ (1RC2)	>=10.0	[36]	PSA: measurements performed under osmotic gradient with sucrose solutions on proteoliposomes prepared by mixing purified AqpZ, octyl glucoside and lipids; Buffer: MOPS (pH 7.5).	3.2±0.7 to 4.4±0.7	[37]	MDS of the protein in several lipid bilayer compositions (18.5-26.5ns x 1 replica, NPT, 310 K); Starting structure PDB: 1RC2; FFs: Charmm22+CMAP (protein), Charmm27 (lipids); WM: Tip3p.
	2.0	[38]	PMA: measurements performed after forming planar lipid bilayers from unilamellar vesicles (proteoliposomes) containing purified AqpZ. Transmembrane water flux measured from solute concentration changes in the immediate membrane vicinity; 50 mM MOPS, 100 mM NaCl, 0.3, μM CaCl ₂ (pH 7.5).	15.9±5.1	[12]	Same as for bAqp0; Starting structure PDB: 1RC2.

Ave±SEM: >6.0±4.0			Ave±SEM: 8.2±3.9			
eGlpF (1FX8)	2.0	[39]	PSA: measurements performed under osmotic gradient with sucrose solutions on proteoliposomes prepared by mixing purified GlpF, octyl glucoside and lipids; Buffer: MOPS (pH 7.5).	14.0±0.4	[40]	MDS of the protein in a lipid bilayer (4 replicas, 5ns total, NPT, 310 K); Water pressure gradient settled by applying a constant force on all water molecules in the main direction of the channel; Starting structure PDB: 1FX8; FFs: Charmm22+CMAP (protein), Charmm27 (lipids); WM: Tip3p.
	0.7	[41]	Same as for AqpZ by Pohl et al. [38]	16.0±3.0	[12]	Same as for bAqp0; Starting structure PDB: 1LDI.
				8.6±1.1 to 13.1±3.4	[37]	MDS of the protein in several lipid bilayer compositions (20-26ns x 1 replica, NPT, 310 K); Starting structure PDB: 1FX8; FFs: Charmm22+CMAP (protein), Charmm27 (lipids); WM: Tip3p.
Ave±SEM: 1.4±0.7			Ave±SEM: 13.6±1.5			

^a rAqpx: rat aquaporins; rabAqp1: rabbit aquaporin-1; pAqp1: pig aquaporin-1; oAqp1: sheep aquaporin-1. ^b Experimental and computed (via MDS) permeabilities reported here refer to per-unit (pore channel) permeability. ^c Abbreviations: SEM, standard error of the mean; OSA, oocytes swelling assay; PSA, proteoliposome swelling assay; PMA, planar membrane assay; MDS, molecular dynamics simulations; FF, force field; WM, water model; NPT, isothermal-isobaric ensemble; NVT, canonical ensemble.

Table S2. Composition (in %) per amino acid (AA) and per amino acid type for the AQPs' pore lining compared to whole protein.

Protein (PDB) ^a	Composition on... ^b	Non-polar AAs									Polar AAs w/o charges						Polar AAs with (-) charges			Polar AAs with (+) charge					
		Gly	Ala	Val	Ile	Leu	Met	Pro	Phe	Trp	Total	Ser	Thr	Cys	Tyr	Asn	Gln	Total	Asp	Glu	Total	Arg	Lys	His	Total
bAqp0 (1YMG)	Whole protein	9.9	12.2	9.5	3.4	14.4	1.9	4.9	6.8	1.9	65.0	7.2	4.9	1.1	3.0	3.0	3.0	22.4	0.8	3.4	4.2	4.9	1.1	2.3	8.4
	Pore lining	11.1	11.1	8.9	4.4	12.2	3.3	3.3	5.6	1.1	61.1	7.8	4.4	0.0	4.4	5.6	1.1	23.3	1.1	2.2	3.3	4.4	2.2	5.6	12.2
oAqp0 (2B6O)	Whole protein	9.9	12.2	9.9	3.4	14.4	1.5	4.9	7.2	1.9	65.4	6.5	5.7	0.8	3.0	3.0	3.0	22.1	0.8	3.4	4.2	4.9	1.1	2.3	8.4
	Pore lining	8.8	9.9	9.9	3.3	12.1	3.3	3.3	5.5	0.0	56.0	5.5	4.4	1.1	5.5	6.6	3.3	26.4	0.0	2.2	2.2	9.9	0.0	5.5	15.4
bAqp1 (1J4N)	Whole protein	9.6	10.3	7.7	9.6	12.2	1.5	3.3	4.8	1.5	60.5	8.9	4.8	1.5	1.8	3.3	3.3	23.6	4.8	2.2	7.0	3.7	3.0	2.2	8.9
	Pore lining	13.3	10.0	7.8	10.0	11.1	1.1	3.3	4.4	0.0	61.1	5.6	5.6	2.2	1.1	6.7	5.6	26.7	2.2	0.0	2.2	5.6	0.0	4.4	10.0
hAqp1 (7UZE)	Whole protein	10.0	10.4	8.2	8.6	12.3	1.1	2.6	4.8	1.5	59.5	8.6	5.6	1.5	1.9	4.1	3.0	24.5	4.8	2.2	7.1	4.1	3.0	1.9	8.9
	Pore lining	12.4	9.0	7.9	6.7	10.1	0.0	1.1	4.5	0.0	51.7	5.6	6.7	2.2	2.2	4.5	4.5	25.8	3.4	1.1	4.5	11.2	3.4	3.4	18.0
aAqp1 (7W7S)	Whole protein	10.3	11.1	9.2	5.7	12.3	2.7	4.2	4.2	1.1	60.9	7.3	5.4	1.9	2.3	5.7	2.3	24.9	3.4	2.7	6.1	2.7	3.8	1.5	8.0
	Pore lining	8.6	9.7	7.5	7.5	9.7	2.2	3.2	4.3	0.0	52.7	11.8	3.2	3.2	2.2	8.6	4.3	33.3	1.1	2.2	3.2	3.2	4.3	3.2	10.8
kAqp1 (3ZOJ)	Whole protein	10.4	15.8	5.0	7.9	8.2	3.2	6.1	7.2	2.9	66.7	4.7	5.0	0.7	3.6	4.3	3.2	21.5	2.5	2.9	5.4	3.6	1.4	1.4	6.5
	Pore lining	12.9	17.2	6.5	6.5	8.6	0.0	3.2	6.5	3.2	64.5	2.2	5.4	1.1	4.3	7.5	4.3	24.7	1.1	3.2	4.3	3.2	2.2	1.1	6.5
hAqp2 (4NEF)	Whole protein	8.9	12.9	8.9	4.4	14.8	1.1	5.2	5.2	1.8	63.1	7.0	5.2	1.5	1.5	2.6	3.0	20.7	2.6	4.4	7.0	4.8	1.5	3.0	9.2
	Pore lining	9.1	14.1	8.1	7.1	7.1	1.0	3.0	6.1	1.0	56.6	9.1	4.0	3.0	1.0	5.1	2.0	24.2	3.0	3.0	6.1	6.1	2.0	5.1	13.1
hAqp4 (3GD8)	Whole protein	10.5	8.7	10.2	8.0	8.0	3.1	3.7	5.3	2.2	59.8	6.5	5.9	2.5	2.2	2.8	2.5	22.3	3.4	4.3	7.7	3.4	4.6	2.2	10.2
	Pore lining	11.4	6.8	11.4	10.2	3.4	8.0	3.4	4.5	0.0	59.1	9.1	5.7	2.3	1.1	6.8	2.3	27.3	2.3	1.1	3.4	2.3	4.5	3.4	10.2
rAqp4 (2D57)	Whole protein	10.5	9.3	10.5	8.0	8.0	2.8	3.7	4.6	2.2	59.8	7.7	5.6	2.5	2.2	2.8	2.2	22.9	3.4	4.3	7.7	3.1	4.3	2.2	9.6
	Pore lining	12.2	6.7	11.1	10.0	3.3	6.7	0.0	5.6	1.1	56.7	12.2	5.6	2.2	1.1	4.4	1.1	26.7	3.3	3.3	6.7	2.2	3.3	4.4	10.0

hAqp5 (3D9S)	Whole protein	8.7	12.8	8.3	6.4	13.6	1.9	4.9	6.4	1.5	64.5	6.4	5.7	1.1	2.3	4.2	3.0	22.6	1.1	4.2	5.3	3.8	2.6	1.1	7.5
	Pore lining	8.5	9.6	6.4	10.6	9.6	1.1	4.3	8.5	0.0	58.5	7.4	5.3	2.1	3.2	7.4	3.2	28.7	1.1	1.1	2.1	6.4	2.1	2.1	10.6
hAqp7 (6QZI)	Whole protein	10.2	8.5	9.4	6.1	10.2	4.4	6.1	5.6	2.3	62.9	7.0	5.6	0.6	3.2	3.5	2.3	22.2	1.5	3.8	5.3	3.8	2.6	3.2	9.6
	Pore lining	9.7	8.6	12.9	8.6	7.5	5.4	5.4	6.5	1.1	65.6	4.3	5.4	1.1	5.4	4.3	1.1	21.5	2.2	3.2	5.4	4.3	1.1	2.2	7.5
hAqp10 (6F7H)	Whole protein	10.6	12.0	9.3	4.0	14.6	3.0	6.3	4.0	1.7	65.4	4.7	6.0	1.7	3.0	3.7	3.7	22.6	1.7	3.7	5.3	2.7	2.0	2.0	6.6
	Pore lining	11.1	13.1	11.1	7.1	11.1	4.0	7.1	4.0	1.0	69.7	4.0	5.1	1.0	4.0	3.0	3.0	20.2	2.0	3.0	5.1	3.0	0.0	2.0	5.1
soPIP2;1 (1Z98)	Whole protein	10.7	13.5	9.3	7.5	8.5	1.8	5.0	7.1	2.1	65.5	5.3	5.0	1.4	3.2	3.2	2.1	20.3	2.5	2.5	5.0	2.8	3.9	2.5	9.3
	Pore lining	12.0	11.0	10.0	11.0	6.0	0.0	4.0	8.0	0.0	62.0	5.0	7.0	1.0	4.0	5.0	2.0	24.0	1.0	1.0	2.0	4.0	3.0	5.0	12.0
mAqpM (2F2B)	Whole protein	14.6	12.6	6.5	12.2	9.8	2.4	4.9	6.5	1.6	71.1	5.3	6.5	1.2	3.7	3.7	1.6	22.0	1.2	2.0	3.3	1.6	1.6	0.4	3.7
	Pore lining	16.2	12.1	6.1	15.2	8.1	2.0	4.0	3.0	1.0	67.7	4.0	9.1	1.0	3.0	3.0	1.0	21.2	2.0	2.0	4.0	3.0	3.0	1.0	7.1
aAqpM (3NE2)	Whole protein	15.0	14.6	7.7	11.0	10.2	2.8	5.7	6.1	1.6	74.8	2.8	6.1	0.4	3.3	3.3	1.2	17.1	1.6	2.4	4.1	2.4	1.2	0.4	4.1
	Pore lining	13.3	13.3	7.6	13.3	8.6	2.9	7.6	3.8	1.0	71.4	2.9	8.6	0.0	1.9	4.8	1.0	19.0	1.9	2.9	4.8	3.8	0.0	1.0	4.8
osNIP2;1 (7CJS)	Whole protein	8.4	10.7	9.7	6.7	7.4	3.7	4.4	6.0	1.7	58.7	8.7	7.4	1.0	2.3	3.7	3.0	26.2	3.4	3.0	6.4	3.4	2.7	2.7	8.7
	Pore lining	15.7	14.3	11.4	5.7	4.3	7.1	2.9	2.9	0.0	64.3	5.7	8.6	1.4	1.4	2.9	2.9	22.9	2.9	1.4	4.3	4.3	0.0	4.3	8.6
atTIP2;1 (5I32)	Whole protein	14.4	16.4	10.0	7.2	10.0	1.6	4.0	6.8	1.2	71.6	7.6	5.2	0.8	3.2	2.0	0.8	19.6	2.8	1.6	4.4	0.8	1.6	2.0	4.4
	Pore lining	8.3	16.7	9.7	6.9	8.3	2.8	4.2	1.4	0.0	58.3	11.1	8.3	0.0	4.2	4.2	1.4	29.2	2.8	1.4	4.2	2.8	1.4	4.2	8.3
atPIP2;4 (6QIM)	Whole protein	11.7	13.7	8.6	7.2	7.6	1.7	5.2	7.2	1.7	64.6	4.5	5.2	1.7	4.5	2.7	1.7	20.3	4.1	2.4	6.5	3.8	3.4	1.4	8.6
	Pore lining	10.5	11.6	11.6	9.5	7.4	1.1	5.3	5.3	0.0	62.1	2.1	8.4	2.1	4.2	5.3	3.2	25.3	2.1	1.1	3.2	4.2	3.2	2.1	9.5
eAqpZ (1RC2)	Whole protein	15.2	14.7	9.5	7.4	11.3	1.3	3.9	7.8	2.2	73.2	5.2	4.8	0.9	2.2	1.7	1.3	16.0	1.3	3.0	4.3	2.2	2.2	2.2	6.5
	Pore lining	14.1	10.9	8.7	5.4	7.6	1.1	4.3	12.0	2.2	66.3	7.6	3.3	1.1	1.1	4.3	0.0	17.4	1.1	3.3	4.3	2.2	4.3	5.4	12.0
aAqpZ2 (3LLQ)	Whole protein	15.4	15.4	9.2	7.9	11.8	0.9	4.4	7.5	2.2	74.6	5.7	5.3	0.4	2.2	1.8	1.8	17.1	0.9	2.2	3.1	1.8	1.8	1.8	5.3
	Pore lining	13.6	12.5	10.2	8.0	8.0	0.0	3.4	11.4	1.1	68.2	4.5	4.5	1.1	1.1	4.5	1.1	17.0	1.1	2.3	3.4	3.4	3.4	4.5	11.4

pAqgp (3C02)	Whole protein	10.5	5.4	8.5	7.4	14.0	1.2	2.7	9.7	1.6	60.9	7.4	5.0	2.3	3.5	4.7	1.2	24.0	3.9	2.7	6.6	1.6	5.0	1.9	8.5
	Pore lining	8.6	7.5	8.6	8.6	12.9	1.1	3.2	5.4	3.2	59.1	6.5	5.4	1.1	2.2	4.3	1.1	20.4	4.3	3.2	7.5	3.2	6.5	3.2	12.9
eGlpF (1FX8)	Whole protein	11.4	12.1	9.3	7.5	10.7	2.1	5.3	7.5	1.8	67.6	4.3	5.3	2.1	2.5	2.5	2.5	19.2	2.8	3.2	6.0	2.5	2.8	1.8	7.1
	Pore lining	13.1	11.1	7.1	9.1	10.1	2.0	6.1	7.1	2.0	67.7	2.0	6.1	2.0	3.0	3.0	2.0	18.2	5.1	0.0	5.1	5.1	2.0	2.0	9.1
ALL PROTEINS	Whole protein	11.2	12.1	8.8	7.2	11.0	2.2	4.6	6.3	1.8	65.3±1.1	6.3	5.5	1.4	2.8	3.3	2.4	21.6±0.6	2.6	3.0	5.6±0.3	3.1	2.6	1.9	7.6±0.4
	Pore lining	11.6	11.2	9.1	8.4	8.5	2.6	3.9	5.8	0.9	61.8±1.2	6.2	5.9	1.5	2.8	5.1	2.3	23.8±0.9	2.1	2.0	4.2±0.3	4.5	2.4	3.4	10.2±0.7

^a Aquaporins full names and their source organisms are given in Table 2 of the main manuscript. ^b Statistics for the whole protein composition obtained from the canonical aquaporin sequences retrieved from UniProtKB database [42], and statistics for the pore lining composition calculated based on the information given by the PoreWalker software [6]. FASTA files with the protein sequence from UniProtKB are provided as **Supplementary Files** along with all the output files issued by PoreWalker including the pore-lining amino acidic composition.

Table S3. Pore characteristics and additional data extracted from PoreWalker output.

AQP short name ^a (PDB ID)	Min pore diameter ^b (Å)	Pore regularity ^c (%)	<i>x</i> -coord at min pore diameter ^d	Residues at min pore diameter ^e	Min pore diameter at SF ^f (Å)	<i>x</i> -coord at SF ^g	Min pore diameter at NPA ^h (Å)	<i>x</i> -coord at NPA ⁱ
bAqp0 (1YMG)	1: 1.7	80.5	1: -13.76	1: I13, G60, I62, S63, G64, F75, F146, Y149, L157	1.7	F48: 3.46 H172: 6.11 A181: 6.62	2.7	N68: -4.62 P69: -4.53 A70: -4.63
	2: 1.7		2: 4.24	2: V24, F48*, H172*, G182, R187*, A190, Y204		R187: 2.46		2.5
oAqp0 (2B6O)	1.4	75.0	3.22	V24, G27, F48*, E134, G182, M183, R187*, Y204	1.4	F48: 3.23 H172: 5.64 A181: 6.48	3.1	N68: -4.71 P69: - A70: -
						R187: 2.54		3.6
bAqp1 (1J4N)	2.5	69.0	2.13	I25, I27, F58*, G59, A107, G181, I193, R197*	2.5	F58: 3.26 H182: 5.75 C191: 6.72 R197: 2.36	3.7	N78: -4.36 P79: - A80: -4.05
							2.9	N194: 0.00 P195: - A196: -
hAqp1 (7UZE)	3.2	67.6	-12.44	G68, G72, L83, L154, T156, A168, V224, Y227	3.9	F56: 3.24 H180: 4.99 C189: 6.16	3.8	N76: -4.78 P77: - A78: -4.66
						R195: 2.55		3.9

								P193: - A194: -
aAqp1 (7W7S)	2.7	85.0	0.15	F23, A53, S99, V168, C169, L170, G171, I183, N184**, P185**	3.9	F50: 2.86 H172: 5.12 C181: - R187: 2.28	3.5 2.7	N70: -4.58 P71: - A72: -3.86 N184: 0.00 P185: 0.07 A186: -
kAqp1 (3ZOJ)	1: 1.9 2: 2.1	66.0	1: -17.25 2: 3.75	Y27, P29, Y31, A124, I125, R129, V191, E192, Q261 L59, A62, F92*, H212*, I214, G222, R227*	2.1	F92: 3.74 H212: 5.45 A221: 6.62 R227: 2.93	3.7 2.7	N112: -4.40 P113: - A114: - N224: 0.00 P225: - A226: -
hAqp2 (4NEF)	2.2	70.3	5.95	G27, A45, A47, A101, C181*, S188	2.2	F48: 3.72 H172: - C181: 6.76 R187: 2.63	4.3 3.0	N68: -4.60 P69: - A70: - N184: 0.00 P185: - A186: -
hAqp4 (3GD8)	2.7	64.9	3.69	V49, S52, F77*, G129, S211, R216*	2.7	F77: 4.03 H201: - A210: 6.57 R216: 2.47	3.5 5.2	N97: -4.60 P98: - A99: - N213: 0.00 P214: - A215: -

rAqp4 (2D57)	2.3	57.9	4.83	V49, S52, F77*, G200, H201*, S211	2.3	F77: 4.22 H201: 6.61 A210: 6.97 R216: 2.72	5.0 3.8	N97: -4.54 P98: - A99: - N213: 0.00 P214: - A215: -1.48
hAqp5 (3D9S)	1.7	33.3	4.55	V25, F27, A48, F49*, H173*, S183, R188*	1.7	F49: 3.76 H173: 5.56 C182: 6.60 R188: 2.94	5.0 3.8	N69: -4.47 P70: - A71: - N185: 0.00 P186: - A187: -0.91
hAqp7 (6QZI)	3.2	41.0	3.46	M48, F74*, V211, Y223*, A224, R229*, D330	3.2	F74: 3.97 G214: - Y223: 4.88 R229: 2.61	4.8 5.6	N94: -4.35 A95: - A96: - N226: 0.00 P227: - S228: -
hAqp10 (6F7H)	1: 1.9 2: 4.6	51.2	1: -14.15 ^Δ 2: 3.85	1: Q23, N75, G78, M89, L95, A176, I177, L178, G184, V185, P186, G188, Y260 2: M35, L37, T38, G62*, S63, A65, A111, A114, G202*, I211*, P212, R217*, D218	4.6	G62: 4.88 G202: 5.46 I211: 4.54 R217: 2.63	4.9 4.8	N82: -4.44 P83: - A84: - N214: 0.00 P215: - A216: -
soPIP2;1 (1Z98)	2.2	39.5	4.41	L52, I54, T55, F81*, G133, H210*, T219*, G220, R225, G228	2.2	F81: 4.27 H210: 5.57 T219: 5.79	3.6	N101: -4.31 P102: - A103: -

						R225: 2.78	2.6	N222: 0.00 P223: - A224: -
mAqpM (2F2B)	2.6	39.5	1.28	L18, F62*, A65, A111, V183, I186, L198, N199**, R202*	2.6	F62: 2.97 I187: 5.38 S196: 5.95 R202: 2.43	4.8 3.5	N82: -4.52 P83: -4.16 A84: - N199: 0.00 P200: - A201: -
aAqpM (3NE2)	2.0	64.3	1.02	F63*, A66, L199, N200**, R203*, P229	2.0	F63: 2.16 I188: 4.63 S197: 5.57 R203: 2.33	4.5 3.4	N83: -4.53 P84: -3.99 A85: - N200: 0.00 P201: - A202: -
osNIP2;1 (7CJS)	4.0	40.5	2.86	V62, T65, I86, G88*, C204, T216, S217, R222*	4.0	G88: 2.79 S207: 5.49 G216: 6.42 R222: 2.09	4.6 5.2	N108: -4.50 P109: - A110: - N219: 0.00 P220: - A221: -
atTIP2;1 (5I32)	2.6	56.4	-4.58	A70, V82, N83**, A85**, Q108, L153, I180	3.6	H63: 4.20 I185: 6.47 G194: 6.41 R200: 2.59	2.6 3.9	N83: -4.46 P84: - A85: -4.29 N197: 0.00 P198: - A199: -

atPIP2;4 (6QIM)	1: 2.1	57.5	1: -16.06 ^Δ	1: L114, F115, A117, V120, R124, F186, T189, V202	3.4	F87: 4.07 H216: 5.24 T225: 5.91 R231: 3.45	3.6	N107: -4.69 P108: - A109: -4.82 N228: 0.00 P229: -0.85 A230: -0.76
	2: 3.1		2: 1.94				2: F51, G88, M90, A136, V215, I227, N228, R231*,	
eAqpZ (1RC2)	2.0	37.5	4.15	G19, F43*, H174*, S184, R189*, S190	2.0	F43: 3.67 H174: 5.75 T183: 6.51 R189: 2.50	3.6	N63: -4.55 P64: - A65: - N186: 0.00 P187: - A188: -
							3.5	
aAqpZ2 (3LLQ)	2.0	39.0	4.58	A40, F43*, I135, E136, H172*, T181*, S182, S188	2.0	F43: 3.25 H172: 5.55 T181: 6.32 R187: 2.45	5.1	N63: -4.39 P64: -4.42 A65: - N184: 0.00 P185: - A186: -
							3.0	
pAqgp (3C02)	3.1	61.0	4.55	M24, L48, W50*, L178, F190*, A191, D197, P223	3.1	W50: 5.08 G181: - F190: 5.45 R196: 2.28	4.9	N70: -4.34 L71: - A72: - N193: 0.00 P194: - S195: -
							4.0	
eGlpF (1FX8)	3.0	48.6	3.59	S45, W48*, A97, F200*, A201, R206*, P236	3.0	W48: 4.37 G191: - F200: 4.13	4.9	N68: -4.26 P69: - A70: -

R206: 2.78	6.1	N203: 0.00
		P204: -
		A205: -

^a Aquaporin full names and their source organisms are given in Table 2 of the main article. ^b Minimum pore diameter calculated by the PoreWalker server [6] along the x -coordinates (x -axis) of the AQPs' pore. The x -axis refers to that perpendicular to the zy cellular membrane plane, i.e. the main/longest pore axis. In cases where a minimum pore diameter appears near the terminal ends of the pore (see diameter profiles in Figure S3 and Figure 5 of the main article), a second minimum closer to the central part is also reported. ^c Measure of regularity or linearity of the pore as issued by the PoreWalker server. The value refers to the percentage of pore centers (at 1 Å step) that could be fitted to a line. ^d x -coordinates where the pore exhibits the minimum diameter(s). Values extracted from the diameter plots included in Figure S3 (left top panels), which were obtained at 3 Å step by PoreWalker server. The x -coordinate associated to each amino acid is that of their beta carbon (β C). The x -coordinates along the whole x -axis were shifted to place the beta carbon (β C) of the asparagine (N) in the second NPA motif in the center of the x -coordinate system ($x=0$), for all the AQPs analyzed (check it out in the last column, in bold). This way the x -coordinates are aligned according to the equivalent residues in the AQPs (as if they were aligned structurally). With a delta (Δ) symbol appear those x -coordinates of minima located near the cytosolic or the extracellular interfaces of the pore. ^e Residues located within an x -coordinate range of ± 2 Å of the pore minimum. With an asterisk (*) those amino acids forming the SF motifs. ^f Minimum pore diameter in the x -coordinates range encompassing the four residues forming the selectivity filter (SF). ^g x -coordinates of the amino acids (β C) forming the SF motif. ^h Minimum pore diameter found within the x -coordinates range of the six residues forming the two NPA motifs. ⁱ x -coordinates of the amino acids (β C) forming the NPA motifs. In bold the asparagine in the second NPA motif that constitute the reference ($x=0$) coordinate. **Note:** All the information used to extract the data showed in this table is contained in the PoreWalker output files, provided as **Supplementary Files**. Pore diameter profiles and additional information on the pore shape are given —more visually— in Figure S3 and Figure 5 of the main article.

Table S4. Statistical and predictive parameters of the best-performing QSAR models, including those with one and two PDs.^a

No. PDs in model ^b	Pore Trimming (x-coord range) ^c	PD1 (coeff. ± SE) ^d	PD2 (coeff. ± SE) ^d	Independent term (± SE) ^d	R ²	P-value (F-statistic)	Condition Number ^e	VIF ^e	LOO-Q ^{2f}	SPRESS _g
1	-20 to 17.5	Ave_Bfac_SC (5.75 ± 1.26) ^{***}	—	5.91 ± 1.26 ^{***}	0.72	0.002	1.0	—	0.40	5.22
	-17.5 to 17.5	Ave_Bfac_SC (5.42 ± 1.43) ^{***}	—	5.91 ± 1.43 ^{***}	0.64	0.005	1.0	—	0.30	5.67
	-15 to 15	Ave_Bfac_SC (5.34 ± 1.47) ^{***}	—	5.91 ± 1.47 ^{***}	0.62	0.007	1.0	—	0.30	5.66
	-10 to 10	Ave_Bfac_SC (5.68 ± 1.30) ^{***}	—	5.91 ± 1.30 ^{***}	0.70	0.002	1.0	—	0.41	5.19
	-7.5 to 7.5	Ave_Bfac_SC (5.43 ± 1.43) ^{***}	—	5.91 ± 1.43 ^{***}	0.64	0.005	1.0	—	0.34	5.48
	-5 to 5	Ave_Bfac_SC (5.10 ± 1.57) ^{**}	—	5.91 ± 1.57 ^{***}	0.57	0.01	1.0	—	0.27	5.78
2	-20 to 17.5	Ave_Bfac_SC (5.43 ± 1.10) ^{***}	Ave_diam (2.14 ± 1.10) [*]	5.91 ± 1.08 ^{***}	0.82	0.002	1.16	1.02	0.55	4.56
	-17.5 to 17.5	Ave_Bfac_SC (5.36 ± 1.29) ^{***}	Ave_diam (2.18 ± 1.29) [*]	5.91 ± 1.29 ^{***}	0.75	0.008	1.03	1.0	0.34	5.48
	-15 to 15	Ave_Bfac_SC (5.32 ± 1.40) ^{***}	Ave_diam (1.89 ± 1.40)	5.91 ± 1.40 ^{***}	0.73	0.01	1.01	1.0	0.37	5.35
	-10 to 10	Ave_Bfac_SC (5.76 ± 1.22) ^{***}	Ave_diam (1.79 ± 1.22)	5.91 ± 1.21 ^{***}	0.81	0.003	1.05	1.0	0.53	4.65
	-7.5 to 7.5	Ave_Bfac_SC	Ave_diam	5.91 ± 1.39 ^{***}	0.76	0.007	1.09	1.0	0.45	5.04

	(5.29 ± 1.40) ^{***}	(1.65 ± 1.40)							
-5 to 5	Ave_Bfac_SC (4.47 ± 1.78) ^{***}	Ave_hydrophi (-1.46 ± 1.78)	5.91 ± 1.60 ^{***}	0.66	0.02	1.58	1.22	0.32	5.58

^a Data associated to the models obtained for each of the six evaluated training sets (pore trimmings). ^b Number of PDs included in the best QSAR models presented in the rows. ^c *x*-coordinate ranges remaining after trimming the pore (see the **Supplementary Materials and Methods** section), which resulted in different data sets used for the QSAR modeling. ^d S.E. stands for standard error, and the number of asterisks shown over the values indicates the statistical significance (p-value from a Student t-test) obtained for the PDs or the independent term of the models, namely: * if p < 0.1, ** if p < 0.05, and *** if p < 0.01. ^e Summarized descriptions of the condition number (CN) and the Variance Inflation Factor (VIF) are given above in the **Supplementary Materials and Methods** section. ^f LOO-Q² is the leave-one-out cross-validation coefficient used to assess the internal predictability of the models. ^g SPRESS stands for Standard Prediction Error Sum of Squares.

Table S5. Experimental versus predicted PR residuals obtained from Models 1 and 2 presented in the main manuscript.^a

AQP (PDB)	Exp. PR ^b	Predicted PR	Residual ^c	Predicted PR	Residual ^c
	p_f ($\times 10^{-14} \text{ cm}^3 \cdot \text{s}^{-1}$)	p_f ($\times 10^{-14} \text{ cm}^3 \cdot \text{s}^{-1}$)	(Exp. vs. Pred.)	p_f ($\times 10^{-14} \text{ cm}^3 \cdot \text{s}^{-1}$)	(Exp. vs. Pred.)
			Model 1	Model 2	
bAqp0 (1YMG)	0.15	5.18	-5.04	1.42	-1.28
oAqp0 (2B6O)	0.2	3.74	-3.54	-0.37	0.57
bAqp1 (1J4N)	2.3	3.86	-1.56	4.77	-2.47
hAqp1 (7UZE)	5.1	-0.36	5.46	0.60	4.50
hAqp2 (4NEF)	9.3	9.43	-0.13	8.53	0.77
hAqp4 (3GD8)	11.0	13.77	-2.77	15.29	-4.29
rAqp4 (2D57)	23	17.28	5.72	18.29	4.71
mAqpM (2F2B)	0.65	2.52	-1.87	3.96	-3.31
eAqpZ (1RC2)	6.0	5.87	0.13	6.46	-0.46
eGlpF (1FX8)	1.35	-2.25	3.60	0.09	1.26

^a Predicted osmotic permeabilities, and experimental versus predicted residuals obtained from the QSAR models presented in the main manuscript and in Table S4 for the pore trimming from -20- to -17.5 Å. ^b Experimental osmotic permeation rates (averages when more than one is reported for an AQP) as reported in Table S1. ^c The average residuals from Model 1 (single-PD) —in absolute values— mount to $2.98 \times 10^{-14} \text{ cm}^3 \cdot \text{s}^{-1}$, whereas from Model 2 (Two-PD) mount to $2.36 \times 10^{-14} \text{ cm}^3 \cdot \text{s}^{-1}$.

Table S6. Resolution, experimental conditions and other relevant information about the crystallization of the AQPs included in the QSAR training set.^a

^aThe table is provided as an Excel **Supplementary File**. Data reported in this table has been retrieved from the Protein Data Bank [43] website ('Experiment' tab in each PDB entry).

SUPPLEMENTARY FIGURES

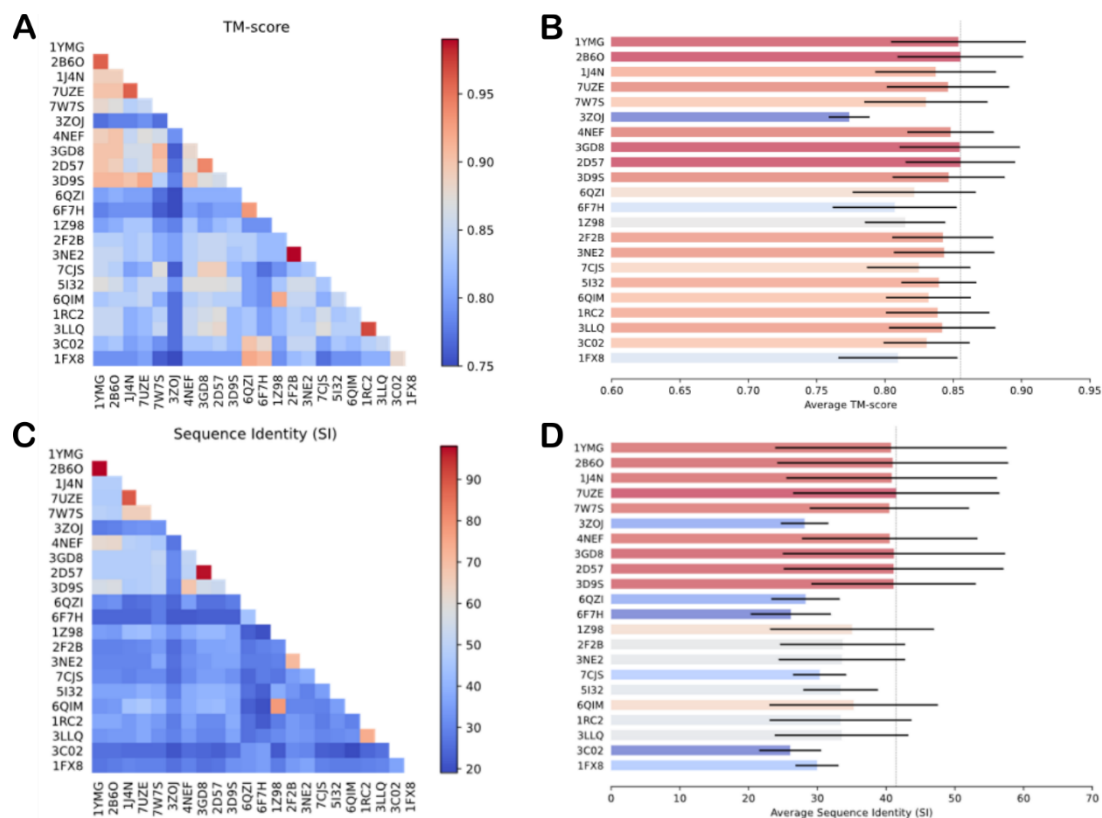


Figure S1. Structural and sequence comparisons of AQPs. (A) TM-score-based pairwise map. (B) Per structure averaged TM-score against all other structures (bars). (C) Sequence identity (SI) pairwise map. (D) Per structure averaged SI against all other structures (bars). A min-max normalization is adopted for the bars coloring. The black lines at the right-hand side of the bars represent the standard deviations, whereas the dashed vertical lines indicate the maximum averages among all the structures. The initial chain of the tetrameric AQP's PDB structures was taken for the calculations. The corresponding AQP's of the compared structures (PDBs) are given in Tables 1 and 2 of the main manuscript.

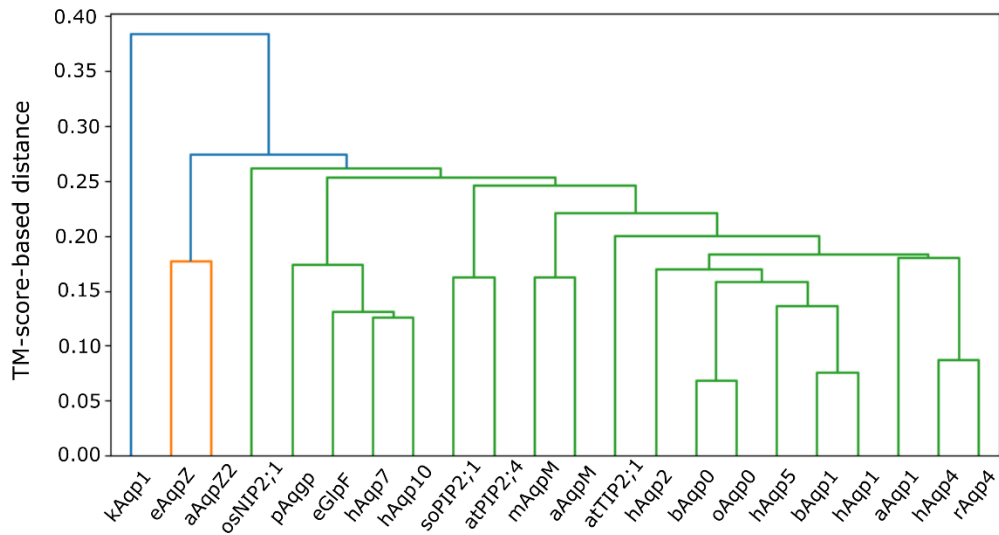
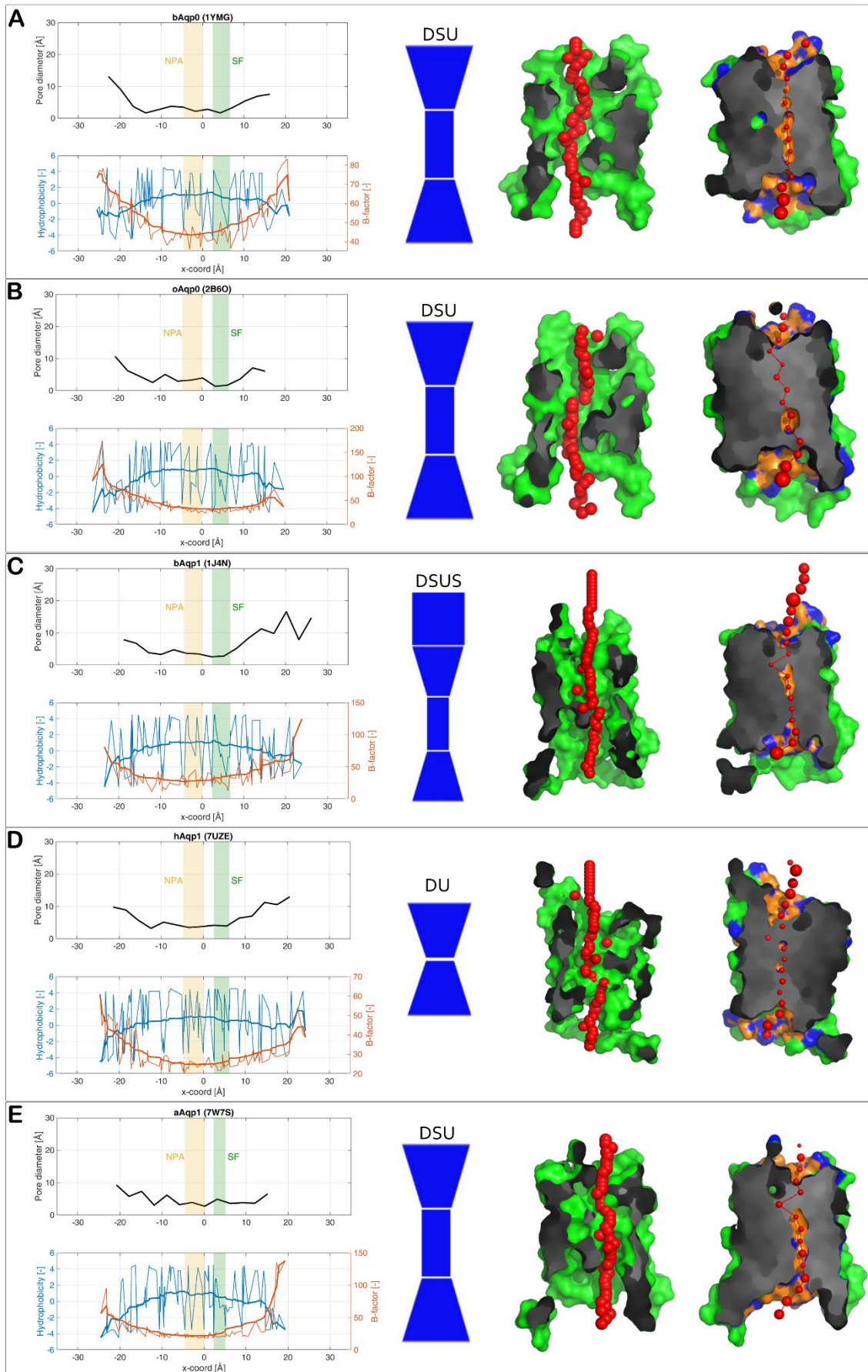
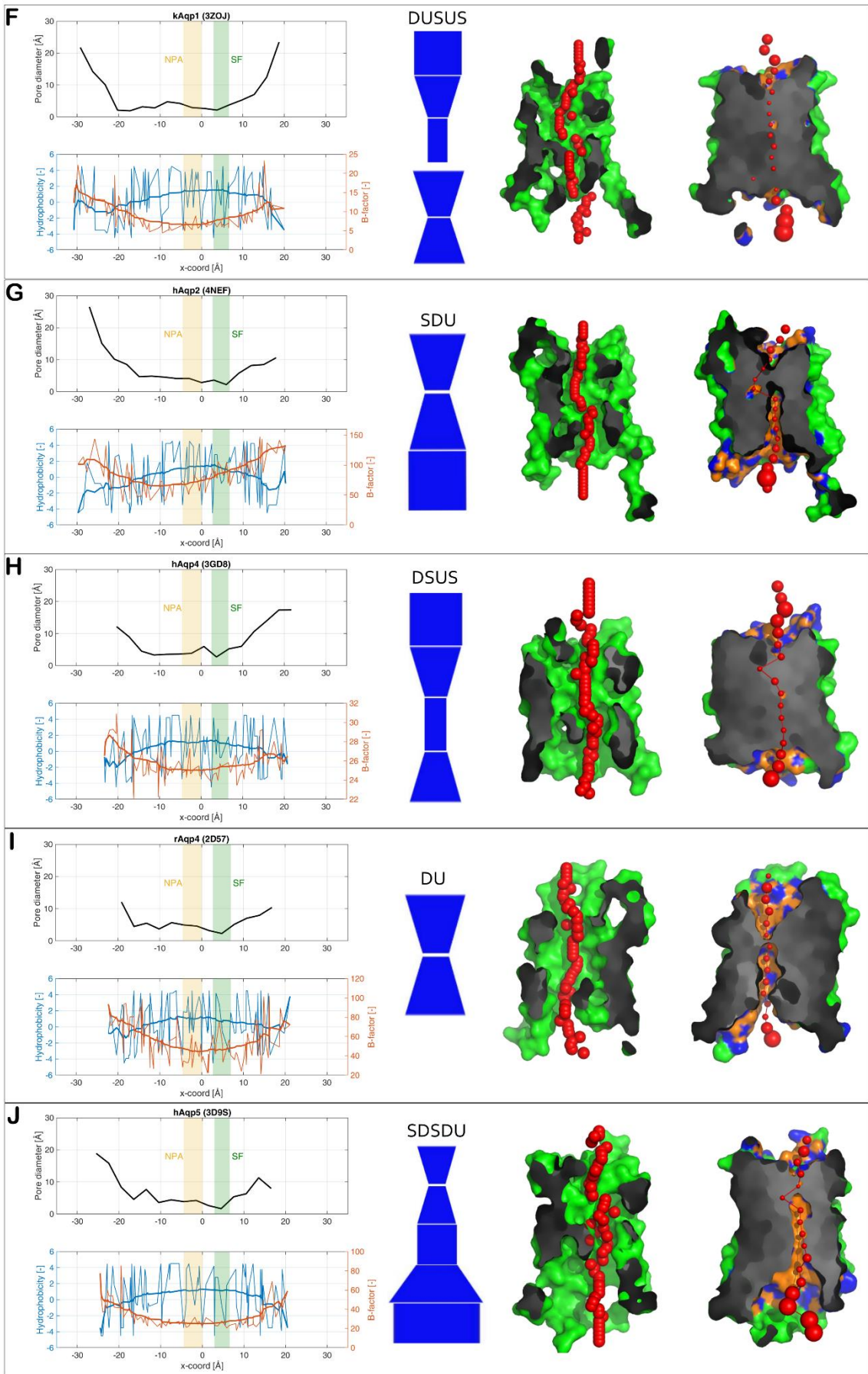
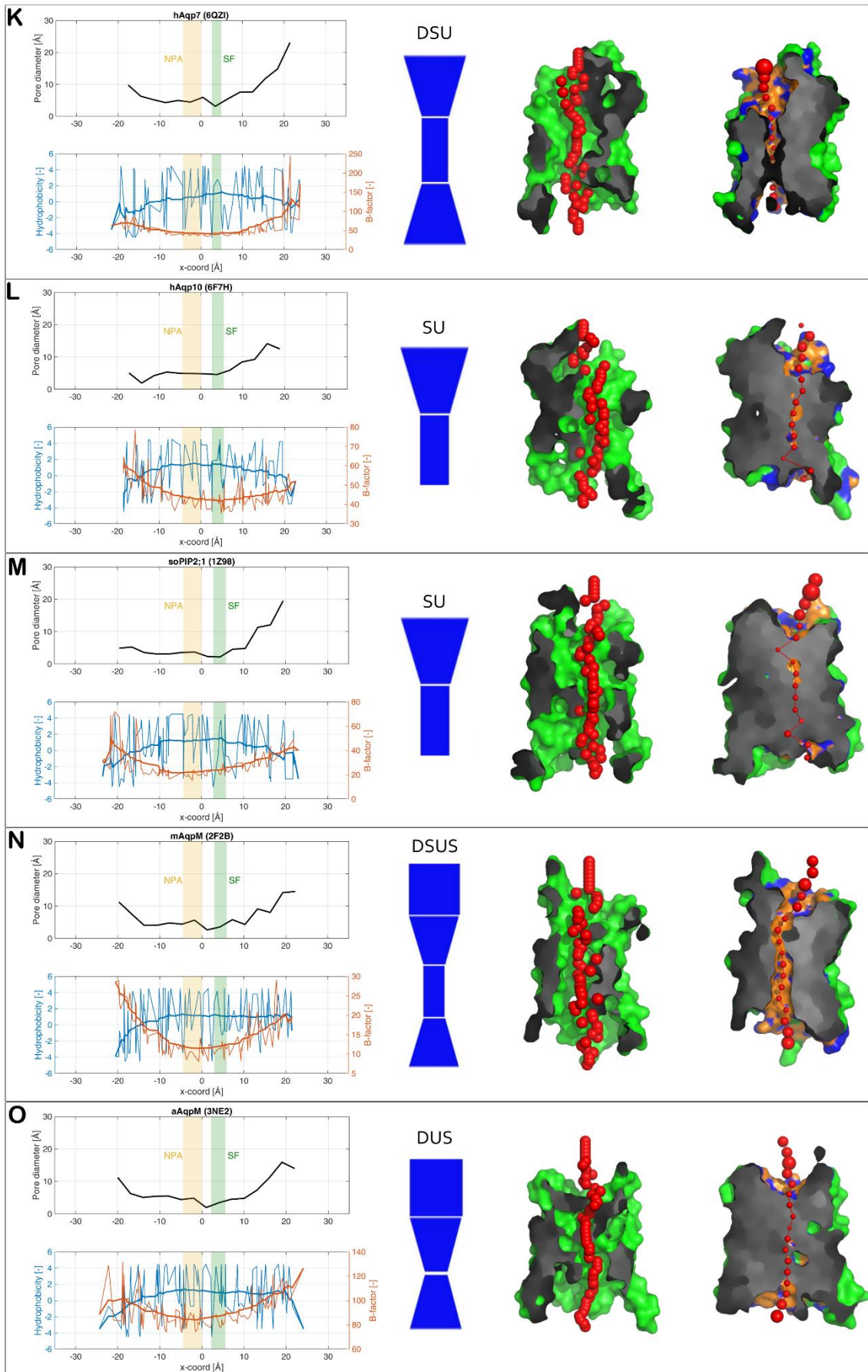
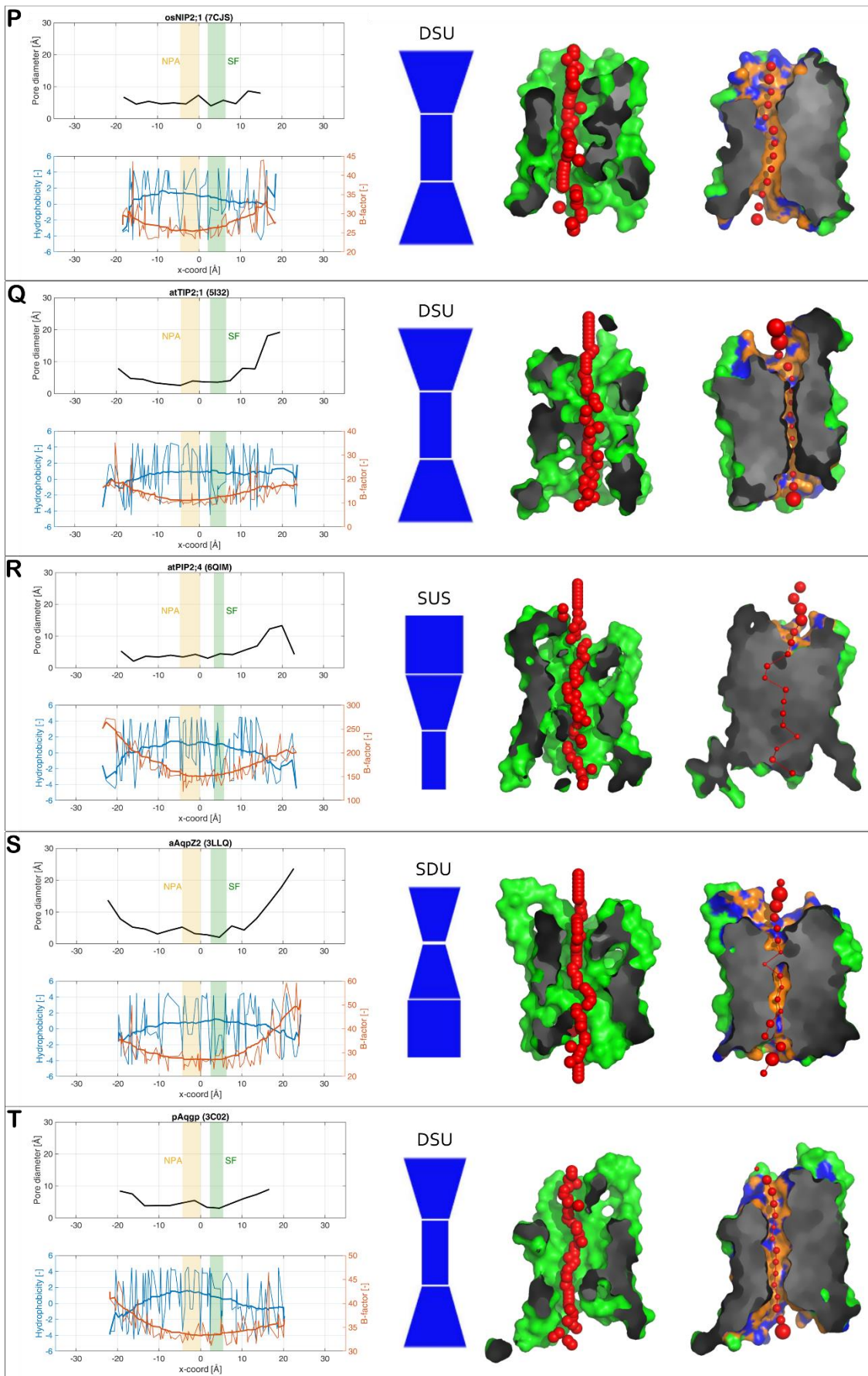


Figure S2. Hierarchical clustering based on the pairwise TM-score of AQPs. The PDB IDs of the structures used are those reported in Tables 1 and 2 of the main manuscript, and in Figure S1. The single linkage method from the Python SciPy library (v.1.11.4) [44] was used for the clustering.









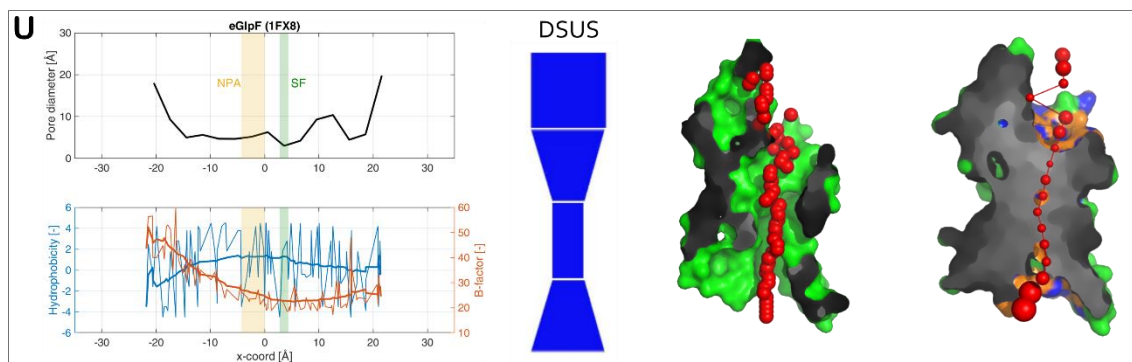


Figure S3. Pore properties profiles and geometrical shape for all the AQPs listed in Tables 1 and 2 of the main manuscript, except for *E. coli* AqpZ included in the main article. Left top panels: diameter profile along the pore principal axis (x -coordinate) at 3\AA step as calculated by the PoreWalker tool [6]. Left bottom panels: per-residue hydrophobicity index (blue) and B-factor (orange) of amino acids in the pore lining along the pore x -coordinate, as calculated by the Discovery Studio (BIOVIA, Dassault Systèmes) [45] and as obtained from the crystal PDB files, respectively. The thicker lines are smoothed curves (noise removed). Vertical bands depicted show the x -coordinates ranges where the NPA (orange) and SF (green) motifs are located. The blue funnel-like form at the center is a 2D projection of the predicted pore shape as calculated by variations of diameter values along the pore: the bottom of the pore axis (i.e., the lowest x -coordinate) correspond to the bottom of the stack. In the letter code on the top of the form, 'D' indicates a conical frustum generated by decreasing pore diameter values, i.e. the diameter of the lower base of the frustum is bigger than the diameter of its upper circle, 'U' indicates the opposite conical frustum, i.e., lower base diameter smaller than upper base diameter, and 'S' indicates a cylinder (the code ordering from bottom to top). The two longitudinal cross-sectional images are selected cuts along the pore's x -coordinate issued by PoreWalker, where the pore regularity is shown in the first cross-sectional image through red spheres located at the centre of the pore every 1\AA step, whereas the pore dimension is represented in the second cross-sectional image by red spheres—at the center of the pore at 3\AA step—, whose sizes are proportional to the pore diameter calculated at that point. In the latter, orange and blue areas show pore-lining atoms and corresponding residues, respectively. (A) bAqp0 (PDB ID 1YMG); (B) oAqp0 (PDB ID 2B6O); (C) bAqp1 (PDB ID 14JN); (D) hAqp1 (PDB ID 7UZE); (E) aAqp1 (PDB ID 7W7S); (F) kAqp1 (PDB ID 3ZOJ); (G) hAqp2 (PDB ID 4NEF); (H) hAqp4 (PDB ID 3GD8); (I) rAqp4 (PDB ID 2D57); (J) hAqp5 (PDB ID 3D9S); (K) hAqp7 (PDB ID 6QZI); (L) hAqp10 (PDB ID 6F7H); (M) soPIP2;1 (PDB ID 1Z98); (N) mAqpM (PDB ID 2F2B); (O) aAqpM (PDB ID 3NE2); (P) osNIP2;1 (PDB ID 7CJS); (Q) atTIP2;1 (PDB ID 5I32); (R) atPIP2;4 (PDB ID 6QIM); (S) aAqpZ2 (PDB ID 3LLQ); (T) pAgqp (PDB ID 3C02); (U) eGlpF (PDB ID 1FX8). **Notes:** Aquaporin full names and their source organisms are given in Table 2 of the main manuscript. Amino acids in the pore lining are reported in the PoreWalker's output files (**Supplementary Files**). The x -coordinates in the panels at the left (diameter, hydrophobicity index and B-factors profiles) were shifted from the original ones issued by PoreWalker, to place the beta carbon (βC) of the asparagine (N) in the second NPA motif at the center of the x -coordinate system ($x=0$). This ensures that all the AQPs are aligned to have the same reference x -coordinate.

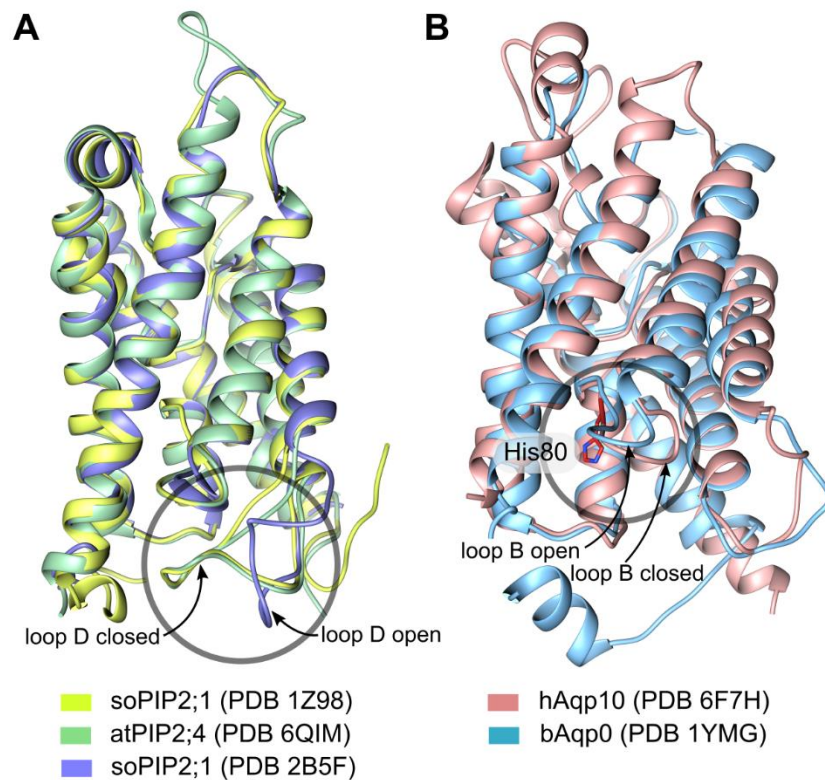


Figure S4. Structure comparison of AQPs on pore gating molecular events. (A) Overlapping of *Spinacia oleracea* PIP2;1, in its closed (PDB ID 1Z98 [46]) and open conformations (PDB ID 2B5F [46]), with the closed conformation of *Arabidopsis thaliana* PIP2;4 (PDB ID 6QIM [47]) aquaporin. Highlighted (circled region) are the main conformational differences in the cytoplasmic loop D that describe the ‘pore-gating’ event. (B) Overlapping human aquaporin-10 (PDB ID 6F7H [48]) with bovine aquaporin-0 (PDB ID 1YMG [49]) to highlight (circled region) the open conformation of loop B (pore gating) in the former. His80, described as the key residue for the pH-dependent loop-B conformational change (pH-sensor [48]), is depicted (sticks).

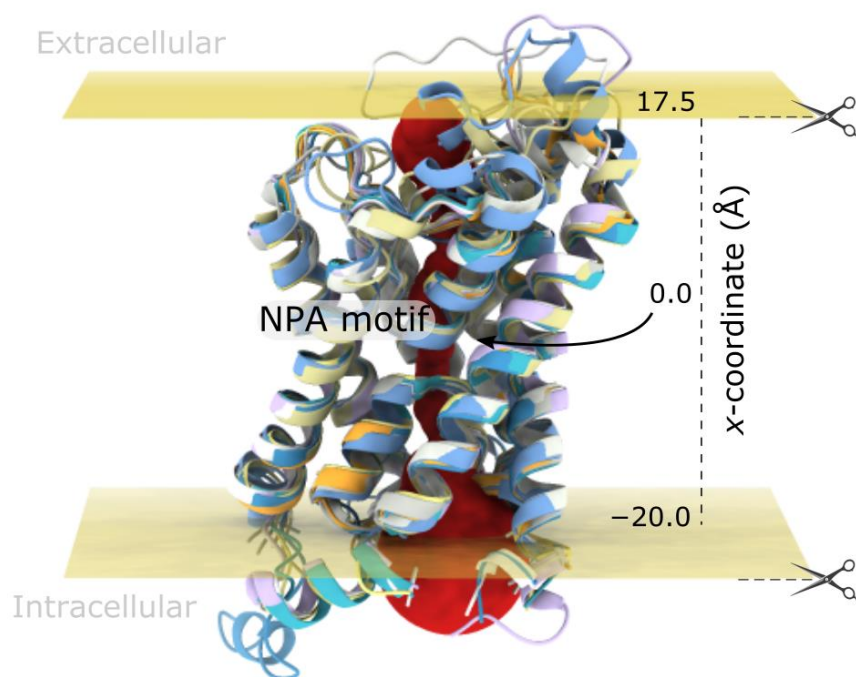


Figure S5. Scheme showing the structural alignment of the ten AQPs used as the training set in the pore-level QSAR study conducted as a proof of concept. Horizontal planes indicate the positions at which the pores were initially trimmed (x -coordinates of -20 and 17.5 Å) to equalize their lengths. The central red yarn ball-like form approximately represent the pore diameter of one of the aligned AQPs.

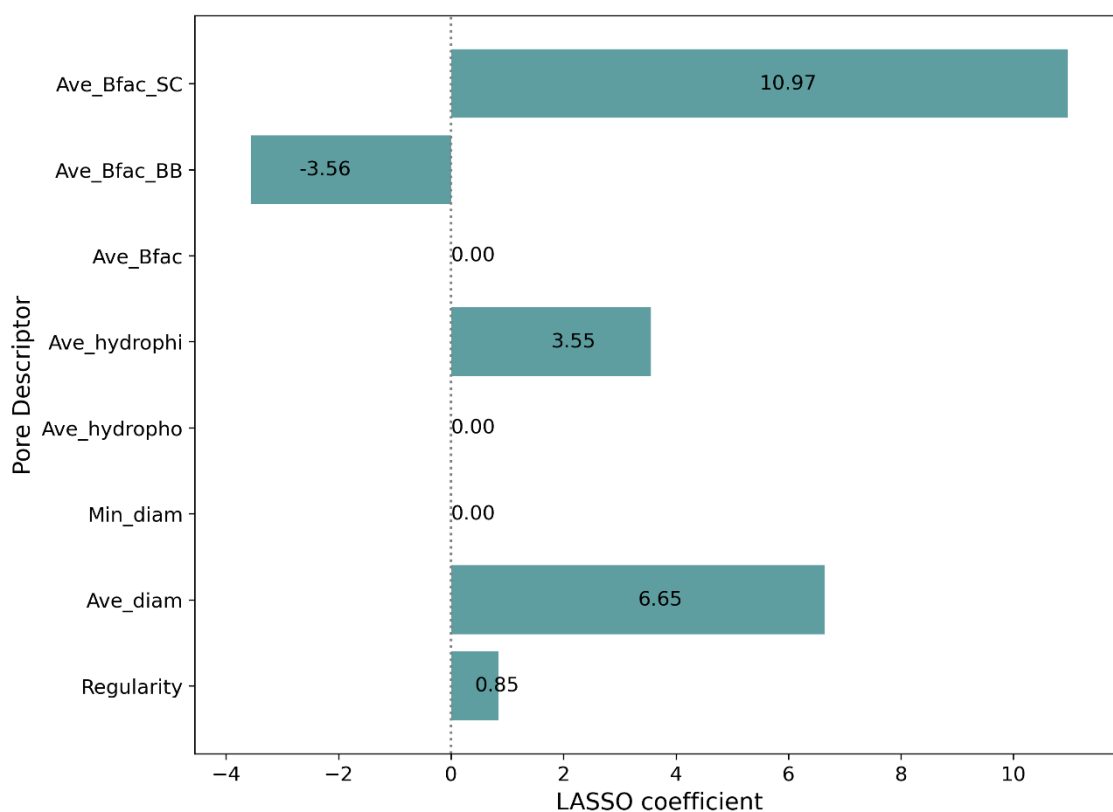


Figure S6. Final LASSO coefficients after applying the LASSO method [10] for feature selection. LASSO coefficients (in the middle of the horizontal bars) per pore descriptor for PDs' dataset obtained with AQPs' pore trimmed by the x -coordinate -20 and 17.5 \AA , $\alpha = 0.1$, and 1,000,000 iterations.

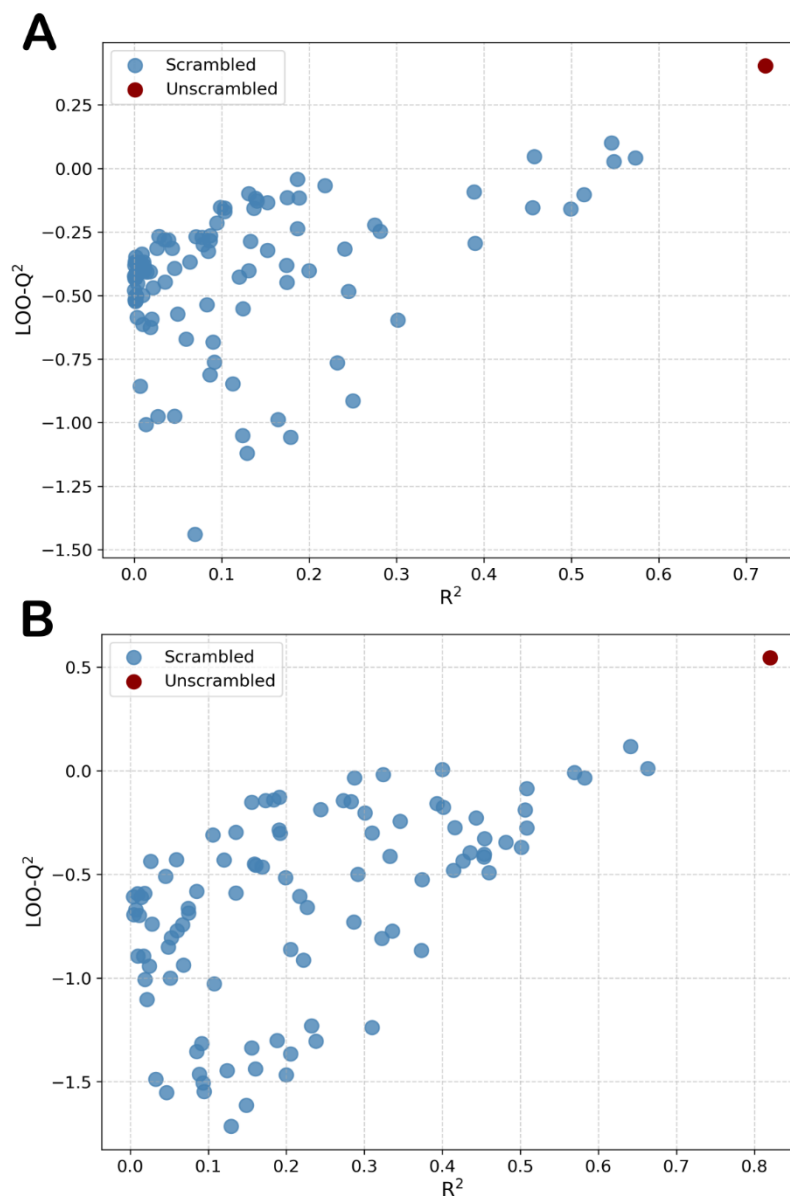


Figure S7. Comparative analysis of *y*-scrambled models versus the unscrambled one. In *y*-axis are the internal predictive metric LOO-Q² and in *x*-axis the squared Pearson correlation (R²) of the pore-level QSAR models compared. Blue dots represent a hundred (100) *y*-scrambled models, whereas the red dot represents the unscrambled (original) best QSAR model of a single PD (A) and two PDs (B), obtained for the AQPs' pore trimmed by the *x*-coordinate -20 and 17.5 Å (see Table S4 and Figure S5).

SUPPLEMENTARY REFERENCES

1. Zhang, Y.; Skolnick, J. Scoring Function for Automated Assessment of Protein Structure Template Quality. *Proteins: Structure, Function, and Bioinformatics* **2004**, *57*, 702–710, doi:10.1002/prot.20264.
2. Xu, J.; Zhang, Y. How Significant Is a Protein Structure Similarity with TM-Score= 0.5? *Bioinformatics* **2010**, *26*, 889–895, doi:10.1093/bioinformatics/btq066.
3. RCSB PDB Pairwise Structure Alignment Available online: <https://www.rcsb.org/alignment> (accessed on 26 April 2024).
4. Li, Z.; Jaroszewski, L.; Iyer, M.; Sedova, M.; Godzik, A. FATCAT 2.0: Towards a Better Understanding of the Structural Diversity of Proteins. *Nucleic acids research* **2020**, *48*, W60–W64, doi:10.1093/nar/gkaa443.
5. Ye, Y.; Godzik, A. Flexible Structure Alignment by Chaining Aligned Fragment Pairs Allowing Twists. *Bioinformatics* **2003**, *19*, ii246–ii255, doi:10.1093/bioinformatics/btg1086.
6. Pellegrini-Calace, M.; Maiwald, T.; Thornton, J.M. PoreWalker: A Novel Tool for the Identification and Characterization of Channels in Transmembrane Proteins from Their Three-Dimensional Structure. *PLoS Comput Biol* **2009**, *5*, e1000440, doi:10.1371/journal.pcbi.1000440.
7. Kyte, J.; Doolittle, R.F. A Simple Method for Displaying the Hydrophobic Character of a Protein. *Journal of Molecular Biology* **1982**, *157*, 105–132, doi:10.1016/0022-2836(82)90515-0.
8. O'Brien, R.M. A Caution Regarding Rules of Thumb for Variance Inflation Factors. *Qual Quant* **2007**, *41*, 673–690, doi:10.1007/s11135-006-9018-6.
9. Detecting and Assessing Collinearity. In *Regression Diagnostics*; John Wiley & Sons, Ltd, 1980; pp. 85–191 ISBN 978-0-471-72515-2.
10. Tibshirani, R. Regression Shrinkage and Selection Via the Lasso. *Journal of the Royal Statistical Society: Series B (Methodological)* **1996**, *58*, 267–288, doi:10.1111/j.2517-6161.1996.tb02080.x.
11. Van Hoek, A.N.; Wiener, M.; Bicknese, S.; Miercke, L.; Biwersi, J.; Verkman, A. Secondary Structure Analysis of Purified Functional CHIP28 Water Channels by

- CD and FTIR Spectroscopy. *Biochemistry* **1993**, 32, 11847–11856, doi:10.1021/bi00095a013.
12. Hashido, M.; Ikeguchi, M.; Kidera, A. Comparative Simulations of Aquaporin Family: AQP1, AQPZ, AQP0 and GlpF. *FEBS letters* **2005**, 579, 5549–5552, doi:10.1016/j.febslet.2005.09.018.
 13. Chandy, G.; Zampighi, G.A.; Kreman, M.; Hall, J.E. Comparison of the Water Transporting Properties of MIP and AQP1. *The Journal of membrane biology* **1997**, 159, 29–39, doi:10.1007/s002329900266.
 14. Zampighi, G.A.; Kreman, M.; Boorer, K.J.; Loo, D.D.F.; Bezanilla, F.; Chandy, G.; Hall, J.E.; Wright, E.M. A Method for Determining the Unitary Functional Capacity of Cloned Channels and Transporters Expressed in *Xenopus Laevis* Oocytes. *J. Membran Biol.* **1995**, 148, 65–78, doi:10.1007/BF00234157.
 15. Saboe, P.O.; Rapisarda, C.; Kaptan, S.; Hsiao, Y.-S.; Summers, S.R.; De Zorzi, R.; Dukovski, D.; Yu, J.; de Groot, B.L.; Kumar, M.; et al. Role of Pore-Lining Residues in Defining the Rate of Water Conduction by Aquaporin-0. *Biophysical Journal* **2017**, 112, 953–965, doi:10.1016/j.bpj.2017.01.026.
 16. Yang, B.; Verkman, A. Water and Glycerol Permeabilities of Aquaporins 1–5 and MIP Determined Quantitatively by Expression of Epitope-Tagged Constructs in *Xenopus* Oocytes. *Journal of Biological Chemistry* **1997**, 272, 16140–16146, doi:10.1074/jbc.272.26.16140.
 17. Schulte, D.J.; van Hoek, A.N. Functional Analysis and Association State of Water Channel (AQP-1) Isoforms Purified from Six Mammals. *Comparative Biochemistry and Physiology Part B: Biochemistry and Molecular Biology* **1997**, 118, 35–43, doi:10.1016/S0305-0491(97)00015-1.
 18. Zhu, F.; Tajkhorshid, E.; Schulten, K. Theory and Simulation of Water Permeation in Aquaporin-1. *Biophysical journal* **2004**, 86, 50–57, doi:10.1016/S0006-3495(04)74082-5.
 19. Groot, B.L. de; Grubmüller, H. The Dynamics and Energetics of Water Permeation and Proton Exclusion in Aquaporins. *Current opinion in structural biology* **2005**, 15, 176–183, doi:10.1016/j.sbi.2005.02.003.

20. Van Hoek, A.; Verkman, A. Functional Reconstitution of the Isolated Erythrocyte Water Channel CHIP28. *Journal of Biological Chemistry* **1992**, *267*, 18267–18269, doi:10.1016/S0021-9258(19)36953-4.
21. Zeidel, M.L.; Ambudkar, S.V.; Smith, B.L.; Agre, P. Reconstitution of Functional Water Channels in Liposomes Containing Purified Red Cell CHIP28 Protein. *Biochemistry* **1992**, *31*, 7436–7440, doi:10.1021/bi00148a002.
22. Walz, T.; Smith, B.L.; Zeidel, M.L.; Engel, A.; Agre, P. Biologically Active Two-Dimensional Crystals of Aquaporin CHIP. *Journal of Biological Chemistry* **1994**, *269*, 1583–1586, doi:10.1016/S0021-9258(17)42062-X.
23. Zeidel, M.L.; Nielsen, S.; Smith, B.L.; Ambudkar, S.V.; Maunsbach, A.B.; Agre, P. Ultrastructure, Pharmacologic Inhibition, and Transport Selectivity of Aquaporin CHIP in Proteoliposomes. *Biochemistry* **1994**, *33*, 1606–1615, doi:10.1021/bi00172a042.
24. Wertén, P.J.L.; Hasler, L.; Koenderink, J.B.; Klaassen, C.H.W.; de Grip, W.J.; Engel, A.; Deen, P.M.T. Large-Scale Purification of Functional Recombinant Human Aquaporin-2. *FEBS Letters* **2001**, *504*, 200–205, doi:10.1016/S0014-5793(01)02703-X.
25. Binesh, A.R.; Kamali, R. Molecular Dynamics Insights into Human Aquaporin 2 Water Channel. *Biophysical chemistry* **2015**, *207*, 107–113, doi:10.1016/j.bpc.2015.10.002.
26. Kitchen, P.; Salman, M.M.; Halsey, A.M.; Clarke-Bland, C.; MacDonald, J.A.; Ishida, H.; Vogel, H.J.; Almutiri, S.; Logan, A.; Kreida, S.; et al. Targeting Aquaporin-4 Subcellular Localization to Treat Central Nervous System Edema. *Cell* **2020**, *181*, 784-799.e19, doi:10.1016/j.cell.2020.03.037.
27. Alberga, D.; Nicolotti, O.; Lattanzi, G.; Nicchia, G.P.; Frigeri, A.; Pisani, F.; Benfenati, V.; Mangiatordi, G.F. A New Gating Site in Human Aquaporin-4: Insights from Molecular Dynamics Simulations. *Biochimica et Biophysica Acta (BBA)- Biomembranes* **2014**, *1838*, 3052–3060, doi:10.1016/j.bbamem.2014.08.015.
28. Garate, J.-A.; English, N.J.; MacElroy, J.M.D. Human Aquaporin 4 Gating Dynamics in Dc and Ac Electric Fields: A Molecular Dynamics Study. *The Journal of Chemical Physics* **2011**, *134*, 055110, doi:10.1063/1.3529428.

29. Hashido, M.; Kidera, A.; Ikeguchi, M. Water Transport in Aquaporins: Osmotic Permeability Matrix Analysis of Molecular Dynamics Simulations. *Biophysical journal* **2007**, *93*, 373–385, doi:10.1529/biophysj.106.101170.
30. Tong, J.; Wu, Z.; Briggs, M.M.; Schulten, K.; McIntosh, T.J. The Water Permeability and Pore Entrance Structure of Aquaporin-4 Depend on Lipid Bilayer Thickness. *Biophysical Journal* **2016**, *111*, 90–99, doi:10.1016/j.bpj.2016.05.039.
31. Alishahi, M.; Kamali, R. Forced Diffusion of Water Molecules through Aquaporin-5 Biomembrane; a Molecular Dynamics Study. *Biophysics and physicobiology* **2018**, *15*, 255–262, doi:10.2142/biophysico.15.0_255.
32. de Mare, S.W.; Venskutonytė, R.; Eltschkner, S.; de Groot, B.L.; Lindkvist-Petersson, K. Structural Basis for Glycerol Efflux and Selectivity of Human Aquaporin 7. *Structure* **2020**, *28*, 215–222, doi:10.1016/j.str.2019.11.011.
33. Kozono, D.; Ding, X.; Iwasaki, I.; Meng, X.; Kamagata, Y.; Agre, P.; Kitagawa, Y. Functional Expression and Characterization of an Archaeal Aquaporin. *Journal of Biological Chemistry* **2003**, *278*, 10649–10656, doi:10.1074/jbc.M212418200.
34. Araya-Secchi, R.; Garate, J.A.; Holmes, D.S.; Perez-Acle, T. Molecular Dynamics Study of the Archaeal Aquaporin AqpM. *BMC Genomics* **2011**, *12 Suppl 4*, S8, doi:10.1186/1471-2164-12-S4-S8.
35. Lee, J.K.; Kozono, D.; Remis, J.; Kitagawa, Y.; Agre, P.; Stroud, R.M. Structural Basis for Conductance by the Archaeal Aquaporin AqpM at 1.68 Å. *Proceedings of the National Academy of Sciences* **2005**, *102*, 18932–18937, doi:10.1073/pnas.0509469102.
36. Borgnia, M.J.; Kozono, D.; Calamita, G.; Maloney, P.C.; Agre, P. Functional Reconstitution and Characterization of AqpZ, the E. Coli Water Channel Protein. *Journal of molecular biology* **1999**, *291*, 1169–1179, doi:10.1006/jmbi.1999.3032.
37. Jensen, M.Ø.; Mouritsen, O.G. Single-Channel Water Permeabilities of Escherichia Coli Aquaporins AqpZ and GlpF. *Biophysical journal* **2006**, *90*, 2270–2284, doi:10.1529/biophysj.105.073965.
38. Pohl, P.; Saparov, S.M.; Borgnia, M.J.; Agre, P. Highly Selective Water Channel Activity Measured by Voltage Clamp: Analysis of Planar Lipid Bilayers Reconstituted with Purified AqpZ. *Proceedings of the National Academy of Sciences* **2001**, *98*, 9624–9629, doi:10.1073/pnas.161299398.

39. Borgnia, M.J.; Agre, P. Reconstitution and Functional Comparison of Purified GlpF and AqpZ, the Glycerol and Water Channels from Escherichia Coli. *Proceedings of the National Academy of Sciences* **2001**, *98*, 2888–2893, doi:10.1073/pnas.051628098.
40. Zhu, F.; Tajkhorshid, E.; Schulten, K. Pressure-Induced Water Transport in Membrane Channels Studied by Molecular Dynamics. *Biophysical journal* **2002**, *83*, 154–160, doi:10.1016/S0006-3495(02)75157-6.
41. Saparov, S.M.; Tsunoda, S.P.; Pohl, P. Proton Exclusion by an Aquaglyceroprotein: A Voltage Clamp Study. *Biology of the Cell* **2005**, *97*, 545–550, doi:10.1042/BC20040136.
42. The UniProt Consortium UniProt: The Universal Protein Knowledgebase in 2023. *Nucleic Acids Research* **2023**, *51*, D523–D531, doi:10.1093/nar/gkac1052.
43. Berman, H.M.; Mitsuoka, K.; Westbrook, J.; Gilliland, Z.F. andG; Bhat, T.N.; Weissig, H.; Shindyalov, I.N.; Bourne, P.E. The Protein Data Bank. *Nucleic Acids Research* **2000**, *28*, 235–242, doi:10.1093/nar/28.1.235.
44. Virtanen, P.; Gommers, R.; Oliphant, T.E.; Haberland, M.; Reddy, T.; Cournapeau, D.; Burovski, E.; Peterson, P.; Weckesser, W.; Bright, J.; et al. SciPy 1.0: Fundamental Algorithms for Scientific Computing in Python. *Nat Methods* **2020**, *17*, 261–272, doi:10.1038/s41592-019-0686-2.
45. Discovery Studio, BIOVIA, Dassault Systèmes 2022.
46. Törnroth-Horsefield, S.; Wang, Y.; Hedfalk, K.; Johanson, U.; Karlsson, M.; Tajkhorshid, E.; Neutze, R.; Kjellbom, P. Structural Mechanism of Plant Aquaporin Gating. *Nature* **2006**, *439*, 688–694, doi:10.1038/nature04316.
47. Wang, H.; Schoebel, S.; Schmitz, F.; Dong, H.; Hedfalk, K. Characterization of Aquaporin-Driven Hydrogen Peroxide Transport. *Biochimica et biophysica acta. Biomembranes* **2020**, *1862*, 183065, doi:10.1016/j.bbamem.2019.183065.
48. Gotfryd, K.; Mósca, A.F.; Missel, J.W.; Truelsen, S.F.; Wang, K.; Spulber, M.; Krabbe, S.; Hélix-Nielsen, C.; Laforenza, U.; Soveral, G.; et al. Human Adipose Glycerol Flux Is Regulated by a pH Gate in AQP10. *Nature communications* **2018**, *9*, 1–11, doi:10.1038/s41467-018-07176-z.
49. Harries, W.E.; Akhavan, D.; Miercke, L.J.; Khademi, S.; Stroud, R.M. The Channel Architecture of Aquaporin 0 at a 2.2-Å Resolution. *Proceedings of the National*

Academy of Sciences of the United States of America **2004**, *101*, 14045–14050,
doi:10.1073/pnas.0405274101.